University of Milano-Bicocca
Department of Physics "G. Occhialini"
PhD program in Physics and Astronomy, 38th cycle

The evolution of massive galaxies across cosmic time as traced by their stellar populations

Candidate:
Fabio Rosario Ditrani

Supervisors:
Prof. Matteo Fossati
Dr. Marcella Longhetti

Registration number:
800712

Coordinator: Prof. Stefano Ragazzi

Academic year 2024/2025

Contents

Chapter 1

Introduction

Following the discovery that galaxies are extragalactic systems distinct from the Milky Way, fundamental questions arose within the astronomical community. These questions concerned the origin of their diverse morphologies, sizes, and spectral properties. Understanding the mechanisms that regulate galaxy formation and evolution is necessary to explaining the wide variety observed across the galaxy population. However, developing a comprehensive theory of galaxies evolution remains a major challenge. This is because it requires a detailed understanding of numerous complex and often correlated physical processes. Many of these mechanisms yield similar observational signatures, and their effects vary significantly with cosmic time, galactic mass, and local gravitational conditions. However, in the last two decades, large and deep spectroscopic and photometric surveys brought major improvements in our understanding of galaxy formation.

1.1 The growth of structures in a Hierarchical Universe

Galaxies do not evolve in isolation within an empty Universe. In fact, their formation and evolution are closely linked to cosmology, which describes the geometry, content, and dynamical history of the Universe. One of the most compelling evidence supporting the current cosmological paradigm came with the serendipitous discovery of the cosmic microwave background (CMB) radiation in 1964 (Penzias & Wilson 1965; Dicke et al. 1965). The CMB is the relic radiation from a hot and dense primordial state, confirming that the Universe began with a Big Bang and has been expanding and cooling ever since. Initial measurements of the CMB revealed a smooth temperature field, which composed a remarkably uniform map. This reinforced the view that the Universe is homogeneous and isotropic on large scales. However, the formation of cosmic structures requires small primordial perturbations. These were first detected in 1992 by the COBE satellite as temperature anisotropies of $\Delta T/T \sim 10^{-5}$ (Smoot et al. 1992). These minute fluctuations, nearly Gaussian in nature, served as the seeds for gravitational collapse, eventually giving rise to the large-scale structures we observe today.

Over the past decades, these and other observations, including galaxy distributions, cluster masses, and a more refined picture of the geometry of the Universe obtained through observations of standard candles and rulers, have led to the introduction of the dark matter paradigm (Peebles & Dicke 1968; Peebles & Yu 1970; Peebles 1974; Toomre 1977; White & Rees 1978; Peebles 1980). Subsequent studies provided the formulation of ΛCDM

model in the 1990s, the current standard model of cosmology that provides the foundation for the hierarchical structure formation scenario. This framework assumes a Universe composed of approximately 4% of baryonic matter, 26% of cold dark matter, and 70% of dark energy, the latter driving the accelerated expansion of the Universe. In this picture, small-scale fluctuations in the matter density field at the time of recombination ($z \sim 1100$) grew via gravitational instability into progressively larger structures. Smaller dark matter haloes formed first and merged across the cosmic time to build up the cosmic web. Figure 1.1 shows a schematic representation of the merger history of a dark matter halo in a cosmological simulation, represented as a tree of subsequent mergers.

However, the luminous structures we observe, i.e. galaxies, form only once the baryonic matter falls into these dark matter haloes, cools, and condenses to form stars. The processes governing the transformation of gas into stars are highly non-linear and sensitive to a range of physical mechanisms, including radiative cooling, star formation, feedback from supernovae and AGN, and environmental effects. While dark matter dictates the gravitational structure of the Universe, the baryonic physics determines the observable diversity of galaxies. We must therefore move from the cosmological model and its predictions to the observational diagnostics that empirically trace how galaxies form, evolve, and interact with their environment.

1.2 Observational evidences

1.2.1 Morphological classification

Edwin Hubble was the first to systematically classify galaxies based on their visual morphology, once it was established that these objects lay beyond the Milky Way. His influential scheme, known as Hubble tuning fork diagram, remains one of the most widely used classification tools in extragalactic astronomy (Hubble 1936). As shown in Figure 1.2, it organises galaxies into four broad morphological classes:

- **Elliptical galaxies (E)**. These exhibit smooth, featureless light distributions and elliptical isophotes. They are denoted E0 to E7, where the number reflects the ellipticity;
- **Spiral galaxies (S and SB)**. They are characterised by thin disks with spiral arms, they are subdivided into normal spirals (S) and barred spirals (SB) based on the presence of a central bar;
- **Lenticular galaxies (S0)**. They are positioned morphologically between ellipticals and spirals, and have smooth light distribution without spiral arms but with a disk and bulge structure;
- **Irregular galaxies (Irr)**. These systems lack clear symmetry, often appearing patchy or distorted. They do not exhibit a dominant bulge or disk.

Subsequent refinements of Hubble's scheme, most notably by de Vaucouleurs (1959), introduced intermediate types, extended the spiral sequence toward irregulars, and introduced numerical T-types to quantify morphology. These extensions were motivated by the discovery of a broader diversity in galactic structures and helped bridge gaps in the original classification.

While Hubble's sequence is morphological in nature, it correlates with several physical properties of galaxies. Many observable characteristics, such as colour, gas content, star

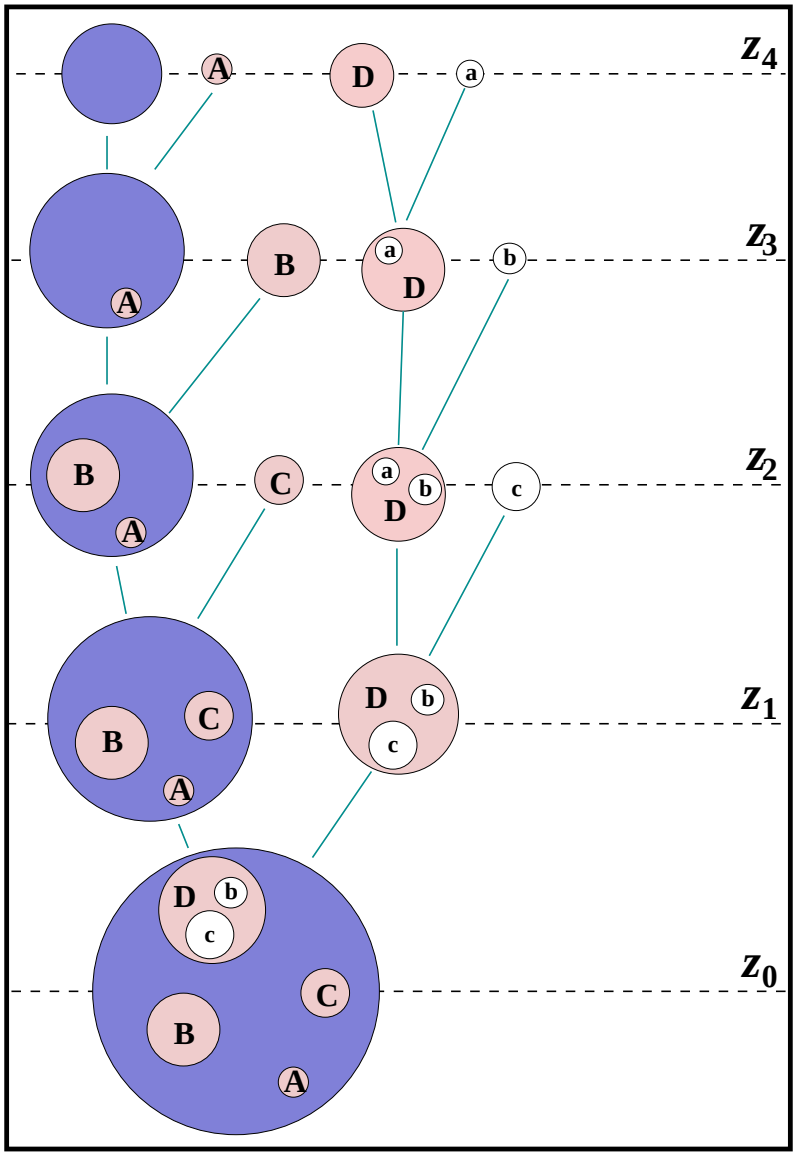

Figure 1.1: Schematic representation of the merger tree describing the hierarchical assembly of a dark matter halo from high to low redshift (z_4 to z_0, top to bottom). The size of each circle reflects the mass of the corresponding halo. The main progenitor evolves through successive mergers, accreting smaller haloes, such as A, B, C, and D, which survive as subhaloes at z_0. Some haloes, like a, are completely disrupted before the final timestep, while others (b and c) become substructures of larger satellites. Figure from Giocoli et al. (2010).

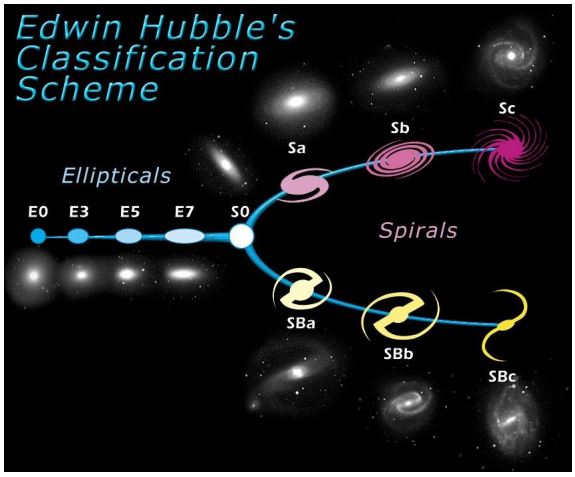

Figure 1.2: Hubble tuning fork diagram of galaxies classification. Elliptical and lenticular galaxies are shown on the left, while spiral galaxies appear on the right. Irregular galaxies are located in a separate region. Figure from https://science.nasa.gov.

formation activity, and stellar population age and metallicity, vary systematically along the sequence. For instance, elliptical and lenticular galaxies, typically red, gas-poor, and quiescent, are referred to as early-type galaxies (ETGs). In contrast, spiral and irregular galaxies, which are generally blue, gas-rich, and actively forming stars, are grouped as late-type galaxies (LTGs). Morphological classification is widely used as a practical framework for investigating galaxy evolution, environmental effects, and scaling relations. Although morphology alone cannot capture the full complexity of the history of a galaxy, it remains a useful tool in both observational and theoretical studies (e.g. van der Wel 2008; Skibba et al. 2009; Bamford et al. 2009; Pandey & Sarkar 2017; Costantin et al. 2025).

1.2.2 Galaxy bimodality and the role of stellar mass

Besides morphological type, another strong feature that has emerged from large-scale galaxy surveys is the bimodal distribution of galaxy properties. These properties are sensitive probes of the stellar populations, star formation histories, chemical composition, and dust content of galaxies.

Massive stars, which account for most of the emitted light in actively star-forming galaxies, emit most of their light in the blue/UV wavelengths but have short lifespans. In contrast, older and long lived stellar populations, that consist of lower-mass stars, emit predominantly in the red/infrared spectral region. As a result, the galaxy colour, defined as the difference in magnitude between two photometric bands, is a first-order indicator of the average age of the stellar population, and thus of the recent star formation rate of the galaxy. Large-scale surveys such as the Sloan Digital Sky Survey (SDSS, York et al. 2000) have demonstrated that galaxy colours exhibit a bimodal distribution, typically seen in colour-magnitude and colour-mass diagrams. Figure 1.3 shows the dust corrected $u - r$ colour as a function of the stellar mass for a large sample of galaxies in the local Universe from Schawinski et al. (2014). The existence of two distinct galaxy populations is evident (see also Strateva et al. 2001; Baldry et al. 2004). Indeed, these diagrams show two dominant populations: the 'red sequence', composed mostly of quiescent galaxies with old stellar populations and little to no star formation; and the 'blue cloud', occupied by actively star-forming galaxies. Moreover, there is a clear segregation in stellar mass. The red sequence is primarily populated by massive galaxies, while the blue cloud extends toward

the low-mass regime. An intermediate, less populated region, the so-called 'green valley', is thought to represent galaxies transitioning from star-forming to quiescent, in a process referred to as quenching. Therefore there is a general correlation between morphology and colour, where ETGs tend to populate the red sequence, while LTGs dominate the blue cloud.

However, the interpretation of galaxy colours must account for degeneracies. Indeed, a red colour similar to that characterising old stellar populations can also result from a younger but metal-rich population. In addition, dust extinction preferentially absorbs blue light, making dusty star-forming galaxies appear redder as well. To break the age-metallicity-dust degeneracy, various colour-colour diagrams have been proposed (e.g. Labbé et al. 2005; Shapley et al. 2005; Wuyts et al. 2007). Among them, one of the most used is based on rest-frame $U-V$ and $V-J$ colours (UVJ diagram, Williams et al. 2009; Whitaker et al. 2012) Figure 1.4 shows the UVJ diagram of a sample of observed galaxies in five redshift bins from Muzzin et al. (2013a), based on a Ks-selected catalogue of the COSMOS/UltraVISTA (Muzzin et al. 2013b). In the UVJ plane, quiescent galaxies occupy a distinct region from star-forming galaxies, with the latter forming a diagonal sequence. At fixed $U-V$ colour, dust-free quiescent galaxies are significantly bluer in $V-J$ than dusty star-forming galaxies, allowing a clear empirical separation.

As shown in the Figure 1.4, the colour bimodality of the galaxy population is not confined to the local Universe. Observations from deep photometric surveys (e.g., COMBO-17, COSMOS, CANDELS) have confirmed the presence of distinct red and blue populations out to at least $z \sim 2-3$ (e.g. Bell et al. 2004; Weiner et al. 2005; Brammer et al. 2009). With the advent of JWST, it has been discovered that the bimodality extends up to $z \sim 6$, highlighting the need to use new colour-colour diagrams to improve the accuracy of disentangle star-forming and quiescent galaxies (Antwi-Danso et al. 2023; Alberts et al. 2024). From the latter observational evidences, it is clear that quenching mechanisms capable of halting star formation in massive galaxies were already in place when the Universe was only a few billion years old. The emergence of a well-defined red sequence at early times suggests that at least a subset of galaxies experienced rapid star formation followed by efficient feedback, transitioning to a passive state early in the cosmic history (e.g. Forrest et al. 2020; Carnall et al. 2024; Kimmig et al. 2025).

A deeper understanding of galaxy bimodality arises when considering stellar mass. Observational evidence indicates a characteristic stellar mass scale $M_{crit} \sim 3 \times 10^{10} M_{\odot}$ above which galaxy are predominantly red, bulge-dominated, gas-poor, and hosted in massive dark matter haloes ($M_{halo} \sim 10^{12} M_{\odot}$). Below this mass, galaxies are generally blue, disk-dominated, gas-rich, and star forming (e.g. Kauffmann et al. 2003; Baldry et al. 2004; Kannappan 2004). This mass threshold also corresponds to a 'knee' in many scaling relations, such as colour-mass, size-mass, and star formation rate-mass, where the slope of the relation changes and galaxies begin to form a more homogeneous population. The existence of such a threshold suggests a mass-dependent regulation of star formation, driven by different feedback mechanisms. At low masses, stellar feedback (from supernovae and stellar winds) is thought to be efficient in suppressing star formation. At high masses, AGN feedback becomes dominant, heating or expelling gas and preventing further accretion and disk growth (Dekel & Birnboim 2004). This feedback-driven transition helps explain both the quenching of massive galaxies and the maintenance of the red sequence at the bright end. In summary, the bimodal nature of the galaxy population, consistently observed from the local Universe to $z \sim 2-3$, reflects the interplay between stellar mass, star formation history, morphology, and feedback processes. The observed colour and mass bimodality distribution that separates blue, star-forming galaxies from red, quies-

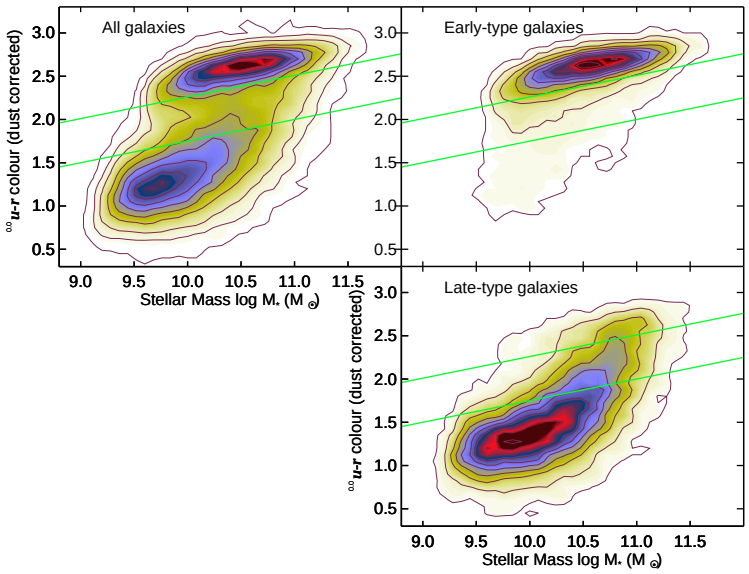

Figure 1.3: Dust corrected $u - r$ colour as a function of the stellar mass of a sample of local galaxies from SDSS. The left panel shows the colour-mass distribution of all galaxies. The right panels show the colour-mass distribution for early- and late-type galaxies, respectively. Figure taken from Schawinski et al. (2014)

cent systems, provides fundamental constraints for theoretical models of galaxy formation and evolution.

1.2.3 Evolution in the cosmic star formation activity

One of the most fundamental observables to trace the growth of galaxies over cosmic time is the cosmic star formation rate density, commonly denoted as $\psi(z)$. This quantity measures the average star formation rate per unit comoving volume at a given redshift and provides a global view of how actively galaxies form stars at different epochs. The resulting diagram, shown in Figure 1.5 widely referred to as the 'Madau plot' (Madau et al. 1996; Madau & Dickinson 2014), is one of the cornerstone results of extragalactic astronomy.

Observational data from a variety of multiwavelength surveys have established a consistent picture: $\psi(z)$ increases rapidly from the early Universe ($z \geq 8$), reaching a peak around $z \sim 2$, when the Universe was approximately 3.5 Gyr old. This epoch corresponds to the so-called 'cosmic noon', during which the star formation activity of the Universe was at its highest. After this peak, the star formation density steadily declines by more than an order of magnitude towards $z = 0$, following a rough scaling of $\psi(z) \approx (1 + z)^{2.7}$. The shape of this curve reflects a complex interplay between the availability of cold gas, the efficiency of its conversion into stars, and the regulation imposed by various feedback processes. Several studies have shown that the decline in $\psi(z)$ at $z < 2$ mirrors the observed decrease in the molecular gas fraction in galaxies (e.g. Tacconi et al. 2013; Genzel et al. 2015), suggesting that the diminishing gas reservoirs in galaxies are a key factor in suppressing star formation at late times.

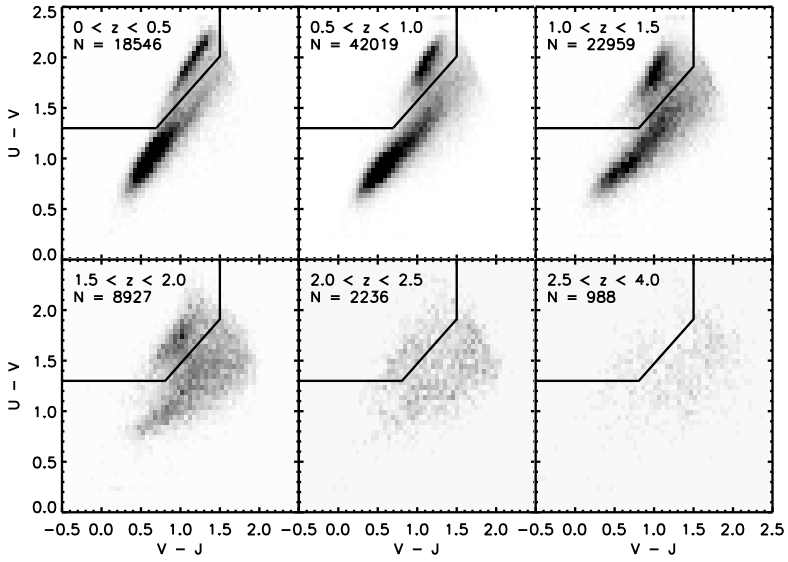

Figure 1.4: Rest-frame $U-V$ vs. $V-J$ colours of a magnitude selected sample of galaxies in five redshift bins. The gray scale represents the density of points in the central region of each plot, while scattered points are plotted individually. The solid lines show the adopted divisions between star-forming and passive galaxy samples at each redshift. Figure taken from Muzzin et al. (2013a)

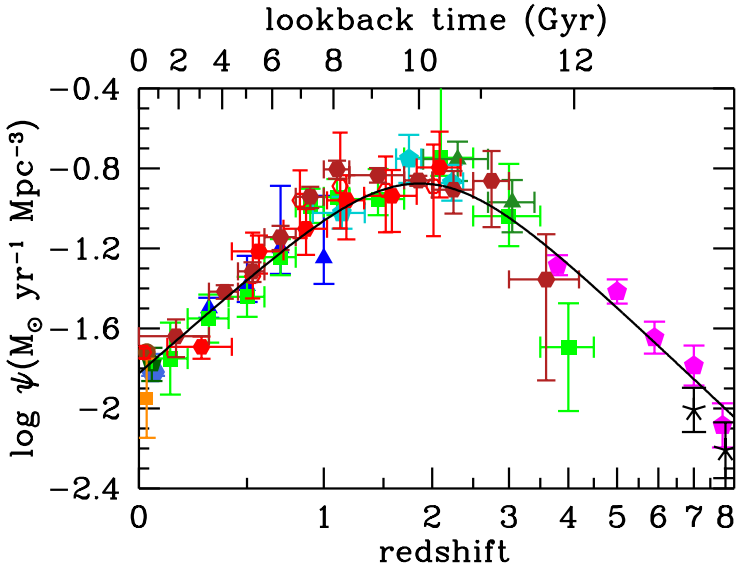

Figure 1.5: The history of cosmic star formation from a compilation of measurements of the star formation rate from $z = 0$ to $z = 8$. Figure taken from Madau & Dickinson (2014).

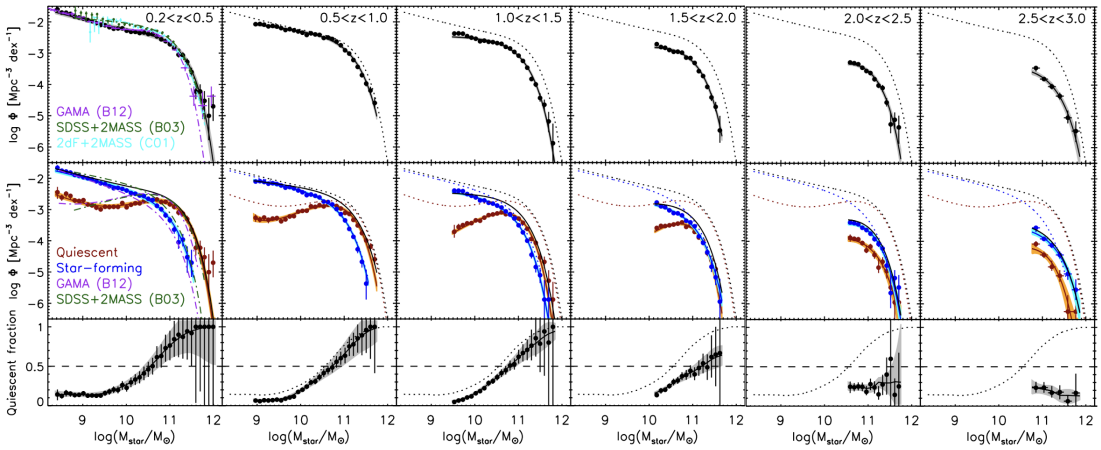

Figure 1.6: Top panels: the stellar mass function of galaxies at different redshifts. Middle panels: the stellar mass function for star-forming and quiescent galaxies in the same redshift bins. Lower panels: The fraction of passive galaxies as a function of stellar mass. The passive fraction correlates significantly with stellar mass, at fixed mass, it is lower at increasing redshift. Figure taken from Muzzin et al. (2013a).

At any given epoch, most of the stars form in galaxies that occupy a tight straight line in the plane SFR-mass, the so-called star-forming main sequence (MS), a tight correlation between SFR and stellar mass. The normalisation of the MS relation evolves strongly with redshift, increasing by nearly a factor of 20 from $z = 0$ to $z \sim 2$, with the high mass end of the curve becoming flatter in the same redshift range (Whitaker et al. 2014). This flattening has been interpreted as a consequence of bulge or bar growth in massive galaxies, which stabilises the gas and suppresses local star formation activity (Gavazzi et al. 2015; Erfanianfar et al. 2016). A small fraction of galaxies ($\sim 1-2\%$) lie above the main sequence and are classified as starburst systems, but they contribute only marginally ($\sim 10\%$) to the global star formation budget (Rodighiero et al. 2011; Sargent et al. 2012). On the opposite end, a growing population of quiescent (and then quenched) galaxies emerges over time. These galaxies exhibit star formation rates much lower than their MS counterparts and become increasingly common at $z \leq 2$. The transition from a star-forming to a quiescent state reflects the cumulative impact of both internal (e.g. AGN feedback, stellar winds) and external (e.g. environmental effects, gas stripping) mechanisms. As a result, the cosmic decline in star formation is not solely due to reduced activity in star-forming galaxies, but also to the increasing prevalence of passive galaxies that no longer contribute significantly to $\psi(z)$. Qualitatively, there is consensus that massive galaxies are mostly quiescent at $z \sim 0$, while were almost entirely star-forming at $z \geq 2$ (see Figure 1.6, Muzzin et al. 2013a).

Altogether, the evolution of cosmic star formation activity encodes key information about galaxy formation and evolution. It reflects the balance between gas accretion, star formation efficiency, and feedback regulation. Discrepancies between the observed stellar mass density and the time-integrated SFR suggest that additional factors, such as systematic uncertainties in SFR indicators, dust attenuation, or a varying IMF, may still play a role.

1.3 Stellar populations in galaxies

The stellar populations of galaxies encode the integrated history of their star formation and chemical enrichment processes. Understanding how these populations form and evolve requires combining a theoretical framework of stellar and chemical evolution with the observational diagnostics that allow us to reconstruct the star formation history of a galaxy from its emitted light.

In the early Universe, only hydrogen, helium, and trace amounts of lithium were produced through primordial nucleosynthesis. The formation of heavier elements, collectively referred to as 'metals', only began with the first generation of stars. Inside them, thermonuclear reactions progressively synthesise heavier elements, with the yield depending on stellar mass and evolutionary stage. Massive stars ($M \geq 8M_{\odot}$) evolve rapidly ($\sim 10-100$ Myr) and end their lives as core-collapse supernovae (Type II SNe), enriching the interstellar medium (ISM) with so-called α-elements (e.g., O, Mg, Si, Ca). In contrast, Type Ia supernovae, which originate from long-lived, lower-mass progenitors in binary systems, are the main producers of iron-peak elements, and release their products on longer timescales (~ 1 Gyr). This delayed enrichment is critical: the relative abundances of α-elements and iron reflect the duration of star formation in a galaxy. Another key ingredient in stellar evolution and chemical feedback is the initial mass function (IMF), which describes the mass distribution of stars at birth. The IMF is a key concept for understanding the baryonic cycle in galaxies. It links the small-scale physics of stellar evolution to the large-scale processes of galaxy formation (see e.g., Kroupa & Jerabkova 2019, for a recent overview). A top-heavy IMF leads to enhanced production of metals and α-elements, while a bottom-heavy one reduces overall yields and alters the mass-to-light ratio. Whether the IMF is universal or environment or mass dependent is still debated, but its shape has profound implications for interpreting the light of a galaxy and estimating stellar mass and chemical enrichment. However, measuring the IMF outside the Milky-Way has proven to be particularly challenging (e.g., Smith 2020).

1.3.1 Star formation regulation and drivers of galaxy quenching

The processes described above set the stage for the chemical evolution of galaxies. However, fully characterising the star formation activity across cosmic time also requires understanding how galaxies dynamically regulate their gas reservoirs and star formation rates. An intuitive and empirical framework has been provided by Lilly et al. (2013), and it links the inflow of baryons into galaxies to their SFR and gas depletion mechanisms, to explain the mass growth and star formation quenching of galaxies across cosmic time. Figure 1.7 illustrates the gas-regulated model presented by Lilly et al. (2013). The model builds on the observation that the specific star formation rate (sSFR) and the specific dark matter accretion rate exhibit a similar redshift evolution. Assuming that baryons trace the dark matter when accreted from the cosmic web, the amount of gas available for star formation is directly connected to the cosmological inflow rate. In this scenario, a galaxy consists of two main components: a long-lived stellar mass reservoir, and a dynamic gas reservoir, which evolves through inflow, star formation, stellar mass return, and outflows. The star formation rate is assumed to scale linearly with the gas mass through the integrated Kennicutt-Schmidt law (Schmidt 1959; Kennicutt 1998):

$$SFR = \epsilon \times M_{gas} \tag{1.1}$$

where ϵ is the star formation efficiency. A fraction ($\sim 40\%$) of the stellar mass formed is returned to the gas-phase via stellar winds and supernovae, enriching the ISM. At the

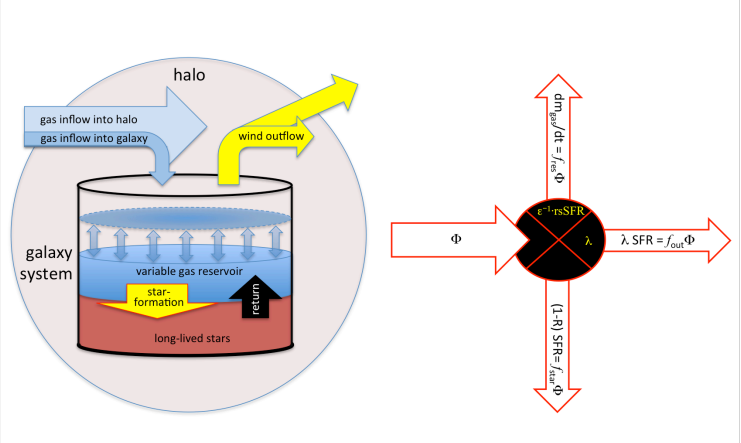

Figure 1.7: Illustration of the gas-regulated model presented by Lilly et al. (2013), in which the SFR is regulated by the mass of gas in a reservoir within the galaxy. The diagram on the right shows, the net flows through the system.

same time, powerful stellar and AGN-driven winds eject part of the gas from the galaxy. These outflows are modeled as:

$$\Psi = \lambda \times SFR \tag{1.2}$$

where λ is the mass-loading factor. The competition between inflows, outflows, and star formation defines the evolution of the gas reservoir and, consequently, the SFR. When the reservoir is exhausted or heating mechanisms prevent cooling and condensation (e.g. through feedback), star formation is quenched, and the galaxy transitions from the star-forming main sequence to the passive population.

From an observational perspective, quenching correlates with several internal galaxy properties, such as stellar mass (Kauffmann et al. 2003; Baldry et al. 2004) and velocity dispersion (Smith et al. 2009; Graves et al. 2009), which relate to the depth of the gravitational potential. More massive galaxies are significantly more likely to be quiescent compared to their lower-mass counterparts. This observational evidence is known as 'mass quenching' (Peng et al. 2010). Although the specific physical cause remains debated, several mechanisms have been proposed, such as AGN feedback, where radiation and jets from a central black hole heat or expel gas (Bower et al. 2006; Croton et al. 2006), major mergers, which trigger central starbursts and exhaust the cold gas (Hopkins et al. 2006; Wilman et al. 2013), and disk instabilities, which build massive bulges and suppress further gas inflow (Dekel et al. 2009).

In addition to internal mechanisms, the role of galaxy environment has long been recognised as a key factor in regulating star formation. First studies revealed a strong morphology-density relation, whereby late-type, star-forming galaxies dominate low-density regions, while early-type, quiescent galaxies are more prevalent in dense environment, such as galaxy clusters (Dressler 1980; Postman & Geller 1984; Dressler et al. 1997). Indeed, HI surveys have shown that spiral galaxies in clusters are often significantly deficient in neutral hydrogen compared to isolated systems of similar mass and size (Haynes & Giovanelli 1984; Giovanelli & Haynes 1985). The reduced gas reservoir in galaxies that enter in denser environment can be attributed to external processes, such as ram-pressure stripping (Gunn & Gott 1972), strangulation (Larson et al. 1980; Balogh et al. 2000), tidal interaction (Merritt 1984), and galaxy harassment (Moore et al. 1998), all of which are more effective in high-density environments (Boselli & Gavazzi 2006; Blanton & Moustakas 2009). Figure 1.8 shows a clear evidence that the mass and environmental quenching are

at first approximation separable and independent processes

The imprint of these quenching processes is preserved in the stellar populations of galaxies. The ages, metallicities, and abundance ratios of stars provide a fossil record of the duration, intensity and chemical evolution of star formation. In this context, stellar population diagnostics become an essential tool to reconstruct the past star formation activity and to distinguish between different evolutionary pathways.

1.3.2 Stellar populations as fossil records of galaxy evolution

While theoretical models provide a framework for understanding how galaxies form and evolve, observational studies must infer this history indirectly, from the properties encoded in their stellar populations. These properties can be probed through the integrated light of galaxies, which carries information on the age, chemical composition, and formation timescales of their stars. The evolution of stellar populations, shaped by star formation rates, the IMF, and chemical enrichment, ultimately defines the spectral and photometric properties we observe in galaxies. In our studies, we rely on a set of integrated diagnostics that encode this information: age, metallicity, and abundance ratios.

- **Age**. The age of a stellar population provides a constraint on the main epoch of star formation. Because the Universe was denser in the past, older stellar populations are expected to have formed in more compact systems. Thus, measuring stellar ages helps to trace not only when galaxies formed their stars, but also how their structural properties evolved (e.g. through mergers or internal processes). Real galaxies host multiple stellar populations depending on their evolution. Different stellar populations emit most of their light in distinct wavelength regions, therefore the inferred age traces different pieces of the star-formation history;

- **Metallicity**. The metallicity reflects both the efficiency and duration of star formation, and the ability of a galaxy to retain metals against outflows. High stellar metallicity implies enriched ISM at the time of star formation, usually resulting from intense or repeated star formation episodes. Gas-phase metallicity, often inferred from emission lines (e.g. Oxygen), traces current ISM enrichment. In contrast, stellar metallicity, derived from absorption features (especially Mg and Fe lines), records the metallicity of the gas at the epoch when the stars were formed. Since stars retain their original chemical composition over time, they provide a fossil record of the ISM enrichment history.

- **[α/Fe] ratio**. The abundance ratio of α-elements to iron is a powerful diagnostic of star formation timescales. A high [α/Fe] indicates that the bulk of star formation occurred quickly, before Type Ia SNe contributed significant iron, and is thus typical in ETGs. This ratio also varies with environment and galaxy mass, offering insights into quenching processes.

From an observational perspective, several studies have demonstrated that stellar populations provide powerful constraints on the star formation histories of galaxies (e.g. Gallazzi et al. 2005; Thomas et al. 2010). By measuring key parameters described above, such as age, metallicity, and abundance ratios, it is possible to infer not only when stars formed, but also how rapidly the star formation proceeded and when it was quenched. At low redshift, these studies found strong correlations between stellar population properties and galaxy velocity dispersion, indicating that more massive galaxies formed their stars earlier and over shorter timescales. A dependence on environment is also observed,

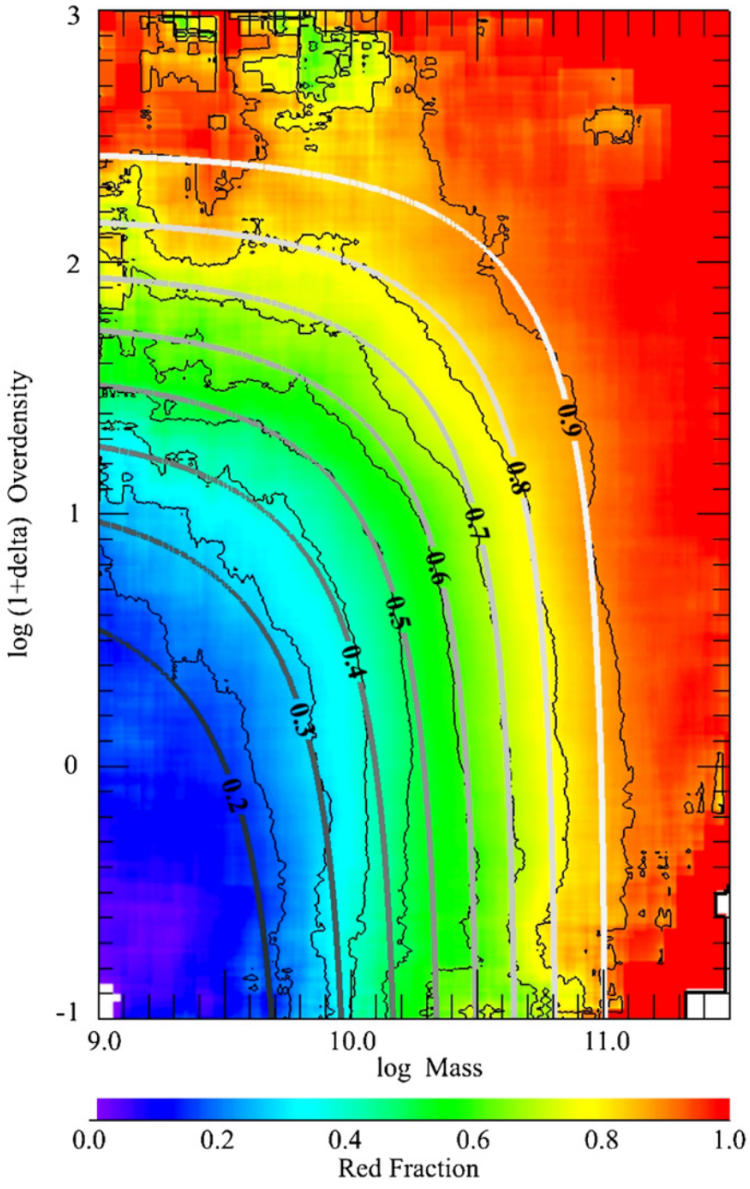

Figure 1.8: The fraction of passive galaxies in SDSS as a function of stellar mass and environmental density. Figure taken form Peng et al. (2010).

suggesting that galaxies in dense regions quenched earlier than their counterparts in the field. These evidences reinforce the idea that integrated stellar populations encode essential information about galaxy formation and evolution. Because these properties evolve in a predictable way depending on the duration and mode of star formation, they allow us to distinguish between galaxies quenched rapidly (e.g., via mergers or environmental stripping) and those with extended star formation histories. Moreover, their dependence on mass and environment makes them uniquely suited to disentangle the relative contribution of internal and external mechanisms in shaping galaxy evolution. Finally, when measured statistically across large galaxy samples, stellar population diagnostics can be used to probe the dependence of the star formation history on mass, morphology, redshift, and environment, thus providing a critical benchmark for testing theoretical models at the population level.

1.4 Modeling the evolution of the stellar content of galaxies

Outside the immediate neighbourhood of the Milky Way, current telescopes cannot resolve individual stars in galaxies. As a result, galaxies must be studied through their integrated light, or spectral energy distribution (SED), which encodes information about their global physical and stellar population properties. The light we observe from a galaxy is therefore the combined emission of its stars, each one characterised by a mass, age, and metallicity. Since the 1970s, researchers have developed increasingly sophisticated tools to interpret observed SEDs by comparing them with predictions from synthetic galaxy models. This process is known as stellar population synthesis (SPS). At its core, SPS modeling is conceptually straightforward: the SED of a galaxy is modeled as the combination of its luminous components, such as stars, gas, and dust, each contributing to the overall spectrum in a distinct way. Dust in galaxies absorbs and scatters stellar light, preferentially attenuating the blue and ultraviolet part of the spectrum and thus reddening the observed stellar continuum. As a result, dust attenuation must be included as an additional ingredient in stellar continuum modeling, with its impact depending on both the dust properties and its spatial distribution relative to the stars. In practice, the global effect of dust is often accounted for by adopting an empirical attenuation law (e.g. Charlot & Fall 2000; Calzetti 2001). Nebular emission lines in galaxies originate from gas ionised by massive, short-lived stars, and are therefore present only in systems with ongoing or very recent star formation. The relative strengths of metal lines depend primarily on the gas-phase metallicity, making them sensitive probes of the chemical composition of the interstellar medium. Modeling nebular emission requires additional assumptions on the spatial distribution of star-forming regions, the chemical composition of the gas, and ultimately depends on the underlying stellar emission models, and thus on all parameters that govern the modeling of stellar populations.

Given this brief description of the dust and gas components, in this thesis we will focus primarily on the modeling of stellar emission. The stellar component is typical constructed from simple stellar populations (SSPs), which represent an idealised group of coeval stars formed in a single, instantaneous burst from gas with uniform metallicity and elemental abundances. Building an SSP requires setting the following ingredients:

- **Isochrones**. It essentially describes how stars evolve across the Hertzsprung-Russell diagram, which plots stellar luminosity against temperature. In a Simple Stellar Population (SSP), isochrones trace the evolutionary stages of stars of different masses at a fixed age, effectively capturing a snapshot of the population at a given time. They indicate which stars are present, their evolutionary phase, and the fraction of

the total stellar mass they represent (i.e., the relative weight of that phase). Since the spectral characteristics of a star change throughout its life, and its mass plays a key role in the history and nature of its evolution, isochrones are fundamental tools for modeling the integrated light of stellar populations.

- **Stellar library.** It is a collection of stellar spectra that, when combined according to a model's recipe, produces the expected spectrum of a stellar population. These libraries can be **empirical**, based on observations of real stars, or **theoretical**, constructed from models based on the stellar evolution theory.

  The stellar empirical spectra are inherently incomplete, as they rely on stars within the Solar neighbourhood. This restricts the parameter space they cover, especially in terms of chemical abundances and peculiar evolutionary stages, that may significantly influence the galaxy spectrum. In addition, they are constrained by the instrumental capabilities of the telescopes and spectrographs used to obtain the data, leading to limited wavelength coverage and resolution.

  The theoretical spectra, on the other hand, offer greater flexibility. They can be generated for any combination of physical stellar parameters, i.e. surface temperature, gravity, and chemical composition, on the basis of the stellar evolution theory. They provide a full wavelength coverage and can efficiently reproduce the spectral continuum. However, they have their own limitations, primarily due to uncertainties in stellar physics. These include challenges in modeling convection, the limited applicability of local thermodynamic equilibrium (LTE) assumptions, and incomplete or inaccurate atomic and molecular line strengths.

- **Metallicity**. The metallicity of the initial nebular cloud from which the stars formed is a key parameter in stellar population modeling. It is defined as the fraction of mass of elements heavier than helium. It has a strong impact on the resulting synthetic spectrum, influencing both the shape of the continuum and the depth of specific absorption lines. In particular, stars with higher metallicity exhibit slightly redder spectral continua compared to metal-poor stars. As a result, increasing the metallicity of a stellar population leads to an overall reddening of its integrated light. However, a similar reddening effect is also caused by the ageing of the stellar population, giving rise to the well-known age-metallicity degeneracy, which complicates the interpretation of spectral features.

- **Initial Mass Function (IMF)**. It describes the distribution of stellar masses at the time of their formation and plays a crucial role in determining the evolution of the spectrophotometric properties of the stellar populations. It directly influences the mass-to-light ratio (M/L) and, consequently, the stellar luminosity evolution of a galaxy. Indeed, massive stars (M $> 2M_{\odot}$) evolve rapidly, exhausting their fuel in less than a Gyr and ceasing to contribute significantly to the light of a galaxy, in particular in the blue/ultraviolet region of the spectrum. In contrast, low-mass stars (M $< 1M_{\odot}$) evolve slowly and dominate the integrated light of old stellar populations, in particular in the optical/infrared region of the spectrum.

  Historically, the IMF was first estimated by Salpeter (1955) through direct star counts in the Milky Way, finding a power-law slope of ~ 2.35 for stars with M $> 0.4M_{\odot}$. Subsequent studies extended this to lower masses with flatter slopes (e.g. Kroupa 2001; Chabrier 2003), leading to the widely adopted bimodal IMFs. These results, observed across different regions of the Galactic disk, supported the notion of a universal IMF, constant across galaxy types and cosmic times. However,

this assumption has increasingly been challenged. For extragalactic systems, where individual stars cannot be resolved, the IMF must be inferred from the integrated light. This introduces strong degeneracies with other properties, such as age and metallicity of the stars. Recent studies, particularly of early-type galaxies (ETGs), suggest a bottom-heavy IMF in more massive systems, implying a higher proportion of low-mass stars compared to the Milky Way. Despite strong theoretical motivations and growing observational evidence challenging the universality of the IMF (e.g. Bastian et al. 2010; Kroupa et al. 2013), our limited ability to constrain it directly still forces many stellar population models to assume a fixed IMF.

Once the SED of an SSP is known, a composite stellar population (CSP) can be built by combining multiple SSPs according to a given star formation history (SFH) and chemical enrichment history, which describe how the stellar mass and metallicity evolve over time.

In summary, SPS models are powerful tools for interpreting the spectrum of a galaxy, but their accuracy is ultimately limited by the quality and completeness of their fundamental ingredients. Understanding these limitations is crucial when using such models to derive galaxy properties from observational data.

1.4.1 Stellar population models

Although the SPS framework is well established, several practical challenges remain. As described above, these include incomplete or uncertain isochrone tables, limited coverage and resolution of empirical stellar libraries, and poorly calibrated physical processes, particularly at low and very high metallicity or for advanced stellar evolutionary phases. Moreover, each input can itself depend on metallicity and abundance patterns, introducing further complexity and potential model-dependent biases. There have been different attempts on modeling SSPs, and we present the ones used in this thesis:

- **CB**19 **models**. They are the latest version of the Bruzual & Charlot (2003) models (see Plat et al. 2019; Sánchez et al. 2022), based on the PARSEC evolutionary tracks (Marigo et al. 2013; Chen et al. 2015). This set of models is provided for different IMFs, assuming $M_{UP} = 100 M_{\odot}$, that is the maximum mass of the stars in the IMF. The models extend from 91Å to 36000μm and are based on a combination of theoretical and empirical stellar libraries: the Tlusty library (Lanz & Hubeny 2003a,b, 2007) in the UV, the MILES stellar library ($3540.5 < \lambda < 7350.2$Å Sánchez-Blázquez et al. 2006; Falcón-Barroso et al. 2011, 2.5Å FWHM), the Indo-US library in the NIR, and a combination of stellar libraries in the IR ($\lambda \geq 9410$Å): BaSeL 3.1 (Westera et al. 2002), Aringer (Aringer et al. 2009), IRTF (Villaume et al. 2017), Dusty models and TP-AGB (Nenkova et al. 2000; González-Lópezlira et al. 2010). For each IMF, the CB19 set of models provides 3300 SSPs unevenly spaced in linear age and [Z/H], covering 220 ages from 0.01 Myr to 14 Gyr and 15 metallicities from [Z/H] $= -2.23$ to [Z/H] $= 0.55$ dex; for reference, the solar abundance ($Z_{\odot}$) is 0.017.

- **E-MILES models** They are an extended version of the MILES stellar population models from Vazdekis et al. (2016), covering the spectral range from 1680Å to 5μm based on fully-empirical stellar libraries: the NGSL (Gregg 1994) for the UV, the MILES, Indo-US (Valdes et al. 2004), and CaT (Cenarro et al. 2001) libraries in the optical, and the IRTF library in the infrared, with a spectral resolution varying from 2.51Å to 23.54Å FWHM, depending on the wavelength range and the relative spectral library.

- **sMILES models**. They are semi-empirical SSPs from Knowles et al. (2023) and the state-of-the-art in [Mg/Fe] abundance resolution. The SSP models adopt the BaSTI evolutionary tracks and the MILES empirical library. They are realised with different IMFs, and for each one the models provides 2650 SSPs unevenly spaced in linear age and [Z/H], covering 53 ages from 0.03 Gyr to 14 Gyr, 10 metallicities from [Z/H] = −1.79 to [Z/H] = 0.26 dex, being the solar abundance $Z_{\odot} = 0.0198$, and five [Mg/Fe]abundances from −0.2 to 0.6 dex. The main limitation is related to the limited wavelength coverage, as it covers only the optical region.
- **TMJ models**. They are models from Thomas et al. (2011). These models are based on the Cassisi evolutionary tracks (Cassisi et al. 1997) and the MILES empirical stellar library. The models assume a Kroupa initial mass function. The synthetic library provides predictions of 25 indices for each SSP. The SSPs are unevenly spaced in linear age and [Z/H], covering 20 ages from 0.1 Gyr to 15 Gyr, 6 metallicities from [Z/H] = −2.25 to [Z/H] = 0.67 dex, and five [α/Fe] abundance ratio from −0.3 to 0.5 dex.

As outlined above, there are various approaches to modeling SSPs, each with its own strengths and limitations. It is therefore essential to understand these differences and choose the most suitable models based on the specific goals of the analysis.

1.5 Methods to estimate the stellar population parameters

In this Section we present an overview of the main methods used to study the stellar population parameters. All of them rely on comparing the observations with the predictions of stellar population models. As will be shown in the following chapters, this comparison can be implemented in different ways.

1.5.1 Absorption-line indices

The contribution of each stellar class to the integrated spectrum of a stellar population varies as a function of wavelength. Specifically, the signature of a given stellar class can be isolated at the wavelengths corresponding to particular absorption lines. Consequently, the analysis of absorption features in a galaxy's spectrum serves as a powerful diagnostic tool to extract selective information about the composition and evolutionary status of its stellar population. Burstein et al. (1984) introduced a system of spectral indices known as the Lick/IDS system, later defined by Worthey et al. (1994). These indices quantify the strength of absorption lines at given wavelengths, normalised with respect to the local continuum, and are widely used to study the stellar populations of galaxies. The absorption lines for atomic transitions are expressed in Å, while the features due to molecular transitions are in magnitudes. Following Worthey (1994) and Trager et al. (2000), a spectral index is calculated as:

$$I_a = \int_{\lambda_{I_1}}^{\lambda_{I_2}} \left(1 - \frac{F(\lambda)}{C(\lambda)}\right) d\lambda \tag{1.3}$$

$$I_m = -2.5 log_{10} \frac{\int_{\lambda_{I_1}}^{\lambda_{I_2}} \left(\frac{F(\lambda)}{C(\lambda)}\right) d\lambda}{\lambda_{I_2} - \lambda_{I_1}} \tag{1.4}$$

where I_a and I_m are the atomic and molecular index, respectively. The wavelength limits of the feature band-pass are λ_{I_1} and λ_{I_2}, $F(\lambda)$ is the flux per unit wavelength of the feature

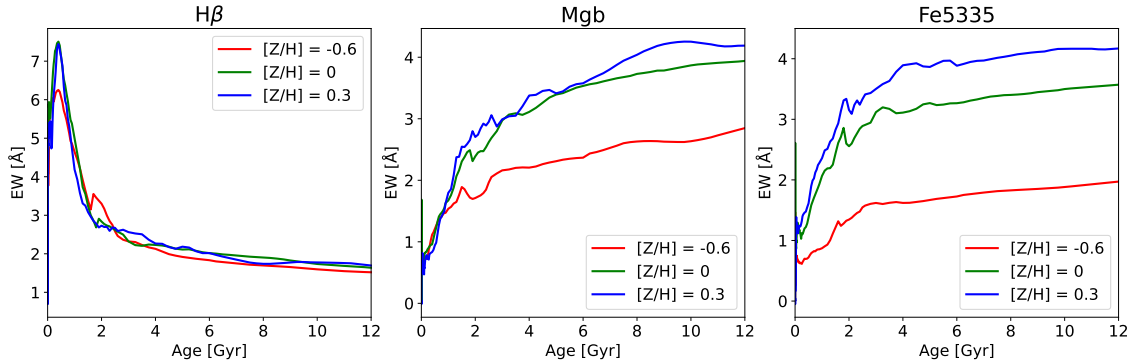

Figure 1.9: Distribution of Hβ (left panel), Mgb (middle panel) and Fe5335(right panel) values as function of the age for three different metallicities, using the CB19 SSPs.

and $C(\lambda)$ is the value of the pseudo-continuum obtained interpolating the mean values of the blue and red band-passes. The definitions of the indices used in this thesis are shown in Table 1.1. Figure 1.9 shows an example of indices sensitive to age and metallicity as function of the age for three different metallicities, using the CB19 SSPs.

Spectral indices are particularly effective in constraining stellar ages and metallicities. Their sensitivity to stellar temperature and chemical composition allows to probe both the age (through temperature-dependent features, such as the Balmer lines) and the metal content (through chemical abundance dependent features, such as Fe and Mg lines). However, both parameters (i.e., the age and metallicity of the stellar population) influence the strength of the resulting spectral absorption lines, giving rise to the well-known age-metallicity degeneracy. This can be mitigated by selecting an appropriate combination of indices that respond differently to age and metallicity.

One major advantage of using absorption line indices is that they are largely insensitive to dust extinction and flux calibration issues, unlike approaches that rely on the stellar continuum of the spectrum. This is especially advantageous when analysing young stellar populations, where the typically abundant dust can obscure key spectral features. Since dust, age, and metallicity all tend to redden the spectrum in similar way, minimising the impact of dust effectively removes one source of degeneracy in the analysis. However, a practical caveat is that line-strength indices are sensitive to additive residuals. Indeed, imperfect background/sky subtraction, scattered light, or residual continuum from neighbouring sources can fill in absorption features or distort the pseudo-continuum, biasing the measured indices. Rigorous background removal and masking of sky-line residuals are therefore essential.

Although the Lick/IDS indices remain the most commonly used, studies of galaxies at higher redshifts shifts the focus to the rest-frame ultraviolet. This has expanded the toolkit for stellar population diagnostics to include a broader set of UV and optical indices.

1.5.2 Full spectral fitting

The full spectral fitting technique is a widely used technique for deriving both stellar population properties and kinematics of galaxies. Unlike the index-based analyses, which focus on specific spectral features, the full spectral fitting leverages the entire observed spectrum to extract information. This approach is particularly efficient and powerful for measuring kinematic parameters, such as velocity dispersion and redshift, benefiting from the broad wavelength coverage and high number of fitted data points (Cappellari &

Table 1.1: List of spectral indices.

Index	Blue pseudocontinuum	Central feature	Red pseudocontinuum	Ref.
FeII2402	2285.0-2325.0	2382.0-2422.0	2432.0-2458.0	1
BL2538	2432.0-2458.0	2520.0-2556.0	2562.0-2588.0	1
FeII2609	2562-2588	2596-2622	2647-2673	1
BL2720	2647-2673	2713-2733	2762-2782	2
BL2740	2647-2673	2736-2762	2762-2782	2
Mg2852	2818-2838	2839-2865	2906-2936	1
Fe3000	2906-2936	2965-3025	3031-3051	1
BL3096	3031-3051	3086-3106	3115-3155	1
BL3580	3500.0 3540.0	3540.0-3600.0	3620.0-3650.0	1
Fe3619	3594.0-3602.0	3602.0-3623.5	3623.5-3628.5	3
Fe3741	3693.5 3700.0	3701.0 3772.0	3775.0 3784.0	3
CaK	3845.0-3880.0	3925.65-3945.0	3950.0-3954.0	4
CaH	3950.0-3954.0	3959.40-3978.0	3983.0-3993.0	4
Dn4000	3850-3950	-	4000-4100	5
FeBand	4014.0-4025.5	4025.5-4085.0	4085.0-4093.0	3
Hδ_F	4057.25-4088.50	4091.00-4112.25	4114.75-4137.25	6
Hγ_F	4283.50-4319.75	4331.25-4352.25	4354.75-4384.75	6
Gband4300	4266.375 4282.625	4281.375 4316.375	4318.875 4335.125	7
Fe4383	4359.125-4370.375	4369.125-4420.375	4442.875-4455.375	7
Ca4455	4445.875 4454.625	4452.125 4474.625	4477.125 4492.125	7
Fe4531	4504.250 4514.250	4514.250 4559.250	4560.500 4579.250	7
$H\beta_o$	4821.175-4838.404	4839.275-4877.097	4897.445-4915.845	8
Fe5015	4946.500 4977.750	4977.750 5054.000	5054.000 5065.250	7
Mgb	5142.625-5161.375	5160.125-5192.625	5191.375-5206.375	7
Fe5270	5233.150-5248.150	5245.650-5285.650	5285.650-5318.150	7
Fe5335	5304.625-5315.875	5312.125-5352.125	5353.375-5363.375	7
Fe5406	5376.250 5387.500	5375.500 5415.000	5415.000 5425.000	7
Fe5709	5672.875 5696.625	5696.625 5720.375	5722.875 5736.625	7

(1) Fanelli et al. (1992); (2) Chavez et al. (2007); (3) Gregg (1994); (4) Borghi et al. (2022); (5) Balogh et al. (1999); (6) Worthey & Ottaviani (1997); (7) Worthey et al. (1994); (8) Cervantes & Vazdekis (2009).

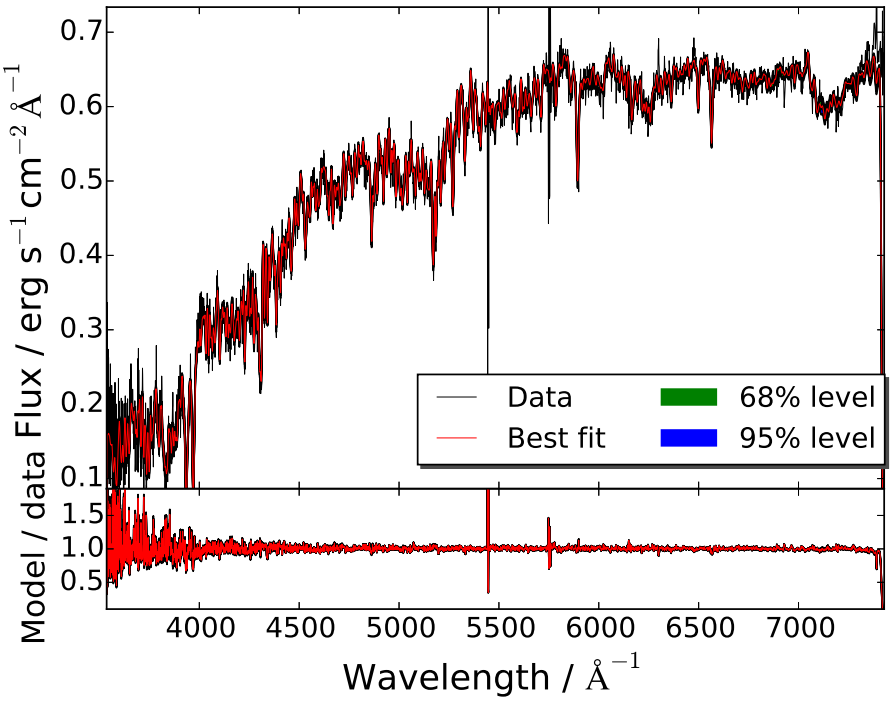

Figure 1.10: Example of full spectral fitting (red) of a typical SDSS DR7 galaxy spectrum (black) with 68% and 95% confidence intervals in shaded green and blue respectively, with the residuals plotted underneath. Image taken from Wilkinson et al. (2017).

Emsellem 2004; Cappellari 2023). Figure 1.10 shows an example of a full spectral fitting performed with FIREFLY from Wilkinson et al. (2017).

The full spectral fitting offers several advantages for recovering stellar population parameters. First, the large number of spectral pixels being fitted improves statistical robustness, which is especially valuable when dealing with low S/N spectra. Second, it captures the information embedded in the spectral continuum, which can be sensitive to effects like dust attenuation and overall spectral shape, factors that are typically excluded in the index-based method. This makes the full spectral fitting in general well-suited for deriving an overview of the SFH of galaxies. However, the method also presents some limitations. Since the fitting process minimises the χ^2 over the entire spectrum, it may fail to reproduce individual narrow spectral features with high accuracy, especially those associated with specific elemental abundances. As a result, because full spectral fitting gives comparable weight to all pixels in the spectrum, it may fail to recover properties whose signatures are confined to specific absorption features, which represent only a small fraction of the total data points. In such cases, index-based methods can be more effective. Another limitation is its sensitivity to parameter degeneracies. Indeed, the full spectral fitting requires assumptions about a larger number of parameters than the index fitting approach, and the classic age–metallicity–dust degeneracy is especially hard to break. This problem is compounded by imperfect relative flux calibration. Even mild continuum-shape errors can mimic dust attenuation or stellar population, biasing the inferred ages, metallicities, and extinctions. Therefore this method requires an accurate flux calibration. In the context of galaxy studies, the full spectral fitting has become a standard tool in large spectroscopic surveys (e.g. Wilkinson et al. 2017; Carnall et al. 2018; Johnson et al. 2021), allowing for automated extraction of stellar population parameters across vast galaxy samples.

1.5.3 Full-index fitting

The full-index fitting (FIF) method, originally proposed by Martín-Navarro et al. (2014), is an hybrid approach that bridges the gap between the traditional line-strength analysis and full spectral fitting. The key idea is to focus on a carefully selected set of spectral features that are particularly sensitive to specific stellar population parameters, and to perform a pixel-by-pixel fit within the bandpasses of those features, rather than averaging over them as in the classic index approach. FIF generalises the line-strength analysis by preserving the advantage of keeping a reduced number of parameters, thus reducing the computational time, but enhances it by using the full information content of each pixel within the index window. Indeed, each pixel of each index responds differently to changes in stellar population parameters, and the FIF accounts not only for the strength of the absorption feature but also for its detailed shape. This permits to better break degeneracies and to lower the S/N requirements compared to classical methods. Another key technical advantage of FIF is that, since the spectral flux within each index window is normalised using narrow sideband regions, as in the traditional index fitting approach, the method is largely insensitive to large-scale flux calibration issues. Moreover, unlike full spectral fitting, which spreads sensitivity across the entire spectrum (and can dilute the influence of specific features), FIF focuses on spectral regions where the diagnostic power is highest, maximising the extraction of stellar population properties, and even allowing for the measurement of individual elemental abundances that only affect a limited number of lines.

Figure 1.11 shows an example of the FIF approach applied to stacked spectrum from DESI data. The best-fit template closely matches each spectral feature, capturing detailed information from both their depth and pixel-by-pixel shape. In summary, FIF offers a robust compromise, since it retains the computational efficiency and focus of index-based methods while incorporating the richer information content and modeling flexibility of full spectral fitting (see also Martín-Navarro et al. 2019; Martín-Navarro et al. 2021, 2023; Bevacqua et al. 2025).

1.6 My thesis

In this thesis we aim to understand the formation and evolution of galaxies across the last 7 Gyr of the Universe's age through four original studies. These works collectively investigate and exploit the stellar population properties of galaxies across a wide redshift range and diverse environments to gather information on the galaxies assembly history. By testing and applying diverse fit methodologies, from a classic index fitting approach, to an advanced full-index fitting combined with photometric data, this work aims to constrain the star formation histories, chemical enrichment and environmental dependence of massive galaxies. Each project leverages different techniques and addresses different aspects of galaxy formation and evolution, ranging from a mock sample of star-forming and quiescent galaxies at intermediate redshift, quiescent galaxies in different environments at fixed intermediate redshift, an interaction-driven system in the local Universe, to a comprehensive study of massive and passive galaxies across 7 Gyr of the Universe.

As a first step, we follow a quite traditional approach based on classical index fitting technique to assess the ability to accurately estimate the stellar ages and metallicities in galaxies using a set of ultraviolet and optical spectral indices (Chapter 2). This study is designed as a fundamental test for the upcoming WEAVE-StePS survey, which will collect large samples of galaxy spectra at intermediate redshifts ($0.3 < z < 0.7$). We simulate

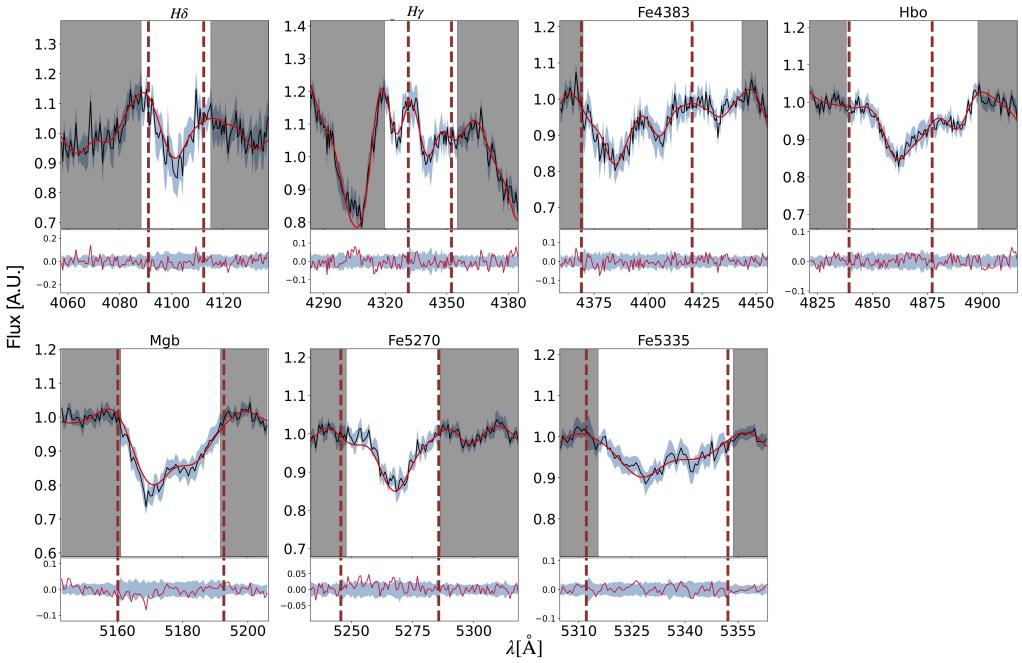

Figure 1.11: FIF application to selected indices in a spectrum. The vertical dashed brown lines indicate the feature boundaries for each index, while the grey shaded regions represent the pseudo-continua used for normalisation. In the upper subplots, the black lines and blue shaded regions correspond to the observed spectrum and its associated uncertainty, respectively. The solid red line represents the best-fit derived from the posterior distribution. The red lines in the lower subplots show the residuals between the observed spectrum and the best fit, with the blue shaded region indicating the relative uncertainties of the observed spectrum.

realistic observations using a comprehensive library of synthetic galaxy spectra, varying parameters such as age, metallicity, and SFH. By applying a Bayesian inference method to the accurately selected spectral indices, we evaluate how well the stellar population parameters can be constrained under different observational conditions. The inclusion of UV indices significantly improves the gathered information about the SFH, particularly at higher redshifts where rest-frame UV features become available. This is a key test to define the probes of the chemical evolution of galaxies across cosmic time.

In Chapter 3 we investigate the recent history of the archetypal collisional ring galaxy: the Cartwheel. By analysing the spatial distribution of its stellar populations, we present a comprehensive analysis that combines integral field spectroscopy from VLT/MUSE with an extensive set of photometric data, ranging from GALEX to JWST/MIRI, with the aim of reconstructing the recent star formation history. In this work, we apply the novel full-index fitting approach to derive precise, spatially resolved stellar population parameters, complemented by a bayesian hierarchical modeling to account for spatial variation in stellar properties. The study demonstrates how detailed stellar population studies can effectively date recent galactic interactions and constrain the physical processes involved.

In Chapter 4 we study the role of environment in quenching the star formation activity in massive galaxies within the COSMOS Wall at $z \sim 0.7$, a large-scale structure encompassing a wide range of environments, from rich and dense clusters down to field-like regions. We leverage high-quality spectroscopic data from the LEGA-C survey, combined with the extensive photometric coverage of the COSMOS2020 catalogue. Then we perform a novel joint full-index and photometric fitting using nested sampling techniques in order to measure the stellar population parameters and the star formation timescale of individual galaxies in different environments. Our results suggest that, even in massive galaxies, the environment plays a role on their quenching, and the study of their stellar populations proves strong hints on different star formation timescales in different environments.

Finally, building on the techniques developed and refined—especially those tailored for large samples with low signal-to-noise ratios—we have analysed the properties of massive quiescent galaxies in the redshift range $0.15 < z < 0.8$ in a uniform way for the first time, both in terms of data quality and methodology. In Chapter 5 we present a comprehensive study on the evolution of the most massive luminous red galaxies (LRGs), exploiting the extensive spectroscopic datasets from the BOSS and DESI surveys across the redshift range $0.15 < z < 0.8$.

In Chapter 6 we summarise our key findings, and we describe the future prospects of this thesis. We discuss future observational facilities, such as WEAVE-StePS and 4MOST-StePS, that will provide new revolutionary datasets to understand the role of mass and environment at intermediate redshift, crucial to understand the galaxy evolution.

Throughout this thesis, we adopt a standard ΛCDM cosmology with $\Omega_M = 0.286$, $\Omega_\Lambda = 0.714$, and $H_0 = 69.6\ \mathrm{km\ s^{-1}\ Mpc^{-1}}$ (Wright 2006; Bennett et al. 2014). Magnitudes are given in the AB system (Oke 1974).

Chapter 2

Stellar age and metallicity from optical and UV spectral indices: test case for WEAVE-StePS

This chapter is adapted from Ditrani et al. 2023, A&A, 677, A93.

As described in Chap. 1.4, estimating stellar population parameters from galaxy spectra is challenging because age, metallicity, dust, and IMF imprint partially degenerate signatures. Large and magnitude-limited statistical studies on stellar populations of galaxies based on spectroscopic data are limited to the low redshift regime. Estimation of stellar population parameters requires spectroscopy with a high signal-to-noise ratio (S/N > 10 Å^{-1}) and moderate to high resolution to trace the key absorption indices that are sensitive to age and metallicity. Moreover, the absorption line indices historically adopted to derive the stellar parameters in low redshift galaxies are mainly located in the optical rest-frame region. At higher redshift, these features move to redder wavelengths, where strong sky emission lines (difficult to subtract accurately) and telluric absorptions (difficult to correct in flux calibration) severely affect the quality of the spectra. Indeed, intermediate-and high-redshift studies based on data of sufficient quality to derive stellar parameters of galaxies are limited to few spectroscopic works, mainly based on cluster galaxies at $z < 1$ (e.g. Jørgensen et al. 2005; Sánchez-Blázquez et al. 2009; Jørgensen & Chiboucas 2013; Ferré-Mateu et al. 2014), with some exceptions in the field (e.g. Ferreras et al. 2009; Gallazzi et al. 2014).

The upcoming generation of spectrographs on four-meter-class telescopes, with their huge multiplexing capabilities, wide wavelength coverage, and moderate spectral resolution, can offer an interesting opportunity to fill in this redshift gap. In particular, the new spectrographs will provide spectra with similar quality of those from SDSS in the local Universe. Two complementary ambitious surveys of $0.3 < z < 0.7$ massive galaxies will start soon: the WEAVE-StePS project on the 4.2m William Herschel Telescope in the Canary Islands (WHT, Dalton et al. 2012; Jin et al. 2023; Iovino et al. 2023b) and the accepted 4MOST-StePS at 4.1m ESO-VISTA in Paranal (de Jong et al. 2019; Iovino et al. 2023a). Thanks to their new-generation spectrographs, both surveys will provide spectra (with S/N > 10Å^{-1}) for hundreds of galaxies in one shot at $R = 5000$, in the observed spectral range from 3660 to 9590Å.

This chapter is the starting point for our study of stellar populations. In this work, we adopt the classical index approach together with a library of templates representative of galaxies at different evolutionary stages to derive the posterior probability distributions of the stellar population parameters. Therefore this chapter presents a methodological test case tailored to these upcoming intermediate-redshift surveys. We evaluated the ability to infer stellar ages and metallicities from UV and optical absorption-line indices measured in realistic, WEAVE-StePS–like spectra. The exploitation of line-strength indices mitigates several systematics by isolating the most diagnostic features and reducing sensitivity to broad-band flux-calibration and dust effects. At the same time, leveraging UV indices adds complementary sensitivity and helps break degeneracies that remain in purely optical analyses. Our approach combines UV and optical indices within a Bayesian framework, using extensive simulations to quantify performance as a function of redshift and signal-to-noise. The goal is to establish a robust, efficient recipe for measuring stellar population parameters in a statistical sample at $0.3 < z < 0.7$.

2.1 Stellar population models

Following Costantin et al. (2019), we used a comprehensive library of spectral templates of stellar populations (Zibetti et al. 2017). The library is based on a revised version of the BC03 models by Bruzual & Charlot (2003).[1]

The new version follows the PARSEC evolutionary tracks (Marigo et al. 2013; Chen et al. 2015) for 16 metallicity values, assuming a solar abundance of $Z_{\odot} = 0.017$. The new tracks include evolution of stars from the main sequence stage to the Wolf-Rayet phase for the most massive stars or to the thermally pulsing asymptotic giant branch (TP-AGB) for stars with mass lower than $6M_{\odot}$. Details on the description of the Wolf-Rayet phase adopted in the models can be found in Appendix A of Plat et al. (2019). For a more detailed description of the new adopted ingredients of the models (cited as C&B), we refer to Appendix A of Sánchez et al. (2022).

We assumed a Chabrier initial mass function (IMF, Chabrier 2003) with $M_{UP} = 100M_{\odot}$ and the MILES stellar library ($3540.5 < \lambda < 7350.2$Å; Sánchez-Blázquez et al. 2006; Falcón-Barroso et al. 2011, 2.5Å FWHM resolution), extended in the UV ($911 < \lambda < 3540.5$Å) with theoretical high-resolution models (Martins et al. 2005, 1Å FWHM, see also Table 12 in Sánchez et al. 2022) . Each simple stellar population (SSP) model provides 220 spectra computed at different time steps ranging from 0.01 Myr to 14 Gyr, with a metallicity ranging from -1.7 dex to 0.4 dex (more details in Plat et al. 2019; Sánchez et al. 2022). The templates in our library have been built assuming different SFHs, chemical enrichment histories, and dust attenuation values (following the two components attenuation model of Charlot & Fall 2000), covering extensively the space of observables. The SFHs are composed of a secular component, described by a Sandage (1986) law:

$$\mathrm{SFR}_{\tau}(t) \propto \frac{t}{\tau} \exp\left(-\frac{t^2}{2\tau^2}\right), \tag{2.1}$$

with a superposition of random bursts (in two-thirds of the templates). The total mass formed in these bursts ranges between 1/1000 and two times the total stellar mass formed in the secular component. The resulting templates library roughly uniformly covers the

[1]The models used in Costantin et al. (2019) were a CB16 version, while the models adopted in this work are the official 2019 public release (*http://www.bruzual.org/CB19/*), referred as C&B in Sánchez et al. 2022 (private communication by G. Bruzual).

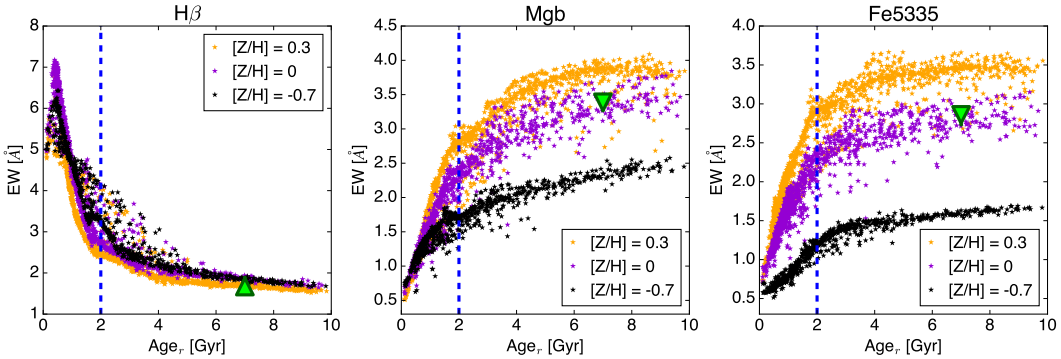

Figure 2.1: Distribution of Hβ (left panel), Mgb (middle panel) and Fe5335 (right panel) values as a function of the r-band light-weighted age in three different bins of mass-weighted [Z/H]: 0.3 (orange symbols), 0 (purple symbols), and -0.7 (black symbols), respectively, as measured in our template library (excluding templates with secondary bursts). The green arrow represents the effect on the indices of a 0.1% fraction of a young (70 Myr) stellar population superimposed on a population with 7 Gyr, both with a solar metallicity.

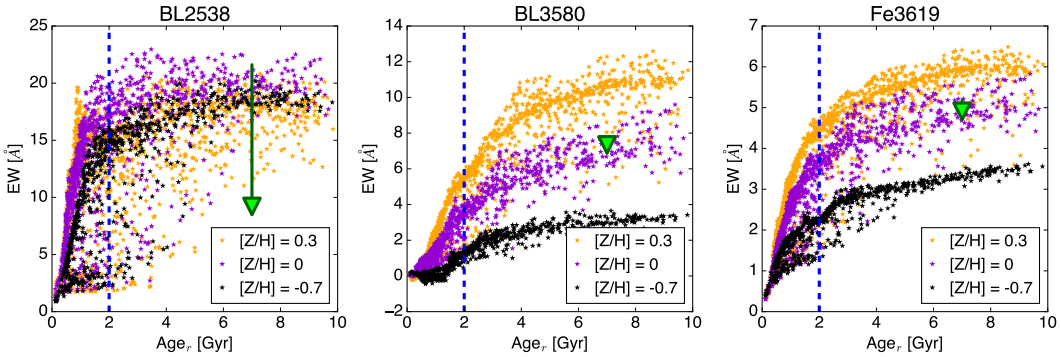

Figure 2.2: Same as Figure 2.1, but for BL2538 (left panel), BL3580 (middle panel), and Fe3619 (right panel), respectively.

mean mass-weighted log age-Z plane, between $-1.70 < [Z/H] < 0.4$ in the metallicity range, where solar metallicity is $[Z/H]_{sol} = 0$, and $8.5 < \log(\text{age yr}^{-1}) < 10.2$ in the age range. All the galaxy types are well represented, from the star forming galaxies to the quiescent ones, with the only exception of the starburst galaxies at their very early stage (i.e. characterised by high star formation rate and very small mass formed). More details about these templates can be found in Zibetti et al. (2017) and Costantin et al. (2019). We used a representative subset of the above library to generate mock WEAVE-StePS-like spectroscopic observations, while the remaining ones have been used as a comparison library to recover the input physical parameters using the Bayesian statistical tools described in Chap. 2.4 (see also Gallazzi et al. 2005).

2.2 Optical and UV spectral indices: A direct comparison

In the literature, stellar metallicity is usually determined by measuring the equivalent width of optical absorption line-strengths with respect to pseudo-continua, as defined in Worthey et al. (1994). In particular, specific optical spectral indices such as Mgb and

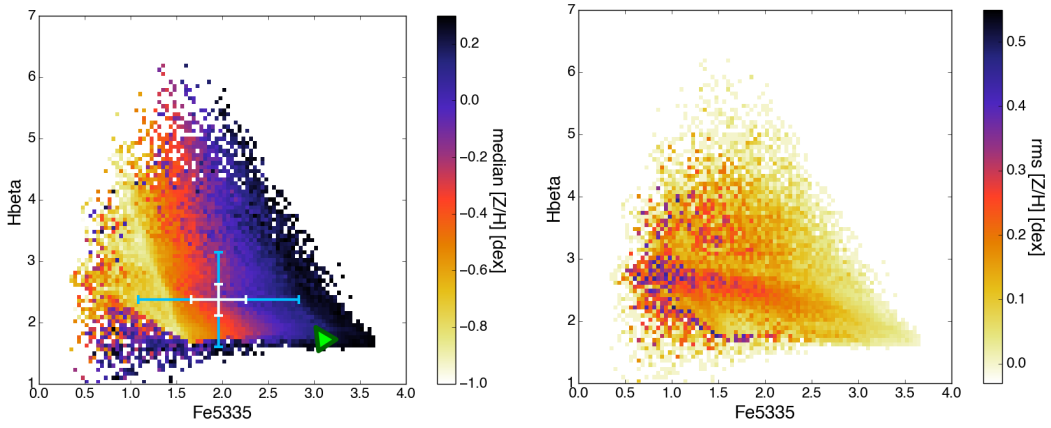

(a) (b)

Figure 2.3: (Fe5335,Hβ) diagnostic plane. Left panel: (Fe5335,Hβ) diagnostics colour-coded according to metallicity for the templates library, considering galaxies with r-band light-weighted age > 2 Gyr. Right panel: (Fe5335,Hβ) diagnostics colour-coded according to the rms in metallicity. The light blue and white error bars represent the typical median 1σ error in measuring Fe5335 and Hβ at $\mathrm{S/N}_{I,\mathrm{obs}} = 10$ and $\mathrm{S/N}_{I,\mathrm{obs}} = 30$, respectively. The green arrow represents the effect on the indices of a 0.1% fraction of a stellar population with 70 Myr superimposed on a population with 7 Gyr, each with solar metallicity.

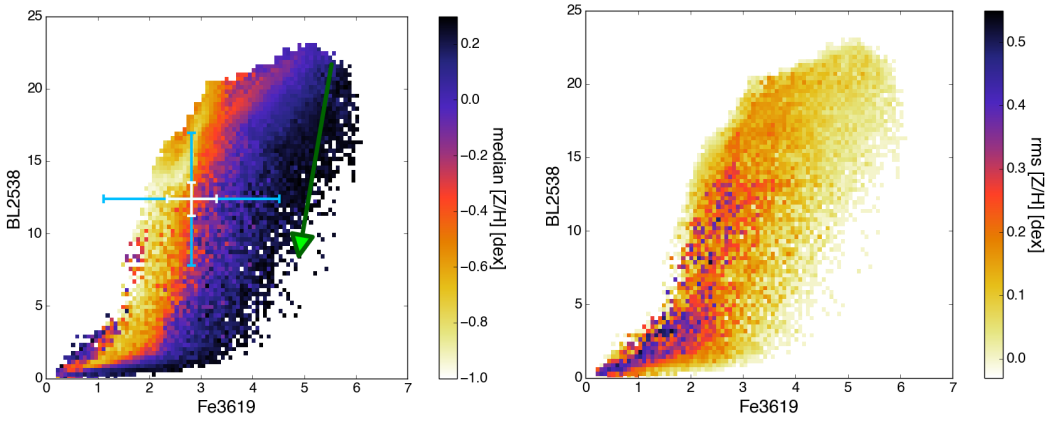

(a) (b)

Figure 2.4: Same as Figure 2.3, but for (Fe3619,BL2538).

Fe5335, combined with age-sensitive indices (e.g. Hβ), help to break the age-metallicity degeneracy (e.g. Boardman et al. 2017; Sarzi et al. 2018). Figure 2.1 shows the distribution of Hβ, Mgb, and Fe5335 values as a function of the r-band light-weighted age for three narrow bins of mass-weighted metallicities, [Z/H], measured in our templates library, but excluding cases with secondary bursts. As expected, Hβ values show a strong dependence on the r-band light-weighted age of the galaxy stellar populations, while Mgb and Fe5335 reveal a clear metallicity dependence, in addition to the age dependency. In particular the two metallicity-sensitive indices display similar behaviour, with a strong stellar metallicity dependence for ages older than 2 Gyr, whereas the age dependency nearly disappears. Typically, metallicity indices start to be mainly sensitive to the presence of hot stars for ages younger than 2 Gyr, implying a dependence on stellar age in that regime. This is particularly true for Mgb, whose absorption is prominent in the atmosphere of giant stars.

In recent decades, UV spectral indices, also sensitive to the stellar age and metallicity, have been used to infer stellar population properties in galaxies (e.g. Fanelli et al. 1992; Daddi et al. 2005; Maraston et al. 2009; Vazdekis et al. 2016; Lonoce et al. 2020; Salvador-Rusiñol et al. 2021). Figure 2.2 shows, as an example, the dependence of three UV indices, namely, the age-sensitive index BL2538 and the metallicity-sensitive indices BL3580 and Fe3619, on r-band light-weighted age. As for Mgb and Fe5335, the indices BL3580 and Fe3619 show a prominent dependence on [Z/H] for ages older than 2 Gyr, while the BL2538 index depends on both age and metallicity. For a more complete understanding of the behaviour of the UV indices (and continuum), particularly below 3000Å, as function of age and metallicity, it should be noted that they can be strongly affected by the presence of even a tiny fraction (i.e. $< 0.1\%$ of the overall mass) of very young (i.e. age < 100 Myr) and hot stars, with drastic changes seen in the continuum and spectral features (Cassarà et al. 2013; Vazdekis et al. 2016; Salvador-Rusiñol et al. 2020, 2021; Corcho-Caballero et al. 2021; Salvador-Rusiñol et al. 2022). In our simulations cases of quiescent galaxies with a tiny fraction of a very young populations are rare; however, they seem quite common, at least in the Local Universe, therefore we explored the behaviour of UV and optical indices considering a combination of two SSPs model. In Figures 2.1 and 2.2, the green arrows indicate the effect of adding 0.1% of mass fraction of a 70 Myr SSP to an old SSP of 7 Gyr, both at solar metallicity. As we can see from Figs. 2.1 and 2.2, even a tiny fraction of a very young population has an important effect in the spectral region below 3000Å. Strong effect on the UV wavelength region of rather old stellar populations can be produced also by old hot stars such as the post-asymptotic giant branch (PAGB) (e.g. Le Cras et al. 2016), whose treatment in stellar population models is rather uncertain (e.g. due to the effect of mass-loss on advanced phases of stellar evolution; see Maraston et al. 2006; Conroy 2013), or those on the blue horizontal branch (not included in our templates). On the contrary, the effect is drastically reduced for indices in the wavelength region around 3500Å, and becomes even more negligible when moving to optical indices.

Classically, index-index diagnostics, which combine an age and a metallicity index indicator, are used to infer the metallicity (and the age) of stellar populations to reduce the age-metallicity degeneracy (e.g. Trager et al. 2000; Longhetti et al. 2000). The (Fe5335, Hβ) or (Mgb, Hβ) diagnostic diagrams have been often used to constrain the metallicity from low-to high-redshift galaxies (see Cervantes & Vazdekis 2009, and references therein). Figure 2.3 shows the (Fe5335, Hβ) diagnostic plane colour-coded according to the median mass-weighted metallicity (left panel) and to the intrinsic scatter of the metallicity (right panel) for the library previously described, including secondary bursts but considering galaxies with r-band light-weighted age > 2 Gyr. The different metallicity values occupy different regions of the index-index plane, with some mixing of values restricted only in the

lower left corner (i.e. low values of both Hβ and Fe5335 indices) corresponding to complex templates with a burst added over the secular SFH component. This is clearly shown in the right panel of Fig. 2.3, where the average low scatter in metallicity at each bin of the index-index diagram confirms that we can effectively disentangle age and metallicity using this diagnostic plane.

Figure 2.4 shows, for the same set of galaxies, an index-index plane and its scatter based on the UV indices Fe3619 and BL2538. We can see that the metallicity values follow a roughly linear trend, where metallicity increases with increasing Fe3619, irrespective of the complexity of the SFHs. The small intrinsic scatter confirms the good quality of the diagnostic plane, showing a similar degeneracy as the (Fe5335,Hβ) one. Following the green arrows in Figs. 2.3 and 2.4, again the effect is clear of a tiny fraction of a very young SSP over a 7 Gyr one on the UV age-sensitive index BL2538, while the other index is barely affected.

However, given the nonzero observational errors (see white and green error bars in Fig. 2.3 and 2.4) the uncertainties on inferring stellar metallicity using only two indices are not negligible. A better approach is to use the whole range of available spectral indices to optimally constrain the metallicity of stellar populations in galaxies, as we explore in the following sections.

2.3 WEAVE-StePS-like observations

In this section, we explore the advantages offered by a wide spectral range provided by new-generation spectrographs, such as WEAVE and 4MOST. Since both spectrographs have similar performances in terms of resolution and wavelength coverage, we followed the same approach as in Costantin et al. (2019) by simulating observations of a large sample of galaxies as will be carried out in the WEAVE-StePS survey. From the library described in Chapter 2.1, we selected a statistically significant and representative chunk of 25000 templates to produce mock WEAVE-StePS-like observations, while the remaining templates are used as comparison library. The selected chunk of templates adopted to reproduce mock observations contains twice the number that was used in Costantin et al. (2019) in order to have a better populated sample of old galaxies at different metallicities. Simulated spectra that realistically resemble the observations were obtained considering the throughput of the combined atmospheric transmission of the WHT and of the WEAVE spectrograph. The contributions to the noise are due to the extended Poisson noise from the sky background and to the read-out noise of the WEAVE CCDs. In this way, our simulations aptly reproduce a realistic S/N distribution as a function of wavelength for a variety of galaxy spectral types (including red galaxies), accounting for the reduced efficiency of the WEAVE+WHT system going to bluer wavelengths. The possible systematic effects present in real observed data (e.g. sky subtraction residuals, flux calibration errors) are not included, as their study is beyond the scope of the present paper. For details on the procedure to transform the rest-frame subsample to mock WEAVE-StePS-like observations, we refer to Sect. 3 in Costantin et al. (2019).

We considered three reference redshifts $z = [0.30, 0.55, 0.70]$ to reproduce the galaxies targeted by WEAVE-StePS and four bins of $S/N_{I,\mathrm{obs}} = [10, 20, 30, 50]\text{Å}^{-1}$. The $S/N_{I,\mathrm{obs}} = 50\text{Å}^{-1}$ bin has been added to the set adopted in Costantin et al. (2019) because, while not representing the expected WEAVE-StePS observations, it can provide more general useful insights on the possibility to estimate the stellar metallicity with higher S/N surveys, as it will be in 4MOST-StePS, or using a stacking procedure to increase the quality of observations at relatively low S/N. For each redshift, observations have been created

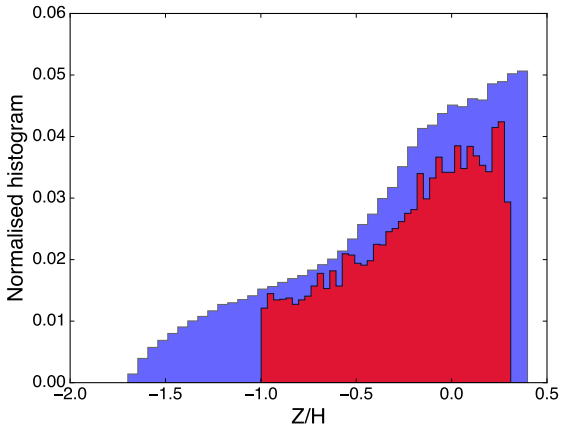

Figure 2.5: Distribution in metallicity of the mock WEAVE-StePS-like observations (red histogram) and the comparison library (blue histogram) at $z = 0.30$.

selecting from the set of 25000 templates those corresponding to $t_{\rm form} < {\rm Age}_{\rm Universe} - 1$ Gyr at that redshift, where $t_{\rm form}$ is the lookback time at the observation, g-band effective attenuation $A_g < 2$ mag, and mass-weighted metallicity $-1 <$ [Z/H] < 0.3. Figure 2.5 shows the distribution in metallicity of the mock WEAVE-StePS-like observations (red histogram) and the comparison library (blue histogram) at $z = 0.30$. Metallicities below -1 dex are extremely rare, in particular for massive galaxies as the targets of WEAVE-StePS survey. In fact, massive galaxies tend to have high metallicity values (e.g. Gallazzi et al. 2005; Thomas et al. 2010; Gallazzi et al. 2021). The final simulated sample consists of 9635 spectra at $z = 0.30$, 8498 at $z = 0.55$, and 7884 at $z = 0.70$, while the comparison library consists of more than 300000 templates, selected to have $t_{\rm form} < {\rm Age}_{\rm Universe}$. The selected subsamples are fully representative of the comparison library, without bias in physical properties, and large enough to explore the parameter space of the physical properties of the galaxies with robust statistics. Both the mock observations and the comparison library are convolved with a fixed velocity dispersion of 150 kms^{-1} in order to account for the typical velocity dispersion expected for WEAVE-StePS galaxies. The templates do not include emission lines, assuming that their contribution has been removed from the spectra.

2.4 Analysis

The main goal of our analysis is to exploit the information provided by key UV and optical absorption-line indices coupled with a Bayesian approach in order to infer the stellar metallicity of galaxies. The analysis is performed on the spectral data for each redshift and $S/N_{I,\rm obs}$, as described in Chapter 2.3.

2.4.1 Spectral indices

We considered a set of spectral indices to be used in our analysis, as listed in Table 2.1. The indices we selected present some differences with respect to those reported in Costantin et al. (2019). In fact, 12 indices among the optical and UV ones have been removed, while 3 UV indices (BL2720, BL2740, BL3619) have been added. Removed indices have been discarded because, even if they appear to be good metallicity or age indicators, they are strongly dependent on other unknown parameters (e.g. specific elements abundances

or IMF) or they can be strongly affected by observational issues (e.g. accuracy of the relative flux calibration). In particular, we excluded indices strongly sensitive to C, N, and Ti abundances (NH3360, CN3883, CN4170, Fe4668, Ca4227, and Fe5782), because they could alter the final results, due to their strong dependence on abundance ratios. We also excluded indices potentially affected by chromospheric emission from the stellar atmospheres (MgII, CaHK) and those possibly affected by interstellar absorption (NaD). TiO1 and TiO2 have been excluded as they are very broad indices, possibly affected by uncertainty on flux calibration. Moreover, both TiO's are strongly dependent on the assumed IMF (e.g. Spiniello et al. 2014). Finally, we excluded the Mgwide because it is a very wide index that needs a reliable flux calibration of the observed data in the UV part of the spectral range, which is not easy to achieve in many spectroscopic surveys[2]. In Table 2.1 we also show the variation of the UV indices when adding 0.1% of the total mass of very young SSP to an otherwise old SSP (see Chap. 2.2), normalised to the range of values covered by each index in the whole spectral library, namely, the relative sensitivity of each index to the presence of young populations. It is appreciable how the effect due to the presence of a tiny fraction of a very young population decreases as the wavelength increases, from 70% of variation for the bluest UV index to 10% for the reddest one.

We measured all the spectral indices that fall in the WEAVE observed spectral range at each selected redshift, and we estimated the observational errors for each index by generating 1000 random gaussian distributed realisations within the noise of each single spectrum at any $S/N_{I,\mathrm{obs}}$. For each realisation, we calculated the systematic and statistical errors as the median and the standard deviation of the relative difference between true and simulated values, respectively. Moreover, we added an extra error of $\sim 5\%$ to the $\mathrm{D_n}4000$ to take into account the possible uncertainty of the spectrophotometric calibration that do not explicitly enter into our simulations, as in Costantin et al. (2019). This extra error budget of 5% has been estimated given the expected relative flux calibration errors for the future WEAVE-StePS survey within spectra windows of 200Å.

2.4.2 Bayesian inference

The Bayesian approach provides a powerful framework for deriving the age and metallicity of stellar populations in galaxies. Our application of the Bayesian statistics consists on the comparison between a set of indices measured in the WEAVE-StePS-like simulations and those measured in the comparison library, as introduced by Gallazzi et al. (2005) and also described in Costantin et al. (2019). We computed the posterior probability of the age and metallicity parameters, where the likelihood is described by $\mathcal{L} = e^{-\chi^2/2}$, with

$$\chi^2 = \sum_i \left(\frac{I_{obs_i} - I_{mod_i}}{\sigma_{obs_i}} \right)^2, \tag{2.2}$$

where I_{obs_i} and I_{mod_i} are the i-th spectral index measured in the simulated and in the comparison spectra, respectively, and σ_{obs_i} is the observational error of the i-th spectral simulated index. The observational error has been evaluated as the standard deviation of the distribution of 1000 random gaussian realisations of the perturbed spectrum, as described in Chapter 2.4.1. With a Bayesian analysis we are able to retrieve for each observation the full probability density function (PDF) of any physical parameter, and we assume its median value as the expected value and the $16-84\%$ percentile range as the uncertainty of the estimated parameters. The PDF of a physical parameter for each

[2]We checked that adding the Mgwide in the inference of metallicity does not significantly change our main results, therefore we decided not to include this index in the main analysis.

Table 2.1: UV and optical spectral indices.

UV index (1)	% (1a)	z (2)	ref. (3)	opt. index (1)	z (2)	ref. (3)
FeII2402	70	> 0.66	a	D_n4000	all	d
BL2538	60	> 0.56	a	$H\delta_F$	all	e
FeII2609	47	> 0.48	a	$H\gamma_F$	all	e
BL2720	37	> 0.43	b	$G_{band}4300$	all	e
BL2740	44	> 0.43	b	Fe4383	all	e
Mg2852	37	> 0.35	a	Ca4455	all	e
Fe3000	23	> 0.31	a	Fe4531	all	e
BL3096	23	> 0.25	a	$H\beta$	all	e
BL3580	11	> 0.09	a	Fe5015	all	e
Fe3619	10	> 0.06	c	Mgb	all	e
				Fe5270	< 0.79	e
				Fe5335	< 0.77	e
				Fe5406	< 0.75	e
				Fe5709	< 0.66	e

(1) index name; (1a) variation of the UV index due to a 0.1% young population on top of 99.9% of 7 Gyr population; (2) redshift range in which the index is within the spectral range of the WEAVE spectrograph ($z_{max} = 0.8$); (3) reference for indices definition: (a) Fanelli et al. (1992), (b) Chavez et al. (2007), (c) Gregg (1994), (d) Balogh et al. (1999) , (e) Worthey et al. (1994).

simulated spectrum is given by the distribution in that parameter of the $\mathcal{L}$ of all the templates in the comparison library.

2.5 Age and metallicity estimates

As detailed in the previous paragraph, we measured all optical and UV indices listed in Table 2.1 for the simulated and the comparison spectra (17 indices at $z = 0.3$, 22 at $z = 0.55$ and 23 at $z = 0.7$). Then we compared the observed spectral indices with those obtained in the comparison library taking into account the expected observational errors to finally obtain metallicity measurements of our WEAVE-StePS-like observations by marginalising over the other parameters.

Figure 2.6 shows examples of metallicity PDFs of four simulated galaxies which differ for the mean r-band light-weighted ages of their stellar content ($Age_r = [0.5, 3, 5, 7]$ Gyr), and for the mass-weighted metallicity ([Z/H] $= [-0.25, -0.9, 0.5, 0.2]$ dex) and $S/N_{I,obs} = [10, 30, 50]$, respectively. It is noticeable that the uncertainty on the metallicity estimates decreases with increasing age, in particular at low $S/N_{I,obs}$. Moreover, $S/N_{I,obs}$ plays a crucial role in the uncertainty of the derived metallicity estimate, and differences in the PDF width between $S/N_{I,obs} = 10$ and $S/N_{I,obs} = 30$ are quite large. However, it clearly appears that from $S/N_{I,obs} = 30$ to $S/N_{I,obs} = 50$ the improvement in the uncertainty of the metallicity measurements is smaller, in particular for old ages.

Figure 2.7 shows examples of joint age and metallicity probability distributions for another four simulated galaxies with different values of age and metallicity at $z = 0.3$, where the contours with different colours (blue, red, and black) correspond to different $S/N_{I,obs} = [10, 30, 50]$, respectively. The age-metallicity degeneracy can be clearly seen for galaxy n.2 and 4, for which the corresponding probability distributions are elongated

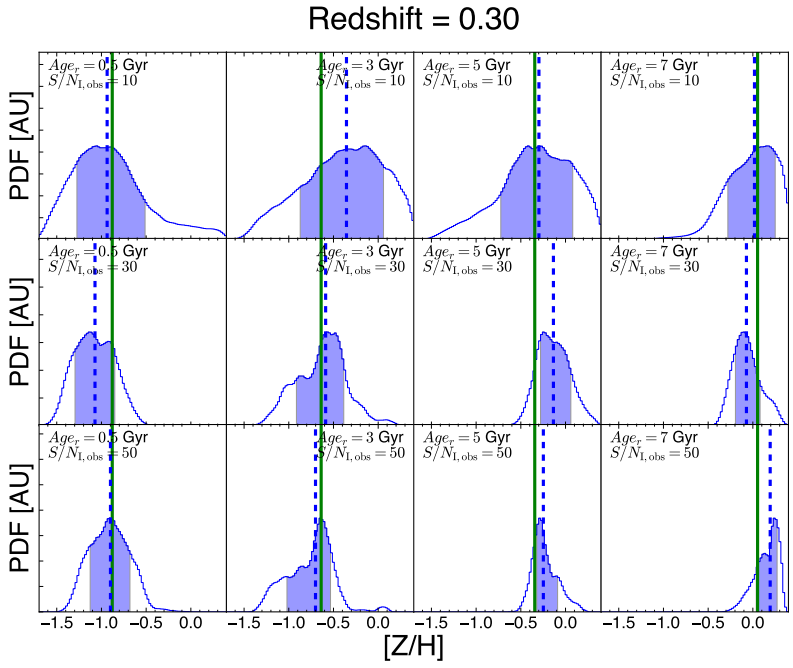

Figure 2.6: Examples of PDFs of mass-weighted metallicity of observations at $z = 0.3$ for $\mathrm{Age}_r = [0.5, 3, 5, 7]$ Gyr (from left to right) and $S/N_{I,\mathrm{obs}} = [10, 30, 50]$ (from top to bottom). The filled region represents the $16-84$ confidence interval of the PDF. The solid green line marks the true value of metallicity, while the dashed blue line represents the median value of the corresponding distribution.

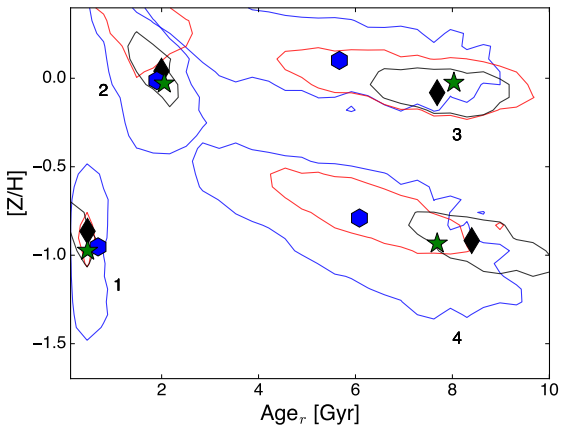

Figure 2.7: Examples of 68% confidence interval of joint r-band light-weighted age and mass-weighted metallicity distributions at $z = 0.3$ at $S/N_{I,\mathrm{obs}} = 10$ (blue lines), $S/N_{I,\mathrm{obs}} = 30$ (red lines), and $S/N_{I,\mathrm{obs}} = 50$ (black lines). The blue hexagons marks the median age-metallicity values of the distribution at $S/N_{I,\mathrm{obs}} = 10$, the black diamonds the median age-metallicity at $S/N_{I,\mathrm{obs}} = 50$, and the green stars represent the true age-metallicity values.

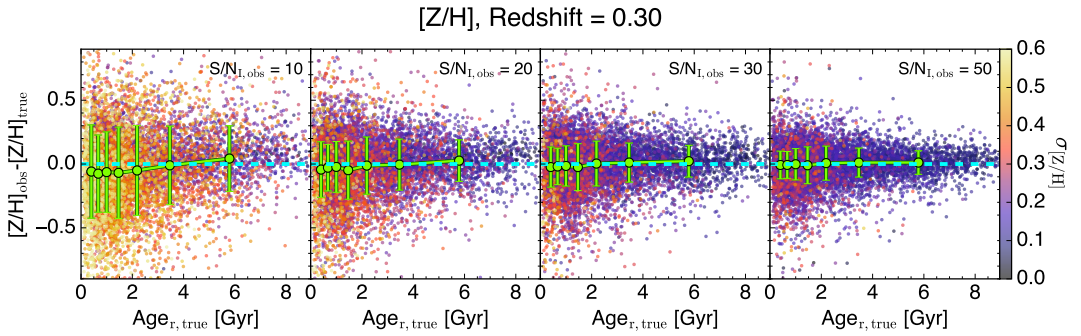

(a)

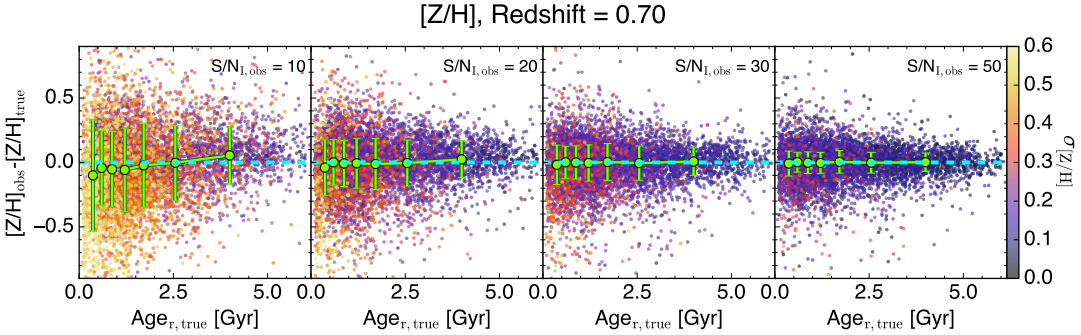

(b)

Figure 2.8: Difference between observed and true metallicity, as a function of true r-band light-weighted age values at different redshifts. *Top panel*: Difference between observed and true metallicity, as a function of true r-band light-weighted age values at $z = 0.30$. Each dot is colour-coded according to $\sigma_{[\mathrm{Z/H}]}$ obtained from the posterior. The green dots are the median values of the [Z/H] differences in bins of $\mathrm{Age}_{r,\mathrm{true}}$, while the error bars are the median of the $\sigma_{[\mathrm{Z/H}]}$, with each bin having the same number of data points. The cyan dashed line represents the 0 value of the y-axis. *Bottom panel*: Same as the top panel for $z = 0.70$.

diagonally in the diagram, in particular at $S/N_{I,\mathrm{obs}} = 10$. It can also be seen that the constraints on the metallicity estimates are tighter with increasing age. This is expected, as already noticed in Chap. 2.2, because for old stellar populations metallic lines become stronger and their variation becomes steeper and independent of age, giving better constraints. Instead, age indicators (e.g. Balmer lines) become weaker and their variation flatter for older populations. On the contrary, metallicity indicators (both optical and UV) become weaker for hot stars, and change very little with metallicity at ages lower than 2 Gyr, becoming mainly sensitive to the age.

Figure 2.8 shows the difference between the observed metallicity and the true one as a function of the r-band light-weighted age for the simulations at $z = [0.3, 0.7]$ and $S/N_{I,\mathrm{obs}} = [10, 20, 30, 50]$. Figure 2.9 shows the same difference but as a function of the true metallicity values. Points are colour-coded according to the metallicity errors obtained from the PDF. Table 2.2 summarises our capability to retrieve the mass-weighted metallicity (as presented in Fig. 2.8) by showing the 1σ errors for seven age bins with equal number of data points, at all the simulated redshift and $S/N_{I,\mathrm{obs}}$, while Table 2.3 shows the same 1σ errors for seven metallicity bins. In this table, we also added the errors estimated at $S/N_{I,\mathrm{obs}} = 10$ for simulated galaxies with r-band light-weighted age > 2

Table 2.2: Error estimates of all the simulated galaxies reported in seven r-band light weighted age bins at all the redshift and $S/N_{I,\mathrm{obs}}$. The total number of available galaxies has been divided in seven bins equally populated. Each bin has different width, assuming the median value as reference. The errors are the 68% confidence interval of the PDF of mass-weighted stellar metallicity, and are expressed in dex.

				$z = 0.30$				
Age_{bin} [Gyr]	[0.07, 0.5]	[0.5, 0.8]	[0.8, 1.1]	[1.1, 1.7]	[1.7, 2.7]	[2.7, 4.4]	[4.4, 9]
$S/N_{I,\mathrm{obs}} = 10$	0.37	0.30	0.32	0.36	0.35	0.30	0.26
$S/N_{I,\mathrm{obs}} = 20$	0.22	0.18	0.20	0.23	0.22	0.20	0.16
$S/N_{I,\mathrm{obs}} = 30$	0.16	0.14	0.16	0.18	0.18	0.15	0.12
$S/N_{I,\mathrm{obs}} = 50$	0.11	0.11	0.12	0.14	0.13	0.11	0.09
				$z = 0.55$				
Age_{bin} [Gyr]	[0.07, 0.5]	[0.5, 0.7]	[0.7, 1]	[1, 1.4]	[1.4, 2.2]	[2.2, 3.5]	[3.5, 6.8]
$S/N_{I,\mathrm{obs}} = 10$	0.39	0.29	0.30	0.34	0.33	0.29	0.23
$S/N_{I,\mathrm{obs}} = 20$	0.22	0.18	0.18	0.21	0.21	0.19	0.15
$S/N_{I,\mathrm{obs}} = 30$	0.16	0.13	0.15	0.17	0.17	0.15	0.12
$S/N_{I,\mathrm{obs}} = 50$	0.10	0.09	0.11	0.12	0.11	0.10	0.08
				$z = 0.70$				
Age_{bin} [Gyr]	[0.07, 0.5]	[0.5, 0.7]	[0.7, 0.9]	[0.9, 1.3]	[1.3, 2]	[2, 3.1]	[3.1, 6.1]
$S/N_{I,\mathrm{obs}} = 10$	0.43	0.29	0.29	0.32	0.33	0.29	0.22
$S/N_{I,\mathrm{obs}} = 20$	0.22	0.18	0.18	0.19	0.20	0.18	0.14
$S/N_{I,\mathrm{obs}} = 30$	0.15	0.12	0.14	0.14	0.14	0.13	0.11
$S/N_{I,\mathrm{obs}} = 50$	0.10	0.08	0.08	0.08	0.09	0.09	0.07

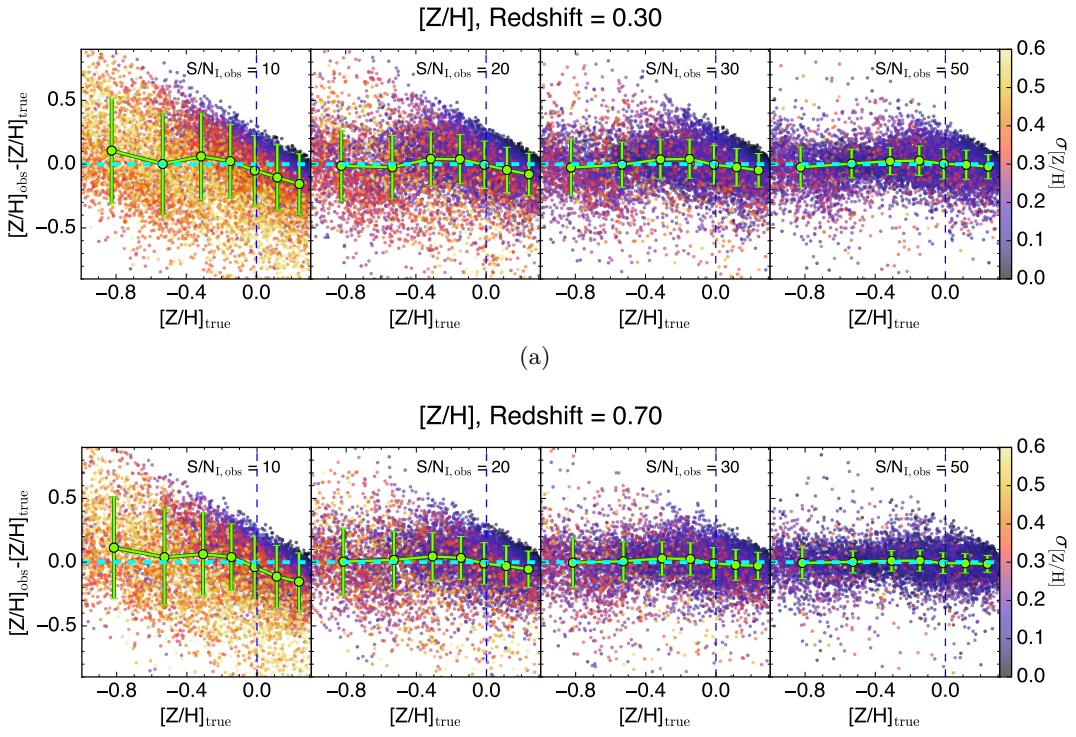

Figure 2.9: Difference between observed and true metallicity as a function of the true values of metallicity at different redshifts. *Top panel*: Difference between observed and true metallicity as a function of the true values of metallicity at $z = 0.30$. Each dot is colour-coded according to $\sigma_{[Z/H]}$ obtained from the PDF. The green dots are the median values of the [Z/H] differences in bins of $\mathrm{Age}_{r,\mathrm{true}}$, while the error bars are the median of the $\sigma_{[Z/H]}$, with each bin having the same number of data points. The cyan dashed line represents the 0 value of the y-axis. *Bottom panel*: Same as the top panel for $z = 0.70$.

Gyr, showing that for older populations, we obtain lower uncertainties on metallicity. It is worth noticing that the typical uncertainties of metallicity estimates well match the median dispersion around the true values.

The main result from Fig. 2.8 is that the median differences between the measured and the true metallicities as a function of the r-band light-weighted age are consistent with 0 for all the cases explored. This indicates that, on average, metallicity can be inferred with no systematic deviations at any galaxy age for all the $S/N_{I,\mathrm{obs}}$. On the other hand, the typical median errors decrease with increasing r-band age for all the $S/N_{I,\mathrm{obs}}$, with values, at $S/N_{I,\mathrm{obs}} = 10$, from $\sigma = 0.38$ dex for $\mathrm{age}_{\mathrm{bin}} = [0.07, 0.5]$ Gyr to $\sigma = 0.26$ dex for $\mathrm{age}_{\mathrm{bin}} = [4.4, 9]$ Gyr, improving ~ 0.1 dex at older ages. A similar effect is obtained by increasing the $S/N_{I,\mathrm{obs}}$ from 10 to 20, reducing the uncertainties for older galaxies down to less than 0.2 dex. The lower panels of Figure 2.8 show the results for simulations at $z = 0.70$. As the number and the typical errors of available indices falling into the WEAVE wavelength range varies with the redshift considered, the upper and lower panels of Figure 2.8 differ. Errors in the metallicity estimate at $z = 0.7$ for galaxies older than 1 Gyr are slightly lower than those obtained at $z = 0.3$, up to 0.04 dex around 5 Gyr. This is mainly due to the higher number of UV indices available at higher redshift.

The expected precision in the metallicity estimate as a function of the true metallicity values is shown in Fig. 2.9, both at low (upper panel) and at high (lower panel) redshift.

Table 2.3: Same as Table 2.2 with simulated galaxies reported in seven metallicity bins. The values in parenthesis represent the error estimates at $S/N_{I,\mathrm{obs}} = 10$ for simulated galaxies with r-band light-weighted age > 2 Gyr.

$z = 0.30$							
$[\mathrm{Z/H}]_{bin}$ [dex]	$[-1, -0.67]$	$[-0.67, -0.42]$	$[-0.42, -0.22]$	$[-0.22, -0.06]$	$[-0.06, 0.09]$	$[0.09, 0.21]$	$[0.21, 0.31]$
$S/N_{I,\mathrm{obs}} = 10$	0.42 (0.39)	0.39 (0.39)	0.33 (0.33)	0.28 (0.28)	0.26 (0.25)	0.25 (0.21)	0.23 (0.19)
$S/N_{I,\mathrm{obs}} = 20$	0.28	0.24	0.20	0.18	0.18	0.17	0.16
$S/N_{I,\mathrm{obs}} = 30$	0.22	0.17	0.15	0.15	0.14	0.14	0.12
$S/N_{I,\mathrm{obs}} = 50$	0.16	0.10	0.10	0.11	0.11	0.11	0.09
$z = 0.55$							
$[\mathrm{Z/H}]_{bin}$ [dex]	$[-1, -0.67]$	$[-0.67, -0.42]$	$[-0.42, -0.22]$	$[-0.22, -0.06]$	$[-0.06, 0.09]$	$[0.09, 0.21]$	$[0.21, 0.31]$
$S/N_{I,\mathrm{obs}} = 10$	0.40 (0.36)	0.37 (0.36)	0.31 (0.31)	0.26 (0.26)	0.25 (0.22)	0.24 (0.19)	0.22 (0.17)
$S/N_{I,\mathrm{obs}} = 20$	0.26	0.22	0.19	0.17	0.17	0.16	0.15
$S/N_{I,\mathrm{obs}} = 30$	0.21	0.16	0.14	0.14	0.13	0.13	0.12
$S/N_{I,\mathrm{obs}} = 50$	0.14	0.09	0.09	0.09	0.09	0.09	0.08
$z = 0.70$							
$[\mathrm{Z/H}]_{bin}$ [dex]	$[-1, -0.67]$	$[-0.67, -0.42]$	$[-0.42, -0.22]$	$[-0.22, -0.06]$	$[-0.06, 0.09]$	$[0.09, 0.21]$	$[0.21, 0.31]$
$S/N_{I,\mathrm{obs}} = 10$	0.41 (0.36)	0.37 (0.34)	0.31 (0.29)	0.25 (0.25)	0.24 (0.22)	0.24 (0.18)	0.22 (0.16)
$S/N_{I,\mathrm{obs}} = 20$	0.27	0.22	0.18	0.16	0.15	0.15	0.13
$S/N_{I,\mathrm{obs}} = 30$	0.19	0.15	0.13	0.12	0.12	0.11	0.10
$S/N_{I,\mathrm{obs}} = 50$	0.12	0.08	0.08	0.08	0.08	0.07	0.06

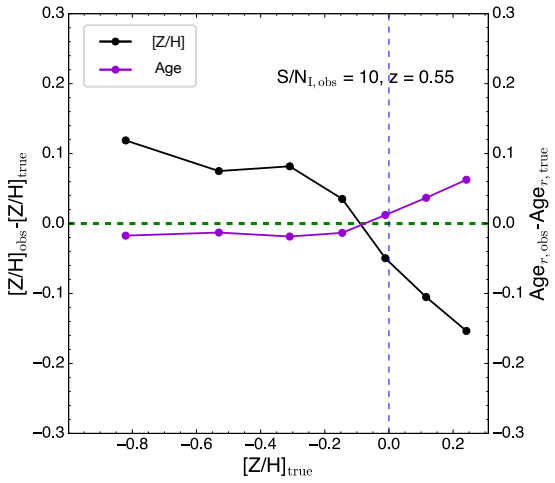

Figure 2.10: Median values of the difference between observed and true values of mass-weighted metallicity (black points and lines) and r-band light-weighted age (violet point and lines), as a function of true metallicity at $z = 0.55$ and $S/N_{I,\mathrm{obs}} = 10$. The blue vertical dashed line marks the solar metallicity value ([Z/H] = 0). The green dashed line represents the 0 value of the y-axis.

At $S/N_{I,\mathrm{obs}} = 10$, the uncertainties decrease from $\sigma = 0.37$ dex for very low metallicity (i.e. [Z/H] ≤ -0.8) to $\sigma = 0.22$ dex for super-solar metallicities. Concerning the expected accuracy, at the lowest/highest metallicities, there is a overestimation or underestimation of ~ 0.1 dex. To better appreciate this trend, Figure 2.10 shows the median values in seven metallicity bins of the difference between the observed and true values of mass-weighted metallicity compared to the difference for r-band light-weighted age as a function of the true values of metallicity at $z = 0.55$ and $S/N_{I,\mathrm{obs}} = 10$. When metallicity is underestimated, age is overestimated – and the other way around as well, consistently with the well-known age-metallicity degeneracy. Moreover the offset at the highest metallicity likely reflects the lack of templates above [Z/H] ~ 0.3 (the maximum value in the input library), making the lowest [Z/H] the most preferable in the index analysis (see Chap. 2.4.1). In other words, at the highest as well as the lowest metallicity, our metallicity estimates, for $S/N_{I,\mathrm{obs}} = 10$, are affected by the prior distribution. Nevertheless, the systematic offset is well within the errors (~ 0.3 dex at $S/N_{I,\mathrm{obs}} = 10$), and it drastically decreases already at $S/N_{I,\mathrm{obs}} = 20$.

The results displayed in Figs. 2.8, 2.9, and 2.10 are based on all the available indices listed in Table 2.1 depending on the simulated redshift. However, as already noted in Chap. 2.2, UV indices located at restframe wavelength lower than 3000Å are strongly affected by the presence of even a tiny fraction of hot stars (e.g. very young or PAGB/HB stars). Since both the origin and the effect of these populations are still poorly understood and hard to model (see e.g. Le Cras et al. 2016; Salvador-Rusiñol et al. 2020, 2021, 2022), and an extensive treatment of these components is beyond the scope of the present paper, we also repeated our analysis by excluding UV indices at $\lambda < 3000$Å (i.e. the ones potentially affected by these components, see Table 2.1). Figure 2.11 shows the comparison between the main analysis of this work and the same analysis performed excluding UV indices below 3000Å. We found very similar uncertainties in both cases, thus, our ability to constrain metallicity is the same when excluding UV indices below 3000Å. We also verified that the age limit within the comparison library, selected to be lower than the age of the

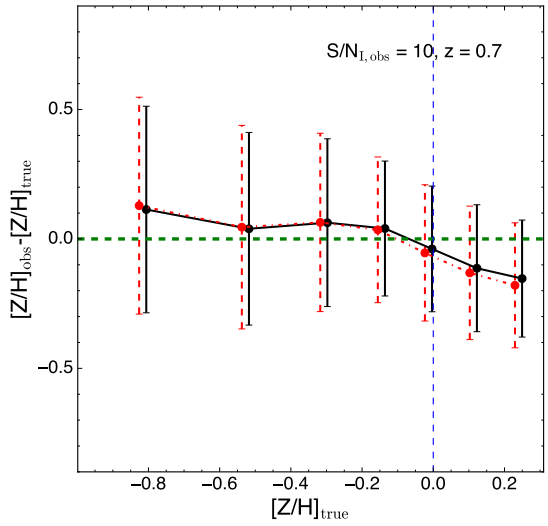

Figure 2.11: Median values of the difference between observed and true metallicity as a function of the true values of metallicity at $z = 0.70$ and $S/N_{I,\mathrm{obs}} = 10$. The black error bars indicates the main case of our work, while the red dashed error bars represent the case excluding indices below 3000Å. The blue vertical dashed line marks the solar metallicity value ([Z/H] = 0). The green dashed line represents the 0 value of the y-axis.

universe at each redshift, does not affect the results, which are consistently derived even using the entire available range of ages. We checked the effect on the results of simulating galaxies based on α-enhanced stellar populations (which is particularly relevant for massive galaxies) keeping the comparison template library based on solar chemical composition (see Appendix A.1 for details). Although we found that the effect of [α/Fe] = 0.4 dex can introduce systematic offsets in metallicity estimates up to −0.3 dex at $S/N = 10$, our test is an extreme case, since usually massive quiescent galaxies have [α/Fe] up to 0.3 dex (e.g. Thomas et al. 2010; La Barbera et al. 2013; Carnall et al. 2022). Moreover, the effect of varying chemical abundances might be not so severe, as the overabundance of different elements affect spectral features in a different way. For instance, the relative response of an SSP model spectrum to increasing [α/Fe] tends to go into the opposite direction of increasing [C/Fe], so that for several spectral indices, increasing both elements (as it is the case in massive galaxies) affects only marginally the line-strengths (see La Barbera et al. 2017). In future works, we will take this issue into account by using models with varying [α/Fe] and other elemental abundances.

We compared the accuracy of our metallicity estimates for simulated WEAVE-StePS-like spectra with those reported in the literature. Using SDSS spectra, Gallazzi et al. (2005) inferred metallicity of early-type and late-type galaxies in the Local Universe using five absorption indices, of which three are composites (D_n4000, $H\delta_A$+$H\gamma_A$, $H\beta$, [Mg_2Fe], [MgFe]'). To test the advantage of using a large number of indices, we performed our analysis considering only the five indices adopted by Gallazzi et al. (2005) and compare the results with our more general simulations including all the available indices at redshift $z = 0.3$. Both analyses are based on S/N derived from WEAVE-StePS-like simulations, and the results are presented in Fig. 2.12. Both the systematic offset between true and measured values, and the errors affecting the metallicity estimates are lower (up to 0.1 dex) when using all the available indices with respect to the restricted number of indices in Gallazzi et al. (2005).

Another instructive comparison can be made with the work of Choi et al. (2014), who

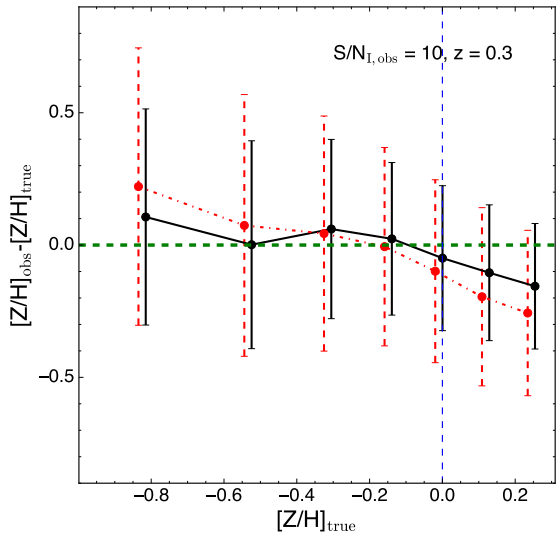

Figure 2.12: Median values of the difference between observed and true metallicity as a function of true metallicity values at $z = 0.30$ and $S/N_{I,\mathrm{obs}} = 10$. The black error bars show results for our analysis including all spectral indices, while the red dashed error bars represent the case using only the 5 absorption indices used in Gallazzi et al. (2005). The blue vertical dashed line marks the solar metallicity value ([Z/H] = 0). The green dashed line represents the 0 value of the y-axis.

inferred the metallicity by performing full spectral fittings in the $4700 - 5500$Å range on simulated spectra (see Fig. A.1 of Choi et al. 2014). They considered mock observations for a sample of quiescent galaxies at age $\sim$ 6 Gyr and solar metallicity, and obtained metallicity values without particular systematic offset and with error $\sigma_{\mathrm{Choi}} \sim 0.15$ dex. Considering a sample of galaxies from our simulations in the same age and metallicity range as in Choi et al. (2014), we found an error of 0.15 dex in [Z/H], perfectly matching the result obtained in Choi et al. (2014). This result is mainly due to the large set of indices used in our analysis.

López Fernández et al. (2016) performed a full spectral fitting analysis in the $3700 - 6800$Å range on simulated CALIFA (Calar Alto Legacy Integral Field Area, Sánchez et al. 2012) spectra to infer stellar metallicity. They considered mock observations with age and metallicity parameters similar to those of the sample used in the analysis of this work, and they obtained metallicity values without particular systematic offset from the true value and with error $\sigma_{\mathrm{Lopez}} = [0.33, 0.22, 0.13]$ at S/N = [10, 20, 50]. Considering the metallicity constraints on our entire sample at $z = 0.30$, we found errors of $[0.32, 0.21, 0.11]$ at $S/N = [10, 20, 50]$, consistent to the results obtained in López Fernández et al. (2016). Spectral fitting is expected to provide lower error bars, as all the information in the galaxy spectrum is used. Nevertheless, spectral indices help to extract the cleanest information from a galaxy spectrum, through well-selected and characterised spectral features, and help to reduce the effect of other parameters on the estimates of the metallicity (e.g. presence of dust and possible uncertainties on flux calibration). Moreover, as it will be explained in Chap. 2.6, increasing the number of indices helps to decrease the errors in constraining the metallicity.

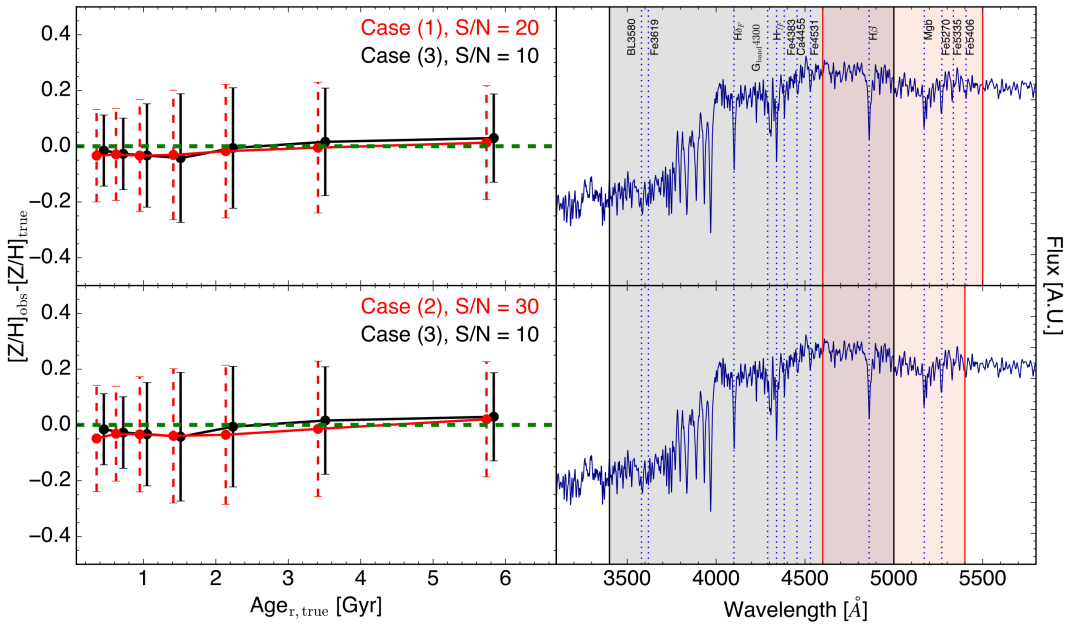

Figure 2.13: Median values of the difference between observed and true metallicity as a function of true r-band light-weighted age values. In both left panels, black error bars denotes case 3 ([BL3580, Fe3619, Hδ_F, Hγ_F, G$_{band}$4300, Fe4383, Ca4455, Fe4531, Hβ]) at S/N = 10, while the red dashed error bars indicates case 1 ([Hβ, Mgb, Fe5270, Fe5335, Fe5406]) at S/N = 20 (upper left panel) and case 2 ([Hβ, Mgb, Fe5270]) at S/N = 30 (lower left panel). The green dashed line in the left panels represents the 0 value of the y-axis. The blue curves in the right panels represent an example of a rest-frame template with 3 Gyr and solar metallicity. The black filled zone is the spectral range considered in case 3, while the red filled zone marks the spectral range considered in cases 1 and 2 (upper right and lower right panels, respectively).

2.6 Constraints from bluer indices

In this section, we present a more generic test to explore the difference in the capability of retrieving the stellar metallicity of galaxies when using a small set of indices at high S/N (≥ 20) or a larger one at a moderate S/N ($= 10$). In particular, we compared the results obtained using the classic set of optical indices ([$H\beta$, Mgb, Fe5270, Fe5335, Fe5406]) with those obtained using a larger set of indices between 3500 and 5000Å. This test is not specifically related to StePS-like spectra, and aims to inform other possible future spectroscopic surveys. For this reason, we did not use WEAVE-StePS-like simulated spectra (i.e. with S/N in the UV region depending on the spectral shape of the simulated galaxies for the same S/N fixed in the I-band region), but relied on a new set of ad hoc simulations, assigning a fixed S/N to the continuum adjacent to each spectral index considered. We selected three different set of indices: (1) [Hβ, Mgb, Fe5270, Fe5335, Fe5406], that is, the so-called "classic" indices, (2) [Hβ, Mgb, Fe5270] and (3) [BL3580, Fe3619, H$\delta_{\rm F}$, H$\gamma_{\rm F}$, $G_{\rm band}$4300, Fe4383, Ca4455, Fe4531, and Hβ], the first two at wavelengths larger than 4800Å, while the last one at wavelengths lower than 5000Å. We want to test whether it is more profitable for the stellar metallicity estimates to invest in observing time to obtain S/N = 20-30 around the first two set of indices or to obtain a S/N = 10 around the larger and bluer set of indices. The upper panel of Figure 2.13 shows the comparison of the results obtained using the five "classic" redder indices (i.e. case 1) at S/N = 20 (red error bars) and the larger set of 9 bluer indices (case 3) at a lower S/N of 10 (black error bars). It is clear that doubling the number of indices at lower S/N at 3500Å $< \lambda <$ 5000Å gives similar results than using only the five classic indices at higher S/N (4600Å $< \lambda <$ 5600Å). Moreover, the use of bluer indices allows us to obtain a better metallicity constraint at younger ages (as demonstrated by the black error bars in Fig. 2.13) becoming smaller than the red ones at ages younger than 1 Gyr. The lower panel of Figure 2.13 shows the comparison of the results obtained using even a smaller set of three "classic" redder indices (case 2, 4600Å $< \lambda <$ 5400Å) at S/N = 30 (red error bars) and the full set of 9 bluer indices (case 3) at S/N = 10 (black error bars). As in the upper panel, we found that results similar to those obtained with few optical indices at a relative high S/N can be obtained with a wider set of bluer indices, over a larger wavelength baseline, for spectra at a lower S/N. In this second comparison, the improvement on the metallicity estimates is higher, in particular at young ages when using the larger and bluer set of indices at S/N = 10, namely, one-third of the S/N value considered for the redder indices only. This result is in agreement with what previously found by López Fernández et al. (2016). They obtained similar constraints of the stellar metallicity combining optical spectra with FUV and NUV photometric data at S/N = 10 than using only optical spectra at S/N =20.

Our results show that metallicity can still be reliably measured with optical and blue spectral indices even at relatively low S/N values. Indeed, this is relevant when also taking into consideration that bluer indices are less affected by the sky emissions at $\lambda >$ 6000Å up to $z \sim 1$, whereas above $z \sim 0.5$, the redder indices are significantly affected by strong sky emission lines and telluric absorptions. This results could be useful for wavelength range selection in planning future spectroscopic surveys.

While our analysis shows that blue indices have a significant constraining power to metallicity, we caution that generally, they are also sensitive to the effect of non-solar abundance ratios (see e.g. Vazdekis et al. 2015), and therefore it would be ideal to estimate metallicity with both optical and UV features if modelling based on different chemical composition is not available.

2.7 Summary and conclusions

In this work we investigate the capability to retrieve the mass-weighted metallicity in galaxies at different redshifts and S/N values, simultaneously exploiting the UV and optical rest-frame wavelength coverage. Our analysis is based on the classic index fitting approach using a wide stellar templates library derived from the latest version of the Bruzual & Charlot (2003) models. We showed that the mid-UV indices BL3580 and Fe3619 can provide reliable constraints on stellar metallicity, when used along with other optical indicators. At the same time, we emphasised that UV indices below 3000Å can be strongly affected by the presence of even a tiny fraction (i.e. $< 0.1\%$ of the overall mass) of very young (i.e. age < 100 Myr) stars. The same effect is expected from the presence of old hot stars (e.g. PAGB/BHB stars) which can mimic the same behaviour of very young ones (e.g. Salvador-Rusiñol et al. 2020, 2021, 2022). Nevertheless UV spectral indices can be used to infer the metallicity of the stellar populations in galaxies, in particular considering the spectral region around ~ 3500Å.

To analyse the expected constraining power of different sets of indices on real observations, we simulated spectra as will be observed by the upcoming WEAVE-StePS survey. This intermediate redshift survey will observe around 25000 galaxies at $0.3 < z < 0.7$ covering a wide spectral range. Therefore, we simulated 25000 spectra at three different redshift ($z = [0.30, 0.55, 0.70]$) and at four values of S/N in the observed I-band $S/N_{I,\mathrm{obs}} = [10, 20, 30, 50]$. We focused on the constraint of the metallicity by measuring key UV and optical absorption-line indices for each simulated galaxy and using a Bayesian approach with an extended galaxy templates library to retrieve the mass-weighted metallicity with an accurate estimate of the expected observational errors. We found that, in general, the available spectral indices can be used to reliably constrain stellar metallicity already at $S/N_{I,\mathrm{obs}} = 10$, with $\sigma \leq 0.3$ dex for galaxies older than ~ 2 Gyr. Below this age, metallicity indices are weak, and mostly sensitive to the temperature of the stars, namely, to the age of the stellar population.

Our results are in good agreement with other theoretical (Choi et al. 2014) and observational (Gallazzi et al. 2005) results in literature, also demonstrating how metallicity estimates can take advantage of including bluer and UV indices together with the classic optical ones.

Finally, we performed a direct comparison among different sets of indices when characterising the stellar metallicity to show the importance and the efficiency of using bluer and UV indices. For the comparison to be fair, we relied on a new set of simulated spectra with fixed S/N along the continuum around each spectral index. We found that results similar to those obtained with fewer optical (e.g. [Hβ, Mgb, Fe5270]) indices at relative high S/N can be obtained with a wider set of bluer indices ([BL3580, Fe3619, Hδ_{F}, Hγ_{F}, G$_{\mathrm{band}}$4300, Fe4383, Ca4455, Fe4531, Hβ]), over a larger wavelength baseline, at lower S/N. We emphasised that one main advantage of blue spectral indices is that of avoiding wavelength regions, in the galaxy observed frames, that are strongly affected by atmospheric contamination (both emission lines and telluric lines) at intermediate redshift. However, blue indices are expected to be more impacted by the effect of non-solar abundance ratios, though the latter become less and less important at young ages (i.e. higher redshifts).

In this Chapter we demonstrated that combining carefully selected UV and optical indices within a Bayesian framework enables accurate estimates of stellar ages and metallicities from medium-resolution, moderate-S/N spectroscopic data, highlighting which features and S/N regimes are most informative at intermediate redshift. A natural next step is therefore to test stellar population diagnostics by moving from simulations to real obser-

vations, and to explore the other methods described in Chap. 1.5. In Chapter 3 we indeed pursue this goal by moving from simulations to a resolved case study: the Cartwheel galaxy, the archetypal collisional ring galaxy (hereafter RiG; see e.g. Athanassoula & Bosma 1985) in the local Universe. This object is the ideal testbed of the methodology presented here, due to the different stellar population properties it displays in its different regions.

Chapter 3

Understanding the unusual life of the Cartwheel galaxy using stellar populations

This chapter is based on Ditrani et al. 2024, A&A, 688, A89.

As illustrated in Chapter 2, the analysis of spectral indices measured on integrated galaxy spectra is extremely successful in deriving their age and metallicity. However, the previous study was based on simulated galaxies rather than real data. We now apply the study of stellar population parameters to real observations. The target of our analysis is the archetypal collisional ring system, the Cartwheel Galaxy. This system represents one of the most extreme environments in which we can study star formation, not only for the energetic contribution from the encounter, but also due to a relatively 'clean' population of spatially segregated regions, which can be studied individually. This implies that the Cartwheel is an ideal laboratory for testing how stellar populations can trace the timing and physics of a recent collision.

In this chapter, we present a resolved analysis of the Cartwheel galaxy, with an emphasis on the stellar component and an explicit link to nebular physics. Compared to the classical analysis presented in the previous chapter, in this work we explore the use of an innovative approach, the full-index fitting described in Chap. 1.5.3 on the high S/N data from VLT/MUSE to map the spatial distribution of stellar ages and metallicities across the Cartwheel. We model their spatial variation with a hierarchical Bayesian modeling to test for inhomogeneities. We then integrate the FIF posteriors with nebular constraints and GALEX–to–JWST photometry in a joint full spectral + SED fitting framework (MC-SPF), to reconstruct the recent star formation history and to date the propagating ring, thereby linking dynamical evolution to the resolved stellar fossil record in an extreme environment.

3.1 The Cartwheel galaxy

Collisional ring galaxies (hereafter RiGs; see e.g. Athanassoula & Bosma 1985) are a peculiar class of galaxy thought to have suffered violent interaction events in the recent

past. They appear to be the result of the impact between two galaxies, with the smaller one passing through the disc of the larger one, which is referred to as the target galaxy, close to its centre. In this framework, a shock wave front induced by the impact starts to propagate within the disc of the target galaxy soon after the encounter, producing the characteristic expanding external ring (e.g. Lynds & Toomre 1976; Theys & Spiegel 1977; Hernquist & Weil 1993; Mihos & Hernquist 1994; Horellou & Combes 2001; Mapelli et al. 2008a,b).

The most famous RiG is the Cartwheel galaxy, a member of the compact group SGC 0035−3357 in the southern hemisphere (Iovino 2002) at redshift $z = 0.03$ (Amram et al. 1998), corresponding to a luminosity distance of 131 Mpc. The Cartwheel galaxy has been the object of many studies, both theoretical and observational, but the details of the mechanisms that lead to its peculiar morphology and its physical properties are still far from clear. More specifically, the age of the collision, a critical quantity in order to understand the evolution and dynamics of the galaxy, is not easy to establish: Higdon (1996), analysing the HI velocity fields, inferred that 300 Myr have passed since the impact; Amram et al. (1998) estimated the age of the ring at > 200 Myr from the Hα kinematics ($13 - 30$ km s^{-1} expansion). Struck et al. (1996) further suggested that the expanding external ring loses material that moves back towards the nucleus along the spokes, triggering star formation events. The simulations of Renaud et al. (2018) follow a similar dynamical scenario, but with a shorter timescale (< 100 Myr) for the persistence of the ring. Recently, Zaragoza-Cardiel et al. (2022) analysed the oxygen abundance in the HII regions populating the external ring of the Cartwheel galaxy, and found that it is lower by ≈ 0.1 dex with respect to the extrapolation of the inner radial gradient. This observed evidence has been interpreted as due to the effect of dragging by the shock wave that leaves the inner regions of the galaxy almost undisturbed, while displacing both the stars formed during the collision and the potential metal-poor gas from the bullet galaxy into the structure that we recognise as the external ring. The recent work of Mayya et al. (2024), who analysed Astrosat/UVIT far ultraviolet (FUV) imaging data of the Cartwheel galaxy, revealed evidence of a wide range of ages of the stellar populations in the HII regions of the external ring, supporting the collision model of Renaud et al. (2018).

The collision scenarios can be strongly discriminated by means of spatially resolved studies of the stellar and nebular content in RiGs. Indeed, the stellar and nebular properties in galaxies and their spatial distribution contain the signatures of the physical processes that lead to their formation and present morphology. Mergers and interactions among galaxies have the effect of mixing different stellar populations and producing gas inflow and outflow, which can trigger star formation activity (e.g. Hopkins et al. 2013; Ferreras et al. 2017).

3.2 Observational data and region identification

We used integral field spectroscopic data of the Cartwheel galaxy from the Multi Unit Spectroscopic Explore (MUSE) mounted on UT4 of the ESO Very Large Telescope. Four mosaicked observations have been carried out during the MUSE science verification run in August 2014 (program ID: 60.A-9333) and cover a field of view (FoV) of 2×2 arcmin, including the entire ring (1.4×1.5 arcmin). These data have a total exposure time of 8400 s. We downloaded the fully reduced 3D science data cube from the ESO Science Portal. The data cover the wavelength range from 4750 to 9351 Å, with a spatial sampling of 0.2 arcsec/pixel, a spectral dispersion of 1.25Å and a spectral resolution of ~ 3 Å (Bacon et al. 2010). Figure 3.1 shows a colour image of the Cartwheel galaxy obtained using the

MUSE data cube and considering three wavelength ranges as pseudo photometric bands: $4800 - 6100$Å as B channel, $6100 - 7500$Å as G channel, and $7500 - 9000$Å as R channel.

We also exploited the available photometric data for this galaxy: FUV and NUV imaging from the Galaxy Evolution Explorer (GALEX, Martin et al. 2005) program GI1-045002, OmegaCAM-VST u-, g-, r-, i- and z-band images from the public survey (Kuijken et al. 2011), the JWST-NIRCam F090W, F150W, F200W, F277W, F356W and F444W images, and the JWST-MIRI F770W, F1000W, F1280W and F1800W images from the JWST Early Release Observation 1 (ERO PID 2727, PI Pontoppidan).

In this work we are interested in deriving the stellar population properties in different regions of the Cartwheel galaxy, with the aim of gaining insights on the formation mechanisms which shaped its complex morphology. To address this aim, we started to identify specific spatial regions on the basis of the distribution of the star formation activity. We extracted the flux maps of the Hα and [NII]6548-6583Å emission lines from the data cube using the KUBEVIZ code (v2.0). We refer the readers to Fossati et al. (2016) for the details of the emission line fitting procedure. The code fits the Hα+[NII] emission line complex with three Gaussians which share a single recessional velocity and velocity dispersion as free parameters. The flux ratio of the [NII]6548-6583Å emission lines is fixed to the values from atomic physics given in Storey & Zeippen (2000). The code first fits all pixels in the MUSE datacube independently. Individual pixels where the S/N of the Hα line is less than 5 are then masked. Masked pixels which are adjacent to unmasked ones are fit again, this time using the average values from the fits of nearby good pixels as initial guesses. The code starts from bad fits that are surrounded by the highest number of good fits and iteratively re-evaluates the masking, gradually moving to more isolated masked fits until no further improvement to the spatial flux map is found (see Fossati et al. 2019, for more details on the iterative procedure).

Figure 3.2 shows the MUSE map of the Hα line flux for pixels with $S/N > 5$ for the Cartwheel galaxy. We readily noticed that the Hα distribution is structured in at least three separate spatial regions: a nuclear region (hereafter nucleus, black line), an inner ring (grey line), and an outer ring (in blue). We also defined a region between the inner ring and the outer ring (hereafter the in-between region).

3.3 Spectral extraction: Stellar continuum and nebular emission

From the four spatial regions identified on the Hα map of the galaxy, we selected the spaxels with $S/N > 5$ in Hα (neglecting the corresponding stellar absorption) and with uncertainties of the Hα+[NII]6548-6583Å kinematics lower than 50 km s^{-1}. We extracted the spectra from each of the selected spaxels, and shifted them to rest-frame using the recessional velocity estimate derived from the Hα+[NII]6548-6583Å lines. After that, we shifted to the same common rest-frame also the spectra extracted from the spaxels with $S/N < 5$ in Hα, for which no reliable kinematic information could be obtained, by interpolating a 2D model of the recession velocity field defined by the significant emission lines. Our investigation is a three-step analysis, where the first two consist of separate analyses of the stellar and nebular components of the four spatial regions of the galaxy, while the third is a joint fit of all the available photometric and spectroscopic data and is partly based on the results obtained in the first two steps. For the analysis of the first step, we obtained the co-added spectrum of each spatial region excluding from the sum spectra coming from the spaxels within the HII regions identified in Zaragoza-Cardiel et al. (2022), in order to limit the overwhelming nebular emission in those regions. Indeed, the

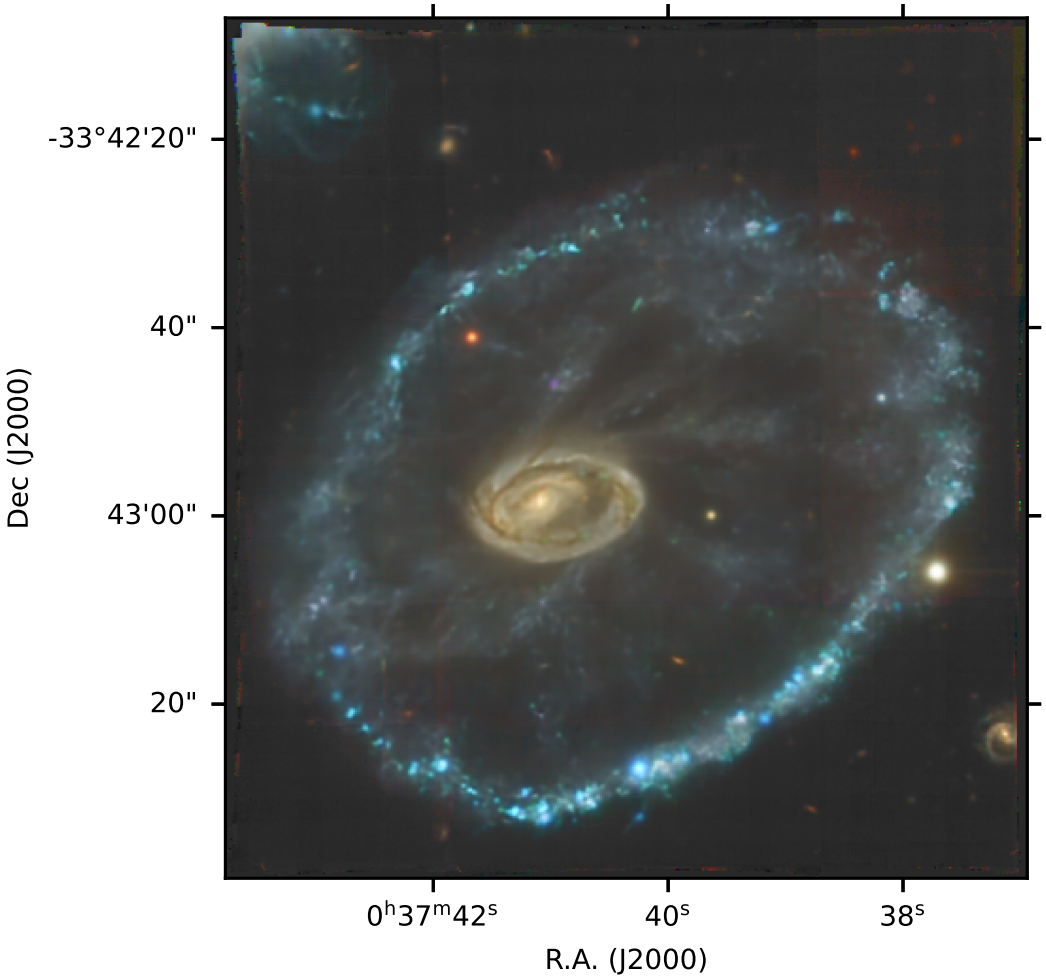

Figure 3.1: False-colour image of the Cartwheel galaxy from MUSE data. Each RGB channel was constructed from the reduced MUSE data cube by projecting it in the wavelength ranges $4800-6100$Å, $6100-7500$Å, and $7500-9000$Å for the B, G, and R channels respectively. The image covers a field of view of $\approx 2 \times 2$ arcmin equivalent to nearly 74 kpc on a side at the Cartwheel's redshift.

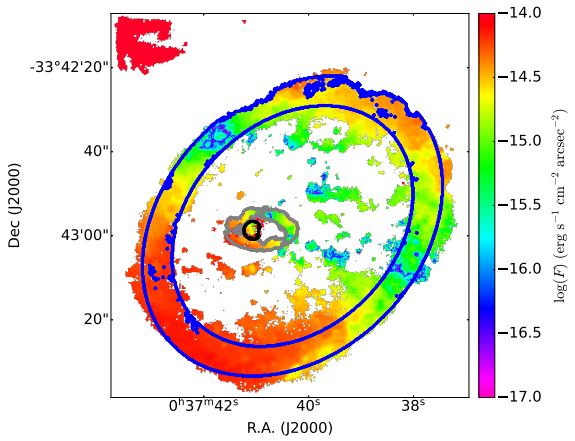

Figure 3.2: MUSE Hα map of the Cartwheel galaxy, where the coloured pixels correspond to S/N(Hα) > 5 and with kinematic uncertainties on the strongest line lower than 50 km s^{-1}. The black, grey, and blue contours indicates the 'nucleus', 'inner ring' and 'outer ring' regions, respectively. The 'in-between' region is defined by the outer grey contour and the inner blue contour.

aim of this part of the analysis is to get insights on the mean properties of the stellar content in each of the four regions of the Cartwheel galaxy. The nebular emission lines which are clearly visible in all the four regions are certainly due to highly ionising stars which are mainly confined within the brighter HII regions and which have been dated in a recent paper by Mayya et al. (2024). Differently from their study, the aim of our analysis of the stellar spectra is to determine the mix of stellar populations characterizing each region in the Cartwheel galaxy, including both the precollisional component and stars possibly formed in the inner part of the galaxy when the shock wave was in more backwards positions. Stars within HII regions are so young and bright that would bias the results dominating the total light. The exclusion of the HII regions allows us then to study in a more reliable way the mean stellar population parameters of the Cartwheel galaxy, even in regions that would otherwise be dominated by nebular emission. Consistently with Zaragoza-Cardiel et al. (2022), we modelled each HII region with a circular region of radius 0.6 arcsec, equivalent to 370 pc, and we excluded them.

Differently from this, for the further two analysis steps, we summed fluxes from all the available spaxels in order to obtain the co-added spectra representative of the overall emission of each of the four spatial regions in the Cartwheel galaxy. In the outer ring, we also extracted a further co-added spectrum corresponding to the HII regions alone, for which we performed only the nebular component analysis for comparison with other literature studies.

To improve upon the statistical significance of the results and given the large spatial dimensions of the selected regions, we divided the inner ring in four equally extended subregions, the in-between region in eight subregions, and the outer ring in 16 subregions, while we keep a single spectrum as representative of the nucleus.

We based the analysis of the stellar component on the rest-frame wavelengths between 4650 Å and 5400 Å, the range that is most sensitive to the age and metallicity of the stars. For the analysis of the nebular components and for the full spectral fitting one, we considered spectra over a larger wavelength range, between 4650 Å and 7200 Å restframe, including both Hβ and Hα lines. For each co-added spectrum, we then separated the stellar and nebular components. To this aim, we first estimated the corresponding stel-

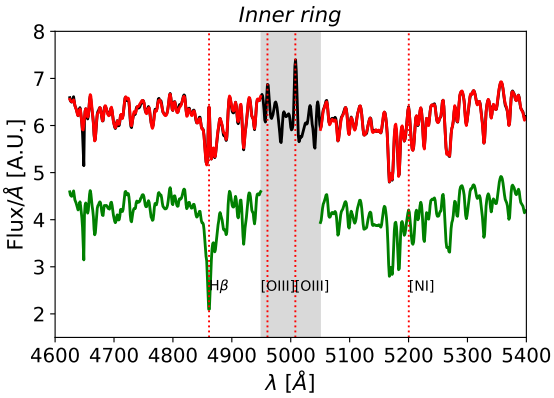

Figure 3.3: pPXF fit for the spectrum of one subregion of the inner ring. The black line marks the observed spectrum, the superimposed red line is the pPXF best-fit, and the green line is the observed spectrum to which the emission line are subtracted, shifted for clarity. The grey region is masked in the pPXF fit.

lar kinematics (i.e. residual redshift and velocity dispersion). Since different wavelength ranges receive light contributions from different stellar components, which can be characterised by slightly different kinematics, we performed the kinematic analysis using the absorption features in the range between 4650 Å and 5400 Å, which is the spectral region used for the stellar analysis. We obtained the residual redshift and velocity dispersion on the co-added spectra exploiting the latest version of the pPXF (Penalized PiXel-Fitting) code (Cappellari & Emsellem 2004; Cappellari 2017, 2023). We adopted the MILES stellar spectral library (Sánchez-Blázquez et al. 2006), convolved to the MUSE instrumental resolution, as model template library.

We then decoupled the stellar component from the nebular one in each spectrum, running again the pPXF code, this time fixing the kinematics measured in the previous stage. In this case, we used the E-MILES simple stellar population (SSP) synthesis models (Vazdekis et al. 2016), obtained assuming the BaSTI tracks (Pietrinferni et al. 2004, 2006) and Chabrier (2003) IMF. We fitted the nebular emission lines assuming 6 moments of their kinematic, since we tested that the use of less moments (e.g. a simple Gaussian fit) limits the fit quality, especially for strong emission lines, and produces a residual component affecting the extracted stellar continuum spectra. Finally, we subtracted the best-fit nebular components from the total spectra, deriving clean stellar component spectra for each of the four regions. Figure 3.3 shows an example of the extracted stellar spectrum of the inner ring using pPXF. The pPXF code was able, for each spectrum, to perform an accurate fit of the stellar component, disentangled from the emission nebular one.

3.4 Analysis

In this section, we describe the details of the analysis performed on the four identified regions of the Cartwheel galaxy. As mentioned in Chap. 3.3, we divided the analysis into three separate steps. The first one is the analysis of the stellar components (Chap. 3.4.1 and 3.4.2). The second step is the analysis performed on the nebular emission of each of the four regions (Chap. 3.4.3), and the last step is the joint photometric and spectroscopic analysis aimed at deriving the SFH of the four regions on the basis of the information derived with the previous methods (Chap. 3.4.4).

3.4.1 Stellar population properties via full-index fitting

We prepared a set of comparison templates based on the SSP models by Vazdekis et al. (2016), with the aim of extracting information on the stellar age and metallicity in the four regions of the Cartwheel galaxy from their stellar spectra. Models adopt the BaSTI tracks (Pietrinferni et al. 2004, 2006) combined with the MILES (Sánchez-Blázquez et al. 2006; Falcón-Barroso et al. 2011, 2.51Å FWHM resolution) empirical stellar library, and assuming the Chabrier (2003) IMF. The synthetic template library contains 636 SSPs unevenly spaced in linear age and [Z/H], covering 53 age from 0.03 Gyr to 14 Gyr and 12 metallicities from [Z/H]=−2.27 to [Z/H]=0.4. We made the simple assumption that each region can be described by the combination of two SSPs, one older than 2 Gyr and the other younger than 4 Gyr. The old component represents the precollisional population of the original galaxy and is not expected to be younger than 2 Gyr, while the young component can trace the possible stars recently formed as a consequence of the impact with the bullet companion. According to dynamical measures, the collision has taken place in the last few hundred Myrs, but we leave a larger age range (up to 4 Gyr) as a prior, to be flexible towards a scenario where no stars are formed during the impact in some regions. In the latter case, the age range overlap between the two SSPs (old and young ones) allows us to take into account the possible complex SFH of the original galaxy that cannot be matched by a single SSP. We tested that the 2 SSPs model can successfully constrain the physical parameters of both populations until the young component (i.e. younger than 1 Gyr) mixed with the older one (i.e. older than 3 Gyr) represents a not-too-large fraction of the total mass (i.e. $< 30\%$). On the other hand, if the fraction of the young component is higher than 30% of the total mass, the light contribution of this component will start to dominate the spectrum and the 2 SSPs model will start to fail to constrain the older population.

We based the comparison between the stellar spectra and the synthetic spectral templates on the analysis of four spectral indices: Hβ_o (Cervantes & Vazdekis 2009), sensitive to the age of the stellar populations, and Mgb, Fe5270 and Fe5335 (Worthey et al. 1994), sensitive to the stellar metallicity. Given the high quality and resolution of the MUSE spectral data, we decided to follow the full-index fitting approach (FIF, Martín-Navarro et al. 2014) to derive the stellar population parameters of each region of the Cartwheel galaxy. Differently from the more classic index fitting approach, with FIF the comparison of the flux within a specific absorption feature of an index (with respect to its continuum value) is made pixel by pixel and not on average. The comparison of single pixel fluxes within the index window is then more efficient in breaking the degeneracy between age and metallicity with respect to the classic index analysis, since not only the strength of the absorption feature is taken into account, but also its specific shape, which brings information on the stellar population parameters (Martín-Navarro et al. 2019). The FIF technique has several advantages also with respect to the full spectral fitting, because in the former case only the spectral features are fitted (not the continuum), optimising the information gained and reducing the computational time. Figure 3.4 shows an example of the application of the FIF approach on the inner ring of the galaxy. The best-fit template follows the shape of each spectral feature in an accurate way and then optimises the information gained pixel by pixel.

3.4.2 Hierarchical Bayesian modelling

In Chapter 3.3 we explained that, given the large dimensions of three out of the four regions selected in the Cartwheel galaxy, we could divide them in subregions in order to perform a

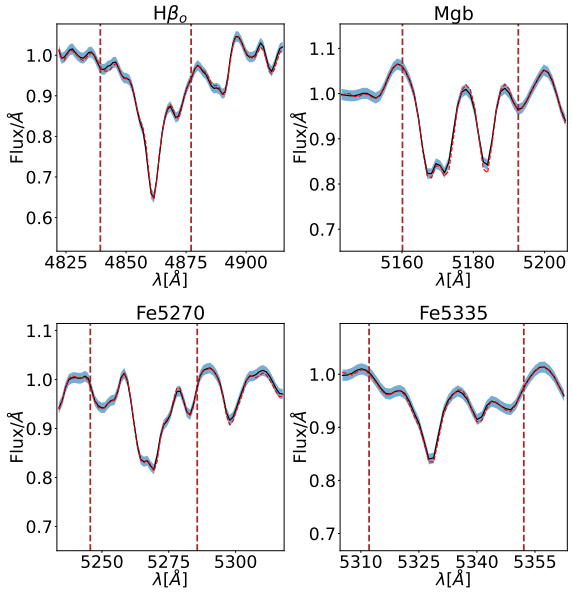

Figure 3.4: FIF application on the four spectral indices of the inner ring spectrum used. The vertical dashed brown lines mark the central feature of each index. The spectral features are normalised using the index pseudo-continua (grey shaded regions). The black lines and the blue shaded regions represent the observed spectrum and the relative uncertainties, respectively, while the superimposed red dashed lines are the best-fit obtained from the posterior distribution.

spatially resolved analysis of the entire galaxy. To assess the stellar population parameters of each region, we then need to combine the results obtained from their different subregions and we adopted a hierarchical bayesian modeling. In the hierarchical framework, our models consist of two levels, being the first one that of the individual measurements in each subregion, and the second one their distribution within the entire region. Following an 'a posteriori' approach, as in Beverage et al. (2023), as the first level of the models we computed the posterior probability of age and metallicity of each SSP template used to fit the stellar spectra and their relative fraction for each subregion, using the likelihood given by $\mathcal{L} = e^{-\chi^2/2}$, with

$$\chi^2 = \sum_i \left(\frac{F_{obs_i} - F_{syn_i}}{\sigma_{obs_i}} \right)^2, \tag{3.1}$$

where F_{syn_i} is the flux of the synthetic spectrum along the feature of each index, and F_{obs_i} is the flux of the observed spectrum with the error σ_{obs_i}. The index i indicates the ith pixel on which the calculation takes place. We assumed a uniform prior for age and [Z/H] for both SSPs, and for the relative fraction of the two components, i.e. young and old. We considered an age range from 2 Gyr to 14 Gyr for the old component and from 0.03 Gyr to 4 Gyr for the young one, while we used the whole metallicity range for both the two components, from [Z/H]=−2.27 to [Z/H]=0.4. We explored the parameter space with a Markov Chain Monte Carlo method (MCMC, Gilks 2005), and the 68% confidence interval is delimited by the 16° and 84° percentile. Then, as a second level modeling, we fitted the posterior distribution of each parameter in each subregion using a Student-t distribution. This allows us to take into account the effects of a higher kurtosis in the distribution of the stellar parameters. With this approach, we can then obtain a mean value of the estimated parameters in the whole regions with a reliable estimate of their

Table 3.1: Median values of the marginalised posterior distribution for each subregion.

Region	$\sigma_{\rm region}$ [km s^{-1}]	$\rm Age_{old}$ [Gyr]	$\rm [Z/H]_{old}$ [dex]	$\rm Age_{young}$ [Gyr]	$\rm [Z/H]_{young}$ [dex]	$\rm Fraction_{old}$
nucleus	72	$3.17^{+0.43}_{-0.34}$	$-0.06^{+0.05}_{-0.05}$	-	-	-
inner ring	73	$5.62^{+3.94}_{-1.97}$	$0.20^{+0.11}_{-0.13}$	$0.87^{+0.22}_{-0.23}$	$-0.87^{+0.32}_{-0.26}$	$0.94^{+0.02}_{-0.03}$
in-between	65	$3.42^{+1.80}_{-0.90}$	$0.12^{+0.11}_{-0.11}$	$0.80^{+0.06}_{-0.14}$	$-1.06^{+0.09}_{-0.07}$	$0.84^{+0.03}_{-0.03}$
outer ring	54	-	-	$0.10^{+0.02}_{-0.02}$	$-1.11^{+0.04}_{-0.05}$	-

The first column shows the velocity dispersion measurement of each region obtained from the pPXF fit. The subsequent columns show the age and stellar metallicity of the two SSPs model and their relative fraction. The errors on the median values refer to the 16th and 84th percentiles.

errors, accounting also for their intrinsic scatter among the different subregions. For this second fit, we assumed the same uniform prior described above for each stellar population parameter, then a logarithmically uniform prior for the intrinsic scatter in the range from 0.01 to 10, and a logarithmically uniform prior for the degrees of freedom of the Student-t distribution, in the range from 1 to 10, where 1 is an heavy-tailed distribution and 10 is a Gaussian one. Figure 3.5 shows an example of the posterior probability distribution of the $\rm Age_{young}$, its scatter and the degrees of freedom of the Student-t distribution for the inner ring.

Differently from the other regions, for the nucleus we analysed a single spectrum considering only the first of the two layers of the modeling. As it will be better explained in Sect 3.4.4, the analysis of the nucleus using the FIF approach did not reveal the presence of a density or shock wave induced past SF population (i.e. young component). Therefore for this region we adopted a simpler SFH described by a single SSP model. Similarly, the FIF analysis of all the subregions in the outer ring did not reveal the presence of the pre-collisional population (i.e. old component). Therefore, also for this region we adopted the single SSP modeling, with the goal of finding not only a mean stellar age and metallicity but also their possible intrinsic scatter between the 16 subregions in which we divided this region.

Table 4.2 reports the velocity dispersion, the median values of the marginalised posterior distribution of age and metallicity of the 2 SSPs and their relative mass fraction for each spatial region. Table 3.2 reports the median values of the marginalised posterior distribution of the scatter of age and metallicity of the 2 SSPs and their relative mass fraction for each spatial region. It is immediately clear that the scatter between the subregions within the inner ring and the in-between is negligible or comparable to the uncertainties for all the measured parameters. On the other hand, we measured a noticeable scatter on the mean age in the outer ring, which we discuss in detail in Chap. 3.5.4.

3.4.3 Properties of the nebular emissions

The nebular spectrum contains valuable information to help in constraining the physical parameters of a galaxy, most notably the gas ionisation mechanism, its metallicity and the

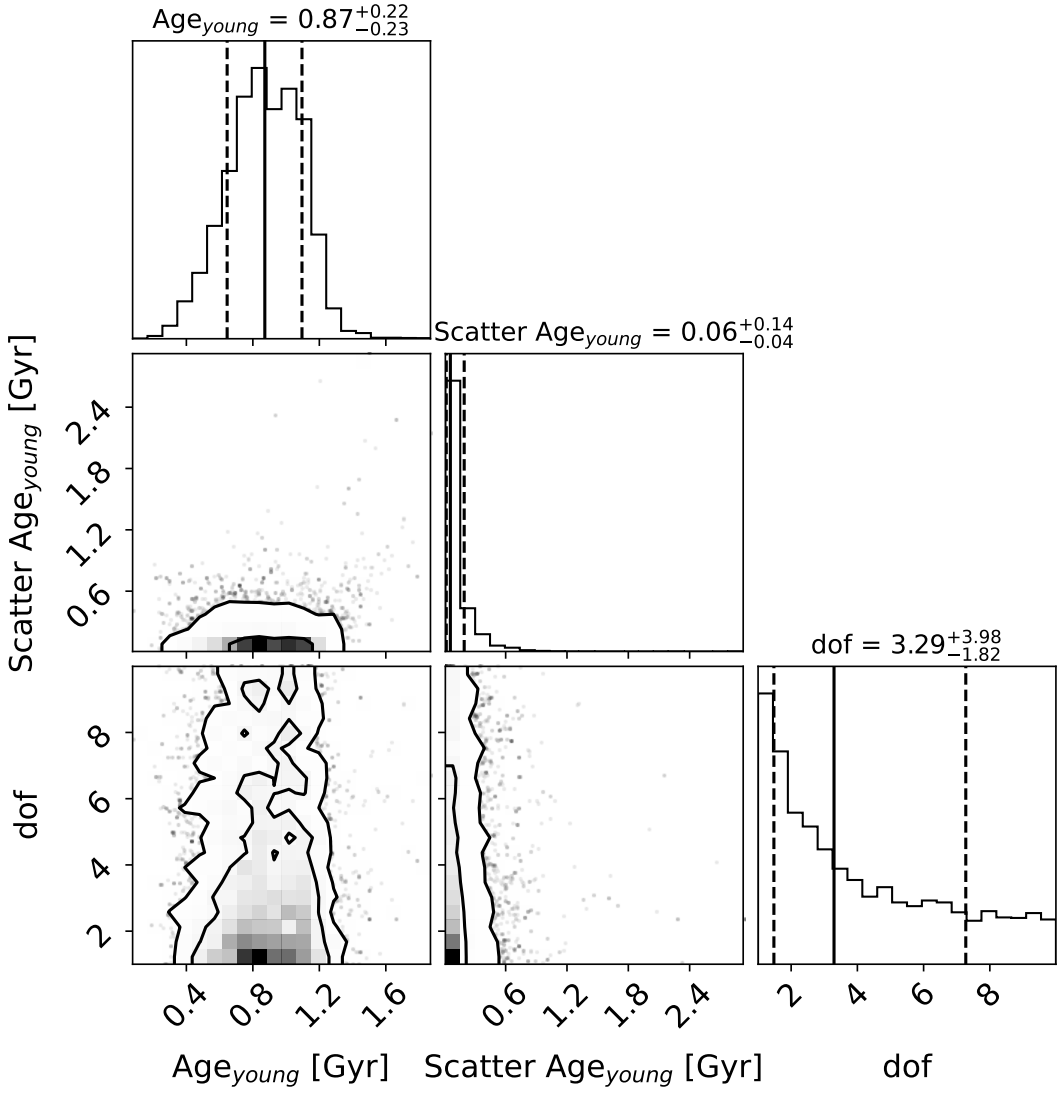

Figure 3.5: Corner plot summary of the posterior distributions of the Age$_{young}$, its scatter, and the degrees of freedom of the Student-t distribution obtained for the four subregions of the inner ring of the Cartwheel galaxy. The panels on the diagonal show the 1D histogram for each model parameter obtained by marginalising over the other parameters, with median and 16% – 84% intervals indicated by solid and dashed lines, respectively. The off-diagonal panels show 2D projections of the posterior probability with contours at the 68% and 95% levels.

Table 3.2: Median values of the marginalised posterior distribution of the intrinsic scatter within the different subregions.

Region	Age_{old} [Gyr]	$[Z/H]_{old}$ [dex]	Age_{young} [Gyr]	$[Z/H]_{young}$ [dex]	$Fraction_{old}$
nucleus	N.A.	N.A.	-	-	-
inner ring	$0.14^{+0.77}_{-0.11}$	$0.03^{+0.06}_{-0.02}$	$0.06^{+0.14}_{-0.04}$	$0.05^{+0.17}_{-0.04}$	$0.02^{+0.02}_{-0.01}$
in-between	$0.06^{+0.26}_{-0.04}$	$0.03^{+0.06}_{-0.02}$	$0.03^{+0.05}_{-0.01}$	$0.04^{+0.10}_{-0.03}$	$0.02^{+0.02}_{-0.01}$
outer ring	-	-	$0.07^{+0.02}_{-0.02}$	$0.11^{+0.06}_{-0.05}$	-

The columns show the scatter of age and stellar metallicity of the two SSPs model and their relative fraction. The errors on the median values refer to the 16th and 84th percentiles.

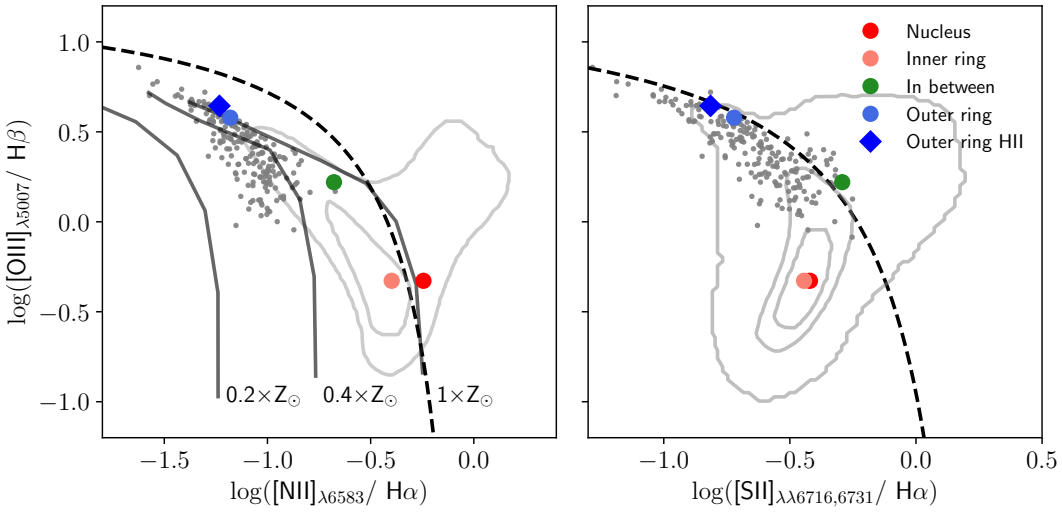

Figure 3.6: BPT diagnostic diagrams [OIII]/Hβ vs. [NII]/Hα (left), and [SII]/Hα (right) derived from the composite spectra extracted from the five regions of the Cartwheel galaxy. The small grey points are the individual HII regions from Zaragoza-Cardiel et al. (2022). The grey contours are obtained from the nuclear spectra of a sample of 50,000 SDSS galaxies at $0.03 < z < 0.08$ whose emission lines are detected at $S/N > 5$. The dashed lines indicate the separation between the stellar photoionisation processes (towards to left) and AGN/shock ionisation (top and right) as defined in Kauffmann et al. (2003) (K03, left panel) and in Kewley et al. (2006) (K06, right panel). The black solid lines in the left panel show the tracks from photoionisation models of Kewley et al. (2001) for three different metallicities (0.2, 0.4, and $1 Z_{\odot}$).

dust extinction in the stellar birth places. Figure 3.6 shows the BPT (Baldwin et al. 1981) diagnostic line ratios [OIII]/Hβ vs. either [NII]/Hα (left panel), or [SII]/Hα (right panel) derived from the composite spectra extracted from the four regions of the Cartwheel galaxy, and a fifth region constructed as the sum of the emission from the HII regions identified in the external ring in Zaragoza-Cardiel et al. (2022). Both diagrams show that the ionisation of the *Outer ring* and the *in-between* regions is consistent with photoionisation by recent star-formation. In particular, the *Outer ring* exhibits a strong ionisation parameter, which is even stronger when we analyse the HII regions only, indicating significant star formation activity in the region. The template spectrum of the HII regions in the *Outer Ring* has line ratios in agreement with the locus of the points of the individual HII regions from Zaragoza-Cardiel et al. (2022), as also confirmed by Mayya et al. (2023). Conversely, the *Nucleus* has line ratios consistent with a weak active galactic nucleus (AGN) when the [NII] BPT diagrams is used, although the line ratios could also be consistent with hot evolved stars (Belfiore et al. 2016). No AGN is detected with X-ray Chandra data, and only a variable source with maximum luminosity of $L_X\ (2-10\ \mathrm{keV}) = 1.4 \times 10^{39}$ erg s^{-1} is present in the nuclear region (Salvaggio et al. 2023), suggesting the latter hypothesis. The *Inner Ring* has line ratios consistent with those of the *Nucleus*, indicating a similar origin of the nebular ionisation.

Given the predominant role of stellar ionising photons on the ionisation conditions of the nebular gas, it is possible to derive the gas-phase metallicity from a combination of nebular emission line ratios, and to compare it with that of the two stellar populations adopted to model each region within the Cartwheel galaxy (see Chapter 3.4.1). Figure 3.7 shows the nebular spectra extracted from each region. We noticed the similarity of the nebular spectra extracted from the nucleus and from the inner ring, implying a similar gas-phase metallicity. Moving towards the outer ring, the increase of the [OIII] lines over the $H\beta$ line and the corresponding decrease of the [NII]/$H\alpha$ ratio mark the evidence of a decrease of the gas-phase metallicity. From the empirical calibration of Curti et al. (2017) for strong-line diagnostics of gas-phase metallicity, we derived metallicity estimates based on R_3, N_2 and O_3N_2 indicators. The different estimates are in excellent agreement with each other. In Table 3.3 we reported the values resulting from the R_3 indicators, where the uncertainty has been derived from the dispersion of the corresponding empirical curve. As a further check, we also applied the empirical calibration by Charlot & Longhetti (2001), finding gas-phase metallicity values well matching the previous ones. From Table 3.3 we can see the decrease of the gas phase metallicity from the solar value in the inner part of the Cartwheel galaxy to less than half of the solar value in the outer ring.

We derived an estimate of the amount of dust extinction by measuring the Balmer decrement between Hα and Hβ, assuming a case B value of their ratio equal to 2.86 and the Calzetti attenuation law (Calzetti 2001). We then derived the current SFR in each region from the luminosity of the Hα line, corrected for the calculated extinction, adopting the conversion factor of Kennicutt (1998) reported to the Chabrier IMF (Driver et al. 2013). Under the assumption of the Hα/SFR conversion factor of Kennicutt (1998) and the extinction curve of Calzetti (2001), both SFR and A_V are subject only to the statistical errors in measuring line fluxes, and since these are very small ($< 0.5\%$), they result in negligible uncertainties in their estimates. Table 3.3 summarises all the quantities measured on the nebular component of each of the four regions.

3.4.4 Reconstruction of the SFHs using MC-SPF

Finally, we also jointly fitted the photometric and spectroscopic data to extract the SFH of each region of the galaxy using the Python code Monte Carlo Spectro-Photometric Fitter

Table 3.3: Nebular parameters.

Region	$[Z/H]_{gas}$ [dex]	A_V [mag]	SFR $M_\odot$ yr^{-1}
nucleus	0.01 ± 0.07	2.46	0.13
inner ring	0.01 ± 0.07	2.21	0.38
in-between	-0.17 ± 0.07	0.66	0.73
outer ring (No HII)	-0.32 ± 0.07	0.56	5.52
outer ring (Only HII)	-0.41 ± 0.07	0.47	3.73
outer ring (With HII)	-0.36 ± 0.07	0.52	9.17

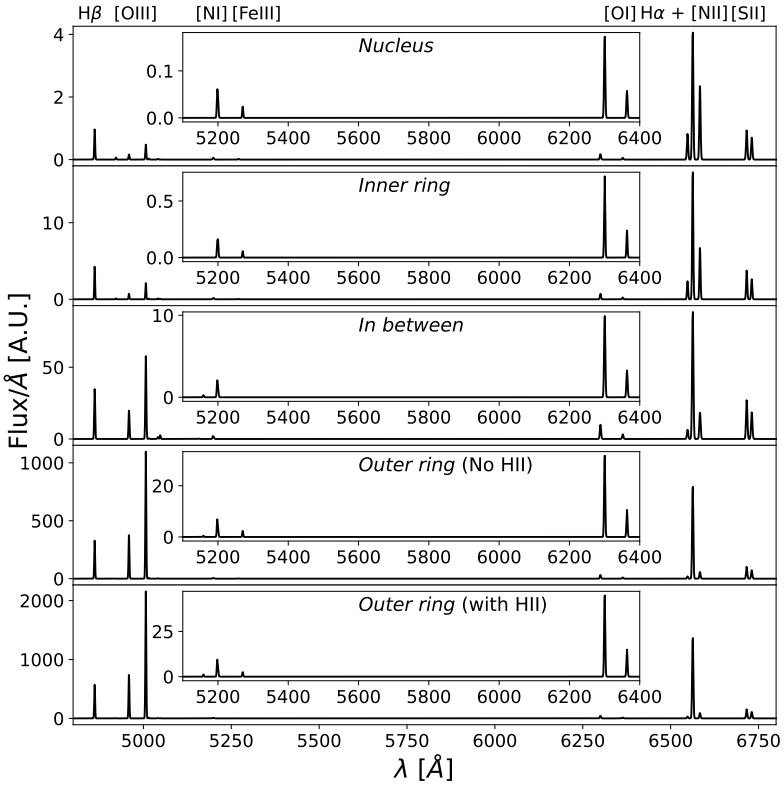

Figure 3.7: Nebular spectra of each region of the Cartwheel galaxy, as indicated in each panel. The inset shows a zoom onto the central part of the spectrum. Strong emission lines are reported at the top of the figure.

(MC-SPF, Fossati et al. 2018). As input data, we used the 1D spectra extracted in the four regions of interest, complemented by the fluxes in each photometric band integrated over the same regions, after subtracting an appropriate background for each region and band. The instrumental point spread function of diffraction limited observations and the seeing conditions of ground based data vary from 0.6 arcsec for JWST-NIRCam F090W to ≈ 5 arcsec for the GALEX data. However, given the large apertures of spectral extraction adopted we did not match the images to a common PSF.

On the MC-SPF code side, we made numerous updates motivated by the needs of this investigation. First, the complex SFH of the different regions of the Cartwheel make the use of parametric SFHs impractical. We therefore chose a nonparametric SFH approach, informed by the stellar and nebular parameters obtained as described in Chap. 3.4.1 and 3.4.3. The aim of this third approach is to verify how the ages recovered in the analysis based on the FIF for the stellar components can be produced by a simplified SFH. For each region, we defined a piece-wise constant SFH in three age bins, an old one ranging from the age of the old SSP to the age of the young SSP and characterised by the stellar metallicity of the old SSP; a young one spanning the time from the young SSP age to 30 Myr ago (the maximum age of the ionising stars); and the youngest one, linked to the current star formation activity and to nebular line emission, ranging from 30 Myr ago to the present day. The last two bins have the stellar metallicity of the young SSP. The code performs the fit varying the relative weights of SFR in these three time bins, determining their relative fractions defined as $\mathrm{Frac_{old}}$, $\mathrm{Frac_{young}}$ and $\mathrm{Frac_{youngest}}$ (where $\mathrm{Frac_{youngest}} = 1- \mathrm{Frac_{old}} - \mathrm{Frac_{young}}$), respectively. We generated model spectra from these SFHs using SSPs from the latest version of the Bruzual & Charlot (2003) (named as C&B, see Plat et al. 2019; Sánchez et al. 2022), where we selected the closest metallicity template to the one identified in each bin of the SFHs. Each SSP template provides 220 spectra computed at different time steps ranging from 0.01 Myr to 14 Gyr, with a metallicity ranging from -1.7 dex to 0.4 dex. We assumed a Chabrier IMF with $M_{UP} = 100\mathrm{M}_\odot$ and the MILES stellar library, in order to be consistent with the models used for the retrieval of the stellar parameters in Chap. 3.4.1.

For the nucleus and the outer ring, the FIF analysis shows that disentangling stellar populations of largely different ages is difficult as these spectra can be modelled with a single population of stars (old in the case of the nucleus and young in the case of the outer ring). For these reasons, we followed a different approach in building the SFHs for these regions. We generated a piece-wise constant SFH in only two age bins, with a single stellar metallicity and an upper age of 10 Gyr. In addition to leaving the star formation fraction of the two bins variable, in the case of the nucleus the SFH is regulated by a free parameter (JumpAge Old) when the old component will cease to form. At a later time (JumpAge Young), the SF activity will resume. These models have three free parameters and are highly flexible in order to determine the old SFH and a possible rejuvenation through recent star formation. In the case of the outer ring, instead, JumpAge Old determines the time at which the first stars are formed, while JumpAge Young marks the time at which an increase (or decrease) of the star formation activity occurred and that level is kept until the time of the observation. We verified that, with the large flexibility allowed by these models, the assumption of an overall duration of the SFH of 10 Gyr has no impact on the results presented in the following sections.

MC-SPF includes a modelling of emission lines using line ratios from Byler et al. (2017) scaled to the Lyman continuum luminosity of the stellar templates and assuming the gas-phase metallicity measured from emission line ratios. We also included dust attenuation with a Calzetti (2001) law, where the flux from stars older than 10 Myr is attenuated

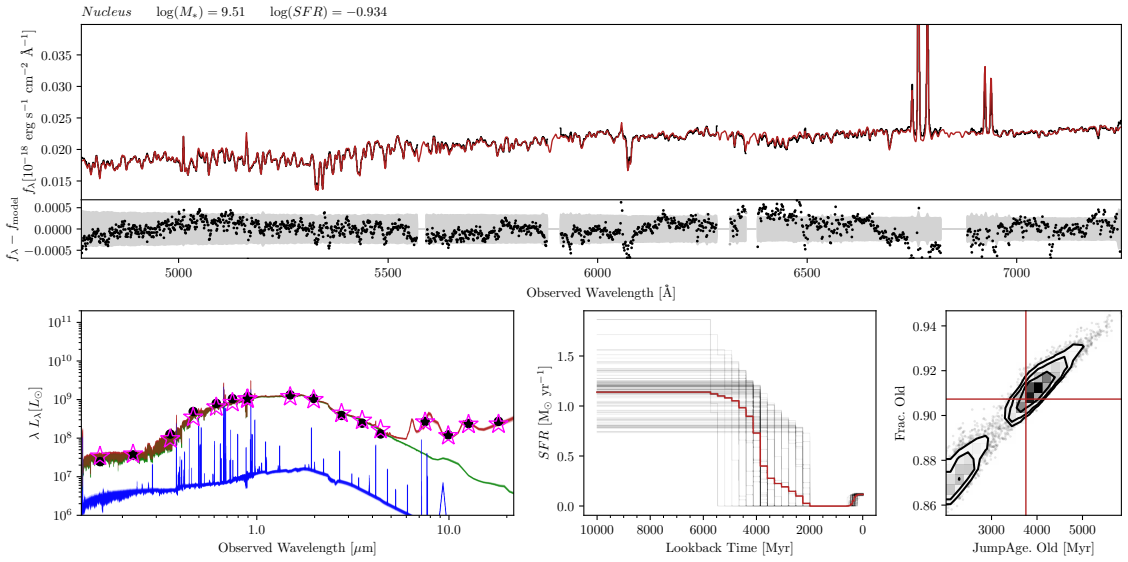

Figure 3.8: Results of the MC-SPF fitting for the nucleus region of the Cartwheel galaxy. Upper panel: MUSE spectrum (black) and best-fitting model (dark red). Spectral intervals dominated by bright skylines are not used in the fit. Fit residuals (Data-Model) are shown below the spectrum and the grey shaded area shows the 1σ uncertainties. Lower left panel: Photometric data points in black. The dark red lines are the total model including the dust emission, dominating at $\lambda > 5\mu$m, while the blue (green) lines show the contribution of the stellar continuum and nebular line emission from young (old) stellar populations (Age <> 30 Myr). The open magenta stars show the photometric datapoints from the best fit model. Different lines are 100 random samples of the posterior distribution. Lower middle panel: Reconstructed SFH from the fitting procedure. The dark red solid line is the median of the SFH samples. Lower right panel: Marginalised likelihood maps for the JumpAge Old and Frac. Old fit parameters. The red lines show the median value for each parameter, while the black contours show the 1, 2, and 3σ confidence intervals.

with a curve normalised by a free parameter (A_V) in the fitting procedure, while the same curve is normalised by $2.27 \times A_V$ for stars younger than 10 Myr. MC-SPF uses the MultiNest (Feroz & Hobson 2008; Feroz et al. 2009; Feroz et al. 2019) code to sample the posterior distribution and obtain the best-fitting parameters with reliable uncertainties in a Bayesian framework. Results obtained with the MC-SPF code will be discussed in detail in the next Section.

3.5 Results

As detailed in the previous sections, we extracted the spectra corresponding to the four spatial regions shown in Fig. 3.2 and we analysed them in their stellar and nebular components. We also derived the SFH for each region of the Cartwheel galaxy (see Chapter 3.4.4). In the following we present the results obtained. In particular, we discuss the ages of the stellar components derived for each separate region via the FIF technique in the framework of the SFH derived by means of the MC-SPF analysis, and we compare the stellar metallicities with the nebular ones.

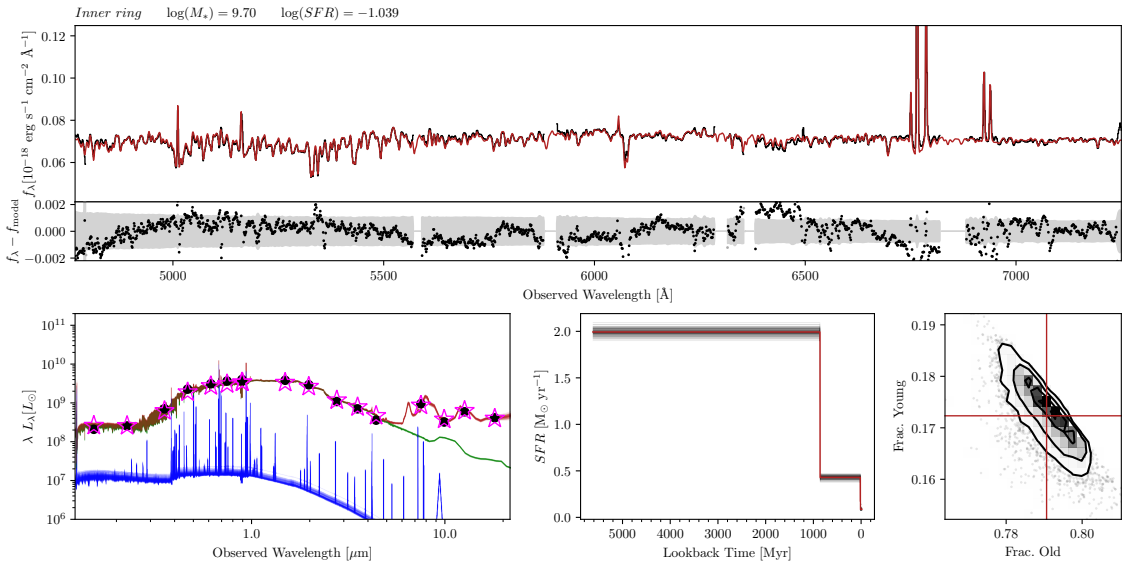

Figure 3.9: Same as Fig. 3.8 but for the inner ring of the Cartwheel galaxy. In this case, the lower right panel shows the marginalised likelihood maps for the Frac. Old and Frac. Young fit parameters.

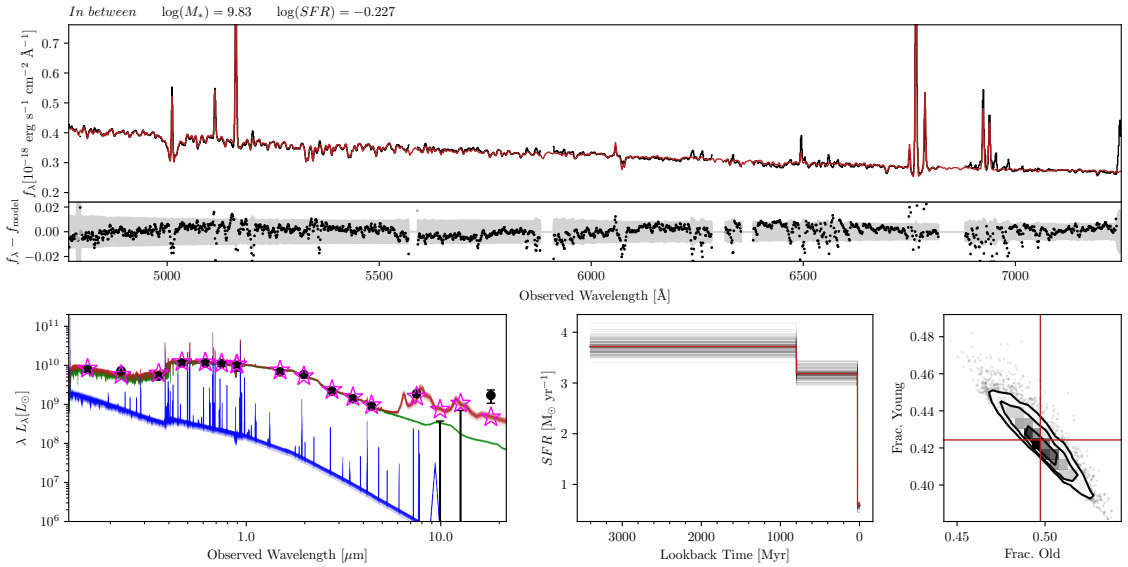

Figure 3.10: Same as Fig. 3.8 but for the in-between region of the Cartwheel galaxy. In this case, the lower right panel shows the marginalised likelihood maps for the Frac. Old and Frac. Young fit parameters.

3.5.1 Nucleus

As anticipated in Chap. 3.4.2 and 3.4.4, our analysis using the FIF approach did not reveal the presence of a density or shock wave induced (post-collisional) population. Therefore we adopted a single SSP model to obtain a mean value of stellar age and metallicity of the nucleus. We found that this region is dominated by a stellar component of ~ 3.2 Gyr with a slightly subsolar metallicity (see Table 4.2). The gas-phase metallicity estimate (i.e. 0.01 dex) is in broad agreement with that of the stellar component. The measured active SFR is compatible with zero, also given the fact that we cannot exclude a contribution from a weak AGN to the emission lines. Figure 3.8 shows the results obtained from the MC-SPF code for the nucleus. The derived SFH describe this region as mainly made during a star formation episode (modelled with a constant rate) that terminated ~ 3.7 Gyr ago, yielding about 91% of the region stellar content, as can be seen in the middle bottom panel of Figure 3.8, showing the posterior samples of the reconstructed SFH. In the same panel, the red line shows the average SFH which indicates an abrupt reduction in the star formation activity between 3 and 5 Gyr ago. The SFR has reduced below 50% of its original value ~ 4 Gyr ago, in excellent agreement with the analysis of the JumpAge Old parameter. Even in the MC-SPF analysis, the input models do not include AGN contributions, and therefore the emission lines can only be fit with a very young population of stars accounting for $\approx 9\%$ of the total mass. Given the possible presence of a weak AGN, this value should be taken as an upper limit, which turns into a lower limit for the older populations of stars.

3.5.2 Inner ring

Differently from the nucleus, in the inner ring we found a young component (i.e. ~ 0.8 Gyr) albeit in a very small fraction (i.e. 6%) of the total mass, over a precollisional population with age of ~ 5 Gyr. This is reflected on the slightly higher active star formation (i.e. 0.38 $M_\odot$ yr^{-1}) than the nucleus. Figure 3.9 shows the results obtained from the MC-SPF code for the this region. The SFH representation matches the results obtained from the stellar analysis, producing about 79% of the stellar content in a first 5 Gyr of activity, which terminated roughly 1 Gyr ago. We found a slightly super-solar stellar metallicity for the old component, which is consistent with the gas-phase one. Conversely, the metallicity of the young stellar SSP is estimated to be $\approx 15\%$ of the solar value. Taken at face value, this could imply a more recent star formation event from metal poor gas, possibly related to the galaxy collision. However, the small mass fraction of the young SSP combined with the posterior distributions shown in Figure 3.5 cannot rule out with high statistical significance that the younger stellar component is more metal enriched, reaching a significant fraction of the solar value.

3.5.3 In-between region

In the in-between region we found a more consistent young component (0.8 Gyr, similar to what found in the inner ring), characterised by a sub solar stellar metallicity, representing 16% of the total mass of the region. The gas-phase metallicity is measured as 67% of the solar value. Figure 3.10, showing the results obtained from the MC-SPF code for this region, confirms the higher active SFR measured by the nebular analysis and the detection of a recently induced star formation activity beside the precollisional component. The different relative fractions of the two components obtained in the FIF analysis (i.e, more than 70% of mass contained in the old component) with respect to those obtained in the MC-SPF (i.e. about 40% of mass contained in the young component) could be due to

the weakness of the FIF approach in reproducing the correct stellar mix on the basis of the simplified assumed SFH (two SSPs) and the spectral properties observed in a short wavelength range. Indeed, in the in-between the young component contains a relevant fraction of the total stellar mass (i.e. higher than $\sim$ 20%) and, given its young age, it dominates the stellar light emission, making it very hard to disentangle the properties of the two components on the basis of the estimates of few optical indices. In particular, on the basis of the stellar spectrum analysis, we obtain reliable measurements of the age and metallicity of the young component (i.e. the one dominating the optical emission), while those relative to the old one and their relative mass fraction are quite sensitive to the adopted SFH. The MC-SPF approach, due to its stronger assumption on the shape of the SFH and the larger wavelength coverage, is probably more reliable and successful in detecting both components and in deriving their characteristics. However, even if the overall picture is clear, only a physically motivated SFH from theoretical predictions on the origin of the old stars can ultimately shed light on the exact age and metallicity of the stellar populations in this region.

3.5.4 Outer ring

The outer ring emission is dominated by the most recent events, revealing a largely different picture with respect to that of the other regions. As already noted in Chap. 3.4.2, the analysis of the optical spectrum, which is dominated by the youngest luminous stars, cannot reveal the possible presence of the precollisional component. For this reason, we further simplified the SFH used to represent this region assuming a single SSP. From the analysis of the optical stellar spectrum, we found that the outer ring has a contribution from stars older than 30 Myr in addition to the current population powering the nebular ionisation. In particular, we found a noticeable scatter in the age of the nonionising population, ranging between 30 and 170 Myr in different subregions of the outer ring, with a mean age of 100 Myr and $0.1Z_{\odot}$ stellar metallicity. In all regions of the outer ring, the contribution of the ionising stars (Age $<$ 30 Myr) to the optical continuum is below 15%, providing indirect evidence of the inhomogeneity of this region. However, given the simplified SFH selected for this region in the FIF approach, we should be careful in interpreting this result. Indeed, a single SSP gives information about the light-weighted mean stellar population parameters that populate the considered region. In the particular case of the outer ring, the flux of the very young stars dominate the spectral region considered in the FIF approach, meaning that we should take this average range as a lower limit for the age of the oldest stars. Regarding the metallicity estimate, the measured value of about 10% of the solar value has to be considered, like the age, a lower limit given that the gas-phase metallicity is about $0.4Z_{\odot}$.

A complementary tool for understanding the stellar content of the outer ring is the use of the MC-SPF approach, which takes advantage of a larger wavelength baseline thanks to the joint fit of the photometry and the spectrum and to the more flexible SFHs. As explained in Chap. 3.4.4, differently from the other regions, in the outer ring we used a piece-wise constant SFH in two age bins, fitting a SFH model with three free parameters: the relative fraction of the two components, the lookback time for the onset of the SF creating the oldest stars, and the lookback time at which the star formation level has jumped from the old to the young component. We stress that, despite its simplicity, we chose this SFH to allow for a great degree of flexibility, in order to capture possible sudden variations in the SF activity that can be expected from the current starbusty activity of the outer ring. Figure 3.11 shows the results obtained with this code in the outer ring. We found that this region is largely dominated by young stars ($>$ 85% of the mass) formed in a

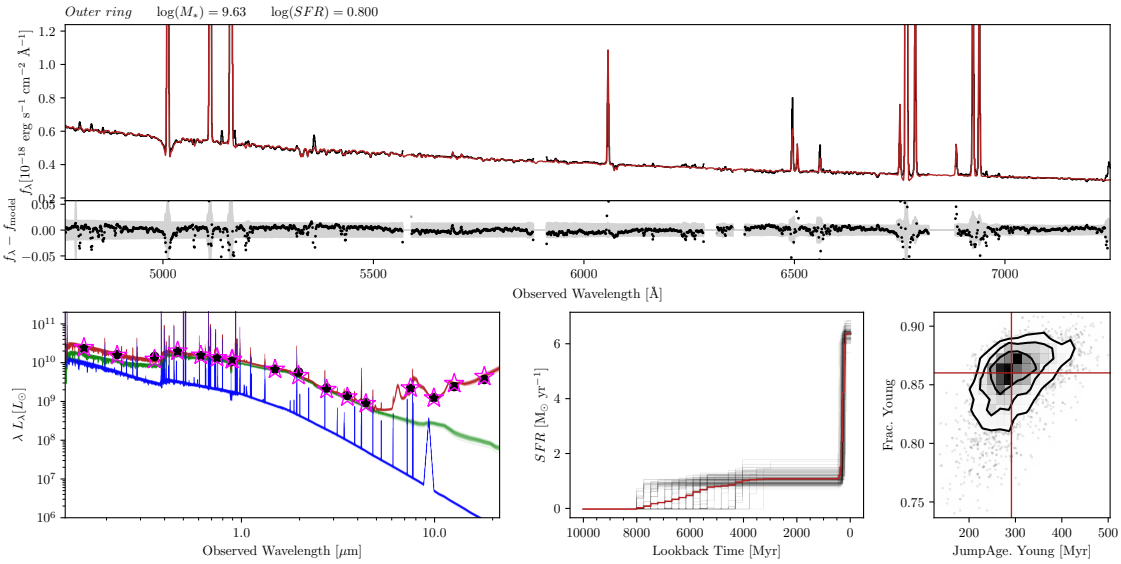

Figure 3.11: Same as Fig. 3.8 but for the outer ring of the Cartwheel galaxy. In this case the lower right panel shows the marginalised likelihood maps for the JumpAge Young and Frac. Young fit parameters.

recent star formation event that, in our parametrisation, started around 300 Myr ago. We also found a small ($< 15\%$) fraction of a precollisional stellar component in this region of the galaxy. This component includes stars as old as 8 Gyr, although the posterior samples shown in the SFH panel in Figure 3.11 indicate that the data can be reproduced also with stars not older than 4 Gyr. As a result, there is a decreasing probability that stars older than 4 Gyr are required by the model, possibly also due to the difficulty in detecting a small fraction of such old stars embedded in a dominant young population.

3.6 Discussion

The study of the stellar content in four regions of the Cartwheel galaxy at increasing radial distance from the centre allows us to define a possible framework to describe the recent evolution of this galaxy. We inferred a precollisional component with a mean age between 3 and 8 Gyr over all the galaxy with the only exception of the outer ring, which is dominated by stars formed in a starburst that started roughly 300 Myr ago and is still ongoing. Even in the inner ring, which supposedly formed as a consequence of the impact suffered by the Cartwheel galaxy, we found that more than 90% of the total mass is part of the precollisional component (i.e. with an age of about $5 - 6$ Gyr), with the same gas-phase metallicity of the nucleus, suggesting that it belongs to the original galaxy. The slight increase in the star formation activity (see Table 3.3) we detected in the inner ring with respect to the nucleus (confirmed also by the MC-SPF analysis, see Fig 3.8 and 3.9) well matches the expected SFR profile of a spiral galaxy of $\log(M_*/\mathrm{M}_\odot) = 10.7$ (Zaragoza-Cardiel et al. 2022) and it corresponds to a slight decrease of the gas-phase metallicity, as expected by the fundamental metallicity relation (FMR, Mannucci et al. 2010). The same trend is confirmed in the in-between region, where the SFR is more significant and the gas-phase metallicity 0.18 dex lower than in the nucleus. Considering an average distance of the in-between region from the nucleus of about 10 kpc, we derive a gas-phase metallicity gradient of 0.018 dex/kpc, in perfect agreement with the gradient found by Zaragoza-

Cardiel et al. (2022) derived from the analysis of individual HII regions identified from the nucleus towards the external ring. In Zaragoza-Cardiel et al. (2022), the areas 4-5-6 in their Figure 11 and 12 correspond to our in-between region, and their estimate of the corresponding gas-phase metallicity is around 65% of the solar value, well matching our estimate (see Table 3.3). We found a good agreement also for the metallicity estimated in both the nucleus and the inner ring, where we measured a value around the solar one to be compared with an estimate of 80% of the solar value derived from Zaragoza-Cardiel et al. (2022).

Considering the age of the stellar content, the main stellar component populating the innermost region of the Cartwheel galaxy up to the limit of the outer ring appears to be almost coeval (within 1σ error), with little to no sign of very recent activity. A possible very young component formed in the last hundreds of Myrs due to the recent impact is almost totally absent in the nucleus and inner ring while it represents only about 20% of the total mass in the in-between region. All these elements taken together suggest that, apart from the peculiar morphology, a large fraction of the stars in the Cartwheel galaxy are not affected by the recent impact with the companion bullet and the galaxy keeps the characteristics of a typical spiral galaxy in terms of age, metallicity and SFR distributions.

Differently from the other regions, in the outer ring we found mostly young stars (i.e. with ages < 400 Myr). The estimated gas-phase metallicity in the outer ring considering all the flux coming from this region is 0.19 dex lower than the value obtained in the in-between region, which is about 12 kpc apart; this is consistent with the previously calculated gradient. This result is at odds with what Zaragoza-Cardiel et al. (2022) report for the gas-phase metallicities of the individual HII regions identified in the ring, which are lower than expected from the extrapolation of the inner gradient. Indeed, the mean gas-phase metallicity we measure in the outer ring is $\approx 45\%$ of the solar value, while the estimate obtained by Zaragoza-Cardiel et al. (2022) in the external ring HII regions is around 20% of the solar value. The difference between the results obtained in the two works can be due to the different analysis we performed, that averages over all the emitting outer ring area rather than being weighted towards the HII regions. To test this hypothesis, we derived the gas-phase metallicity from the spectrum extracted by summing fluxes corresponding to the HII regions in the outer ring spectrum as defined by Zaragoza-Cardiel et al. (2022). Indeed, we found that the HII regions selected by Zaragoza-Cardiel et al. (2022) in the external ring of the Cartwheel galaxy are less metal rich than the average gas contained in the outer ring, being the former less than 40% of the solar value, i.e. 0.1 dex lower than in the outer ring excluding the strong HII regions (see Table 3.3). This result supports the idea outlined by Zaragoza-Cardiel et al. (2022) that the infall of metal poor gas from the intergalactic medium triggers strong star formation activity while diluting the metallicity of the existing gas that is still detectable outside the stronger HII regions. It is worthy to note that the metallicity calibration curves adopted by Zaragoza-Cardiel et al. (2022) (i.e. Pilyugin & Grebel 2016) tend to give lower estimates than those we adopted (i.e. Curti et al. 2017) in particular in the lower metallicity regimes, increasing the discrepancy between our results and those by Zaragoza-Cardiel et al. (2022).

On the other hand, the presence of such a high fraction of very young stars in the outer ring suggests that this is the only region dominated by very recent and ongoing star formation events triggered by the impact with the bullet companion galaxy. Mayya et al. (2024), on the basis of Astrosat/UVIT and FUV imaging data, found evidence of a wide range of ages in the ring but still younger than 150 Myr, suggesting a SFH that can be described by an average steady SFR of ≈ 5 $M_\odot$ yr^{-1} over the past 150 Myr, with a possible, but less statistically significant, increase to ≈ 18 $M_\odot$ yr^{-1} in the last 10 Myr.

Our results for the outer ring support the picture that it formed stars at an elevated rate in the recent past, with the onset of the recent starburst around 300 Myr ago, and with an average rate of about 6.3 $M_\odot$ yr^{-1}. Our estimate of the SFR in the full *Outer ring* region, obtained from nebular emission lines, gives 9.25 $M_\odot$ yr^{-1}, in good agreement with the range of estimates by Mayya et al. (2024). Regarding the recent history of this region, our result implies the possibility that the actual external ring contains stars formed during the expansion of the collision wave, and that the starting time of the wave propagation happened about 300 Myr ago, while the study of Mayya et al. (2024), taking into account the brighter HII regions in the external ring only, finds a more recent value for the starting time of the wave propagation, i.e. around 150 Myr. Nevertheless our estimates of the parameter $D = (L_{\rm young} + L_{\rm old})/L_{\rm young}) = 6.67$, as first introduced in (Mayya et al. 2024, see their Figure 7), and the EW(Hα)= 190 Å are in close agreement with the results obtained in the individual HII regions by Mayya et al. (2024), providing further support to our modelling framework. Our result well matches that of Higdon (1996), who investigated the distribution and kinematics of the neutral hydrogen content in the Cartwheel galaxy. On the basis of the HI velocity field analysis, and assuming a constant expansion rate, they found that the impact took place around 300 Myr ago. Our result is also consistent with the Amram et al. (1998) work. Using the Hα emission map obtained with a scanning Fabry–Perot interferometer, they dated the impact in the range from 210 to 720 Myr ago.

Apart from details on the timescale of the star formation events, we support the same picture presented in Mayya et al. (2024) and Zaragoza-Cardiel et al. (2022), suggesting that the collision wave, while moving towards the actual position, drags the already formed stars sweeping the inner areas, as predicted by the recent collision model by Renaud et al. (2018). Conversely, we describe the external ring as produced by a collision wave started not earlier than 400 Myr ago, while Renaud et al. (2018) predict a shorter lived ring lasting less than 200 Myr. Furthermore, according to Renaud et al. (2018) the ring should start to lose material during its expansion, material that is predicted to gravitationally fall back towards the nucleus within what we call the in-between region, triggering fresh star forming events. Our results derived from the analysis of the nucleus, inner ring and in-between regions do not appear to support this picture (at least over the predicted short timescales) because we found that all the stellar populations in the Cartwheel galaxy follow the distribution expected in a disc galaxy, with the unique exception of the external ring.

3.7 Summary and conclusions

We presented a novel analysis of the stellar population properties of the entire Cartwheel galaxy. Our study is based on the publicly available high-spatial-resolution spectroscopic data obtained with the MUSE instrument during the Science Verification observations. Photometric imaging covering the wavelength interval from the FUV to the IR region, including the recently available JWST/NIRCam and JWST/MIRI data, complement the analysed data set. We divided the galaxy into four separate spatial regions, namely the 'nucleus', the 'inner ring', the 'in-between region' and the 'outer ring'. Given the large spatial dimensions of the selected regions (with the exception of the nucleus), we further divided each one into equally extended subregions in order to perform a spatially resolved analysis of the entire galaxy. For each of the four regions, we then derived the main physical parameters of their stellar content. We followed a two-step approach: First, (i) we compared four spectral indices sensitive to age and metallicity of the stellar populations (i.e. Hβ, Mgb, Fe5270, and Fe5335) with model predictions, and then (ii) we performed a

full spectral fitting of the whole MUSE spectra combined with all the available photometric information to derive the SFH of each region.

In the first step, we adopted the FIF procedure, which takes into account not only the strength of the absorption features but also their shape. Furthermore, we assumed that each region can be described by the combination of the precollisional population of the original galaxy with a recently formed population as a consequence of the impact with the bullet companion.

In the second step, to extract the SFH of each defined region of the galaxy, we also jointly fitted the photometric and spectroscopic data using the MC-SPF code, updated with new features and SFHs tailored to this specific study. Our findings can be summarised as follows:

- We find a dominant old component with a mean age of between 3 and 8 Gyr over all the galaxy with the only exception being the outer ring, which is entirely dominated by stars formed no earlier than 400 Myr ago. Light from these nonionising stars dominates the observed optical continuum flux in the outer ring in spite of the extremely bright nebular lines.

- Apart from the peculiar morphology, a large fraction of the Cartwheel galaxy (from the nucleus to the in-between region) is not affected by the recent impact with the companion bullet and retains the characteristics of a typical spiral galaxy in terms of age, metallicity, and SFR distributions.

- Our analysis suggests a picture in which the collision shock wave, while moving towards the outer ring, sweeping the inner areas and dragging the already formed stars along with it, as predicted by the recent collision model by Renaud et al. (2018), albeit on longer timescales.

- The lack of very young stars in the inner ring and in-between region does not match the Struck et al. (1996) and Renaud et al. (2018) predictions of star forming material falling back towards the nucleus along the spokes.

Our work demonstrates that the study of stellar population distributions, coupled with a nebular analysis, can provide information about the recent collision suffered by the Cartwheel galaxy. Our results show how optical spectroscopy and multi-wavelength photometry can precisely reconstruct the history of complex objects like RiGs.

In this Chapter we validated our code and methodology on a single and peculiar target. We now move from this, interaction-dominated case to a statistical sample of galaxies. We generalise the approaches explored with the Cartwheel galaxy to the COSMOS Wall galaxies at $z \sim 0.73$ (Scoville et al. 2007), leveraging both spectroscopic and photometric data to trace their stellar populations and constrain their formation and quenching timescales across environments. In particular, we carry forward the index selection criteria and Bayesian approaches developed in chapters 2 and 3, to perform a joint FIF+photometry analysis with nested sampling and population-level hierarchical modeling to robustly derive ages, metallicities and star-formation timescales at fixed mass and environment.

Chapter 4

The COSMOS Wall at $z \sim 0.73$: quiescent galaxies and their evolution in different environments

This Chapter is based on Ditrani et al. 2025, A&A, 696, A116.

From Chapters 2 and 3, we now have a validated toolkit to measure the main physical properties of the galaxy stellar populations. Having demonstrated its performance and capabilities on controlled simulations and on spatially resolved regions of galaxies with extreme star-formation conditions, in this chapter we scale up to a statistical sample of observed galaxies. We focus on quiescent galaxies, i.e. systems that have not formed stars for a long time and are therefore easier to model than star-forming galaxies with complex star-formation histories. Their stellar content can be approximated as nearly coeval, since most of their stars were formed in a single, short burst (or in a few episodes) (e.g. Renzini 2006, and references therein). Tracing their stellar ages, metallicities, and formation timescales we can derive their quenching mechanisms across different environments. As discussed in Chap. 1.3, both mass and environmental quenching contribute to the suppression of star formation and their relative significance varies depending on the galaxy mass and the cosmic epoch. Moreover, the effects of these various quenching processes on galaxy properties are often degenerate, making it challenging to distinguish their individual contributions.

Stellar population properties of quiescent galaxies have been known to vary strongly with the environment in which galaxies are located (Spitzer & Baade 1951; Oemler 1974; Davis & Geller 1976; Dressler 1980). In dense environments and massive haloes, the evolution from star-forming galaxies to quiescent ones takes place sooner than in the field (Cooper et al. 2006; Cucciati et al. 2006; Poggianti et al. 2006; Iovino et al. 2010; Peng et al. 2010). However, whether this environmental signal is merely the result of different galaxy masses in different environments (i.e. the mass segregation framework) or reflects intrinsic differences in stellar history at fixed mass is still debated (e.g. Baldry et al. 2006; Thomas et al. 2010; Poggianti et al. 2013). Studies on the effect of the environment are mainly performed in the context of the local Universe. In particular, the stellar ages and metallicities of quiescent galaxies have been shown to correlate to first order with galaxy mass (e.g. Gallazzi et al. 2005; Thomas et al. 2005; Thomas et al. 2010), with environment

playing a larger role in less massive galaxies (e.g. Thomas et al. 2010; Gallazzi et al. 2021). Some studies have been able to determine the role of the environment in quiescent galaxies and found older galaxies in the most massive environments with respect to the field (Sánchez-Blázquez et al. 2006).

In this framework, a unique opportunity to investigate the effects of the environment on galaxy quenching and evolution is a study of a sample of massive quiescent galaxies in a large filamentary structure at $z \sim 0.73$, named the COSMOS Wall (Scoville et al. 2007; Iovino et al. 2016). This structure covers a comprehensive range of environments, ranging from a dense cluster to filaments and voids. Moreover, the COSMOS Wall redshift, corresponding to roughly half the age of the Universe (~ 6.5 Gyr), marks a transitional period when the Universe's star formation rate (SFR) was declining and environmental effects began to play a dominant role in shaping galaxy properties (Fossati et al. 2017).

In this work we then present an analysis of the stellar populations of quiescent galaxies in this peculiar field to study the role of environment in quenching the star formation activity in massive galaxies. We leverage high-quality spectroscopic data from The Large Early Galaxy Astrophysics Census (LEGA-C) Public Spectroscopic Survey (van der Wel et al. 2016; Straatman et al. 2018; van der Wel et al. 2021), combined with the extensive photometric coverage of the COSMOS2020 catalogue (Weaver et al. 2022) to perform a novel joint full-index and photometric fitting. At the population level, we employ a hierarchical Bayesian modeling to quantify intrinsic scatter and environmental dependencies at fixed mass and redshift. With this work we provide precise stellar population measurements to translate them into constraints on their formation and quenching histories.

4.1 Data and sample selection

The COSMOS Wall is a volume identified within the COSMOS survey that contains a large variety of environments, from rich and dense clusters (with X-ray detection) to poor and loose groups, down to average field regions. This volume is at redshift $0.69 \leq z \leq 0.79$, located in the RA-Dec region displayed in Fig. 1 of Iovino et al. (2016). Readers are referred to Iovino et al. (2016) for more details on this structure's definition. Iovino et al. (2016) performed a detailed mapping of the COSMOS Wall volume using a friends-of-friends algorithm and an iterative procedure to obtain a reliable group catalogue at different spatial scales. The valuable aspect of this structure consists in the opportunity it offers to study the possible differences in the physical properties of galaxies in relation to their environment, at a fixed cosmic epoch.

The COSMOS field has been targeted by several spectroscopic surveys (e.g. Lilly et al. 2007; Coil et al. 2011; Comparat et al. 2015), and among them the LEGA-C survey (van der Wel et al. 2016) provided high signal to noise ratio and high resolution spectra of the more massive galaxies in this area. Indeed the spectra, observed with the Visible Multi-Object Spectrograph (VIMOS) on the Very Large Telescope (VLT), have an average continuum $S/N \sim 20$ Å^{-1}, with an instrumental spectral resolution ($R \sim 3500$) suitable to study the stellar population properties of galaxies (DR3; van der Wel et al. 2021). In this work we studied the physical properties of a sample of massive quiescent galaxies within the COSMOS Wall volume by combining optical LEGA-C spectra and a set of photometric data covering a large wavelength range. For the photometric data, we used the multi-wavelength photometric COSMOS2020 catalogue (Weaver et al. 2022). In particular, we used the smallest photometric aperture magnitudes available (2 arcsec) measured in u^* band from the MegaCam/CFHT images, in the HSC-SSP PDR2 g-, r-, i- ,z- and y-band images and in the UltraVISTA DR4 J-, H- and K_s-band Weaver et al. (2022), in order to

match the 1 arcsec slit aperture of the LEGA-C observations (van der Wel et al. 2021).

From the entire LEGA-C sample, we selected galaxies that are in the COSMOS Wall volume as defined above, identifying a total of 244 objects. We measured the available star formation indicators ([OII]$_{\lambda3727}$, Hδ, Hβ, [OIII]$_{\lambda5007}$) using the latest version of the penalised pixel-fitting (pPXF) code (Cappellari & Emsellem 2004; Cappellari 2017, 2023), adopting the E-MILES simple stellar population (SSP) synthesis models (Vazdekis et al. 2016), obtained assuming the BaSTI tracks (Pietrinferni et al. 2004, 2006) and Chabrier (2003) initial mass function (IMF). We then spectroscopically selected a subsample of quiescent galaxy candidates using the following criteria:

- EW([OIII]$_{\lambda5007}$) < 1 Å;
- EW(Hβ) < 1 Å;
- EW([OII]$_{\lambda3727}$) < 5 Å;
- EW(Hδ) < 3 Å in absorption.

These criteria are designed to select galaxies with no detectable [OIII]$_{\lambda5007}$ and Hβ emission lines and at most a weak [OII]$_{\lambda3727}$ emission, which can occur in quiescent galaxies at these redshifts (see Maseda et al. 2021). Additionally, the last criterion, EW(Hδ) < 3 Å in absorption, excludes post-starburst galaxies from our sample, following the definition of Poggianti et al. (2009). Using the above selection criteria, we defined a sample of 99 quiescent galaxies. However, due to the limited and variable rest-frame spectral range, approximately half of the selected sample lacks at least one of the indicators required for this selection. Specifically, among the 99 selected galaxies, 19 have spectra not including the [OII] line, 14 galaxies lack both [OIII] and Hβ, and 9 ones lack only the [OIII]. For these galaxies, we based the selection on the other available indicators. We tested the possible contamination introduced by using a reduced set of criteria using the subsample of 109 out of 244 galaxies for which all the four indicators are available. For example, we performed the selection without considering the [OII] line and then checked the values of [OII] for the selected galaxies. We found that some galaxies would not meet the selection criteria if the [OII] threshold of 5Å had been applied. This analysis revealed that, in the worst-case scenario, only 5 out of the 99 galaxies in the sample might not satisfy all the selection criteria when the full set of indicators is considered.

Figure 4.1 shows the rest-frame UVJ diagram of the 244 galaxies observed in the COSMOS Wall volume by the LEGA-C survey (grey points) and our selected quiescent sample (red points). Rest-frame $U - V$ and $V - J$ values are obtained from the LEGA-C photometric parent sample Muzzin et al. (2013a). The entire sample of selected galaxies falls within the region of the UVJ diagram associated with quiescent galaxies, as defined by Williams et al. (2009). Specifically, they occupy the region corresponding to older quiescent galaxies, as defined from Whitaker et al. (2013), further supporting the robustness of our selection. We also inspected the spectra of those galaxies that have colours matching those of the quiescent galaxies in the UVJ plane but that were excluded by our spectroscopic selection. We found that their spectra clearly exhibit gas-phase emission lines in those galaxies. Therefore, we consider the spectroscopic criteria we adopted for selecting quiescent galaxies to be solid and trustworthy.

Iovino et al. (2016) classified galaxies in the COSMOS Wall volume as belonging to groups or as field galaxies. Furthermore, by cross-correlating their group catalogue with the list of XMM-COSMOS extended sources presented in George et al. (2011) (down to a limit X-ray detection from of rest-frame $\log(L_{X,0.1-2.4keV}/ergs^{-1}) \sim 41.3$, corresponding to $\log(M_{200}/M_{\odot}) > 13.2$), they further categorised the groups into X-ray emitters

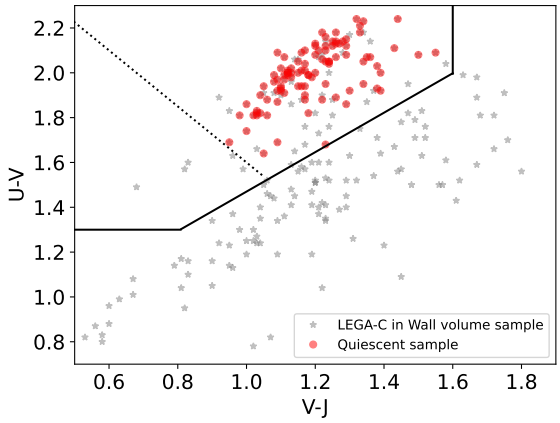

Figure 4.1: Rest-frame UVJ diagram of the selected sample. The stars are all the galaxies observed in the COSMOS Wall volume by the LEGA-C survey, while the red points mark the spectroscopically selected quiescent galaxies. The solid black line is the separation between star-forming and quiescent galaxies as defined in Eq. 4 of Williams et al. (2009). The dotted line divides younger quiescent galaxies (on the left) and older quiescent galaxies (on the right) according to Whitaker et al. (2013).

or non-X-ray emitters. This matching process identified nine groups in the Wall Volume with X-ray detection. Notably, the new X-ray group catalogue for the COSMOS field, derived by Gozaliasl et al. (2019), using combined Chandra and XMM-Newton observations from the COSMOS Legacy Survey, does not alter the list of matched groups originally presented by Iovino et al. (2016). Our sample galaxies can then be divided into three different environment bins: groups with X-ray detection, groups without X-ray detection, and field. Specifically, our sample consists of 22 galaxies located in groups with X-ray detection (hereafter X-ray groups), 28 in groups without X-ray detection (hereafter non-X-ray groups), and 49 in the field.

Figure 4.2 shows the stellar mass distribution of the galaxies across the three environment bins. We used stellar masses estimated from Muzzin et al. (2013a). It is well known that galaxy evolution strongly depends on their stellar mass (e.g. Thomas et al. 2010), and to isolate the effect of environment, we need to compare samples with the same mass distribution across the three environments. According to van der Wel et al. (2021), the LEGA-C sample in the redshift bin between 0.7 and 0.8 is representative down to a stellar mass limit of $\log M_*/\mathrm{M}_\odot = 10.47$. Therefore, we refined our sample selection by restricting it to galaxies within the mass range $10.47 < \log M_*/\mathrm{M}_\odot < 11.4$, since we used the same measurements from Muzzin et al. (2013a). The upper limit was set to exclude the more massive galaxy tail, which is present only in the X-ray group environment. We performed a K-S test for the three distribution in the restricted mass bin, and we obtained a p-value of 0.2 between X-ray and non-X-ray groups, a p-value of 0.4 between X-ray groups and field, and a p-value of 0.5 between non-X-ray groups and field. From the K-S test we did not detect significant differences between the three population and therefore we assumed that the distributions are extracted from the same parent population. Our final sample consists then of 16 galaxies located in X-ray groups, 22 in non-X-ray groups, and 36 in the field, for a total of 74 quiescent galaxies.

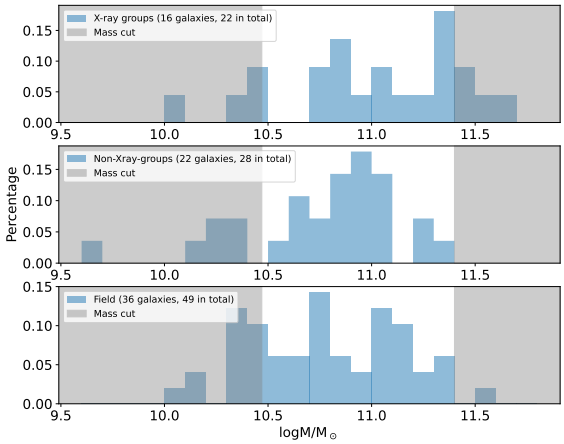

Figure 4.2: Mass distribution in the three environment bins. The shaded grey region is the mass cut we applied to obtain a homogeneous and representative distribution across the three bins.

4.2 Analysis

Our goal is to measure the individual mass-weighted age, the stellar metallicity and the star formation timescale of our sample of quiescent galaxies, and then investigate the effects of the environment on their properties. In this section we describe in detail the steps of the analysis on our sample. Specifically, in Chap. 4.2.1 we introduce the synthetic templates built to analyse the selected galaxies. In Chap. 4.2.2 we describe the performed joint fitting of spectra and photometry using Monte Carlo techniques, given the multi-wavelength available data (Chap. 4.2.2). Finally, we present how we assess the stellar population parameters of each environment bin using the hierarchical Bayesian modelling (Chap. 4.2.3).

4.2.1 Stellar population models

We built a set of synthetic templates based on the SSP models from the latest version of the Bruzual & Charlot (2003) library (hereafter the C&B library; see Plat et al. 2019; Sánchez et al. 2022). The SSP models adopt the PARSEC evolutionary tracks (Marigo et al. 2013; Chen et al. 2015). We assumed a Chabrier IMF (Chabrier 2003) with $M_{UP} = 100 M_{\odot}$ and the MILES stellar library ($3540.5 < \lambda < 7350.2$ Å; Sánchez-Blázquez et al. 2006; Falcón-Barroso et al. 2011, 2.5Å full width at half maximum resolution). The C&B library provides 3300 SSPs unevenly spaced in linear age and [Z/H], covering 220 ages from 0.01 Myr to 14 Gyr and 15 metallicities from [Z/H] $= -2.23$ to [Z/H] $= 0.55$ dex; for reference, the solar abundance ($Z_{\odot}$) is 0.017. From the C&B library we generated composite stellar population templates characterised by a fast rise of star formation, typical of massive quiescent galaxies (e.g. Citro et al. 2016), followed by an exponentially declining star formation history (SFH):

$$SFR_{\tau}(t) \sim \sqrt{\left(\frac{t}{\tau}\right)} \exp\left(-\frac{t}{\tau}\right), \tag{4.1}$$

where τ represents the SFR timescale of the SFH, varying between $0.1 \leq \tau \leq 2$ Gyr, in increments of 0.1 Gyr. At $t = 2\tau$ the SFR has declined to approximately 30% of its peak value and formed about 75% of the total stellar mass. Finally, we adopted the attenuation

law from Calzetti (2001) with $0 \leq A_V \leq 1$ mag. Given the age of the Universe at the redshift of the COSMOS Wall (~ 7 Gyr), we set the maximum age of the templates to 8 Gyr.

4.2.2 Joint spectroscopic and photometric analysis

In our analysis, we combined spectroscopic and photometric data to derive the stellar population parameters of the selected galaxies through comparisons with the spectral template library described in the previous subsection. For each galaxy in the sample, we determined the kinematic parameters (i.e. recession velocity and velocity dispersion) using the latest version of the pPXF code, adopting the template set from the MILES stellar spectral library (Sánchez-Blázquez et al. 2006), convolved to match the LEGA-C instrumental resolution, and considering the rest-frame wavelength range between 3540 Å and 4700 Å. Synthetic templates were then shifted to match the recession velocity of each galaxy and convolved with the estimated stellar velocity dispersion. Our fit of the velocity dispersion are consistent within 10 km/s with the available values from van der Wel et al. (2021).

We then adopted the full-index fitting (FIF) approach (Martín-Navarro et al. 2014) to compare the observed spectra with the synthetic spectral templates. Differently from the more classic index fitting approach, FIF compares the flux within a specific absorption feature (with respect to its continuum value) pixel by pixel rather than averaging it. This pixel-level comparison within the index window is more effective at breaking the degeneracy between age and metallicity compared to the classical index analysis, as it accounts not only for the strength of the absorption feature but also for its detailed shape, which provides additional information about the stellar population parameters. (Martín-Navarro et al. 2019; Ditrani et al. 2024). We applied the FIF method to a comprehensive set of spectral indices, namely: Fe3581, Fe3619, Fe3741, $\mathrm{D_n}4000$, FeBand4050, $\mathrm{H}\delta_F$, $\mathrm{H}\gamma_F$, $\mathrm{G}_{band}4300$, Fe4383, and Fe4531 (Gregg 1994; Balogh et al. 1999; Worthey et al. 1994). Given the available wavelength range, we used only Fe indicators to determine the stellar metallicity, meaning that the derived total metallicity is a proxy of the [Fe/H] abundance. Figure 4.3 shows an example of the FIF approach applied to one of the selected galaxies. The best-fit template closely matches each spectral feature, capturing detailed information from both their depth and pixel-by-pixel shape.

The only exception to the FIF approach concerns the $\mathrm{D_n}4000$ index. For this index, we adopted the classic index definition, and its value was compared with the corresponding values measured in the synthetic templates.

Regarding the photometric data, we compared the observed fluxes in the 9 bands described in Chap. 4.1 with those measured in the same photometric bands on the synthetic spectral templates. For this comparison, we first normalised the synthetic templates using the observed i-band flux corresponding to the wavelength range of the LEGA-C observed spectrum. Additionally, we fitted three 'jitter' parameters: $\ln f_{uv}$ for the u^* band, $\ln f_{opt}$ for g-, r-, i- ,z- and y-band and $\ln f_{ir}$ for J-, H- and K_s-band. These parameters act as multiplicative factors applied to the photometric uncertainties in order to balance the likelihoods between the spectroscopic and the photometric fits, given that the S/N of the photometric data significantly exceeds that of the spectroscopic data.

Therefore, we computed the total posterior probability distribution using the likelihood given by $\mathcal{L} = e^{-\chi^2/2}$, with

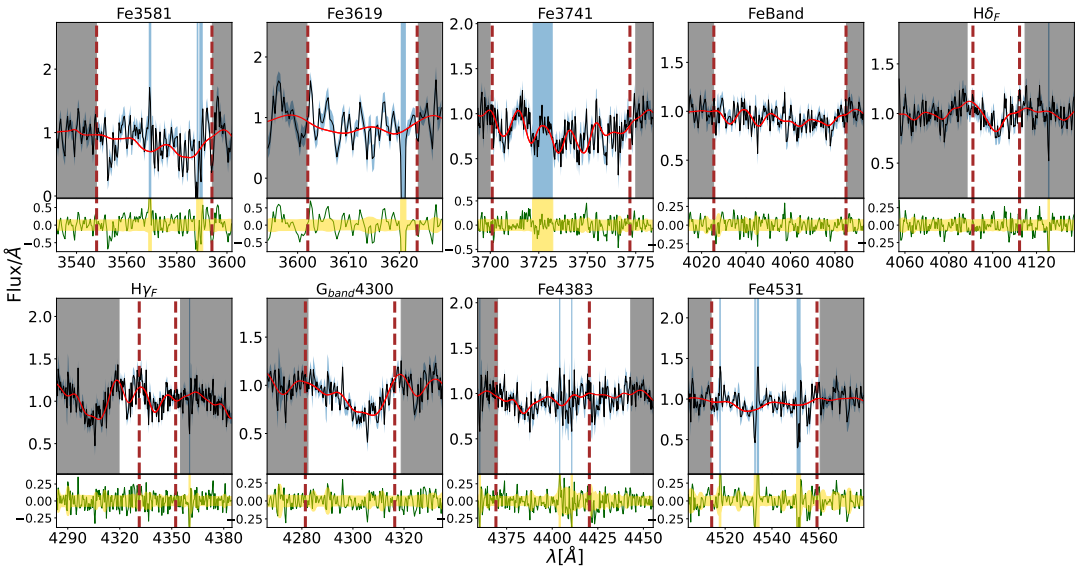

Figure 4.3: FIF application to the indices available in the LEGA-C ID 209466 galaxy spectrum. The vertical dashed brown lines indicate the feature boundaries for each index, while the grey shaded regions represent the pseudo-continua used for normalisation. In the upper subplots, the black lines and blue shaded regions correspond to the observed spectrum and its associated uncertainty, respectively. The solid red line represents the best-fit derived from the posterior distribution. The green lines in the lower subplots show the residuals between the observed spectrum and the best fit, with the yellow shaded region indicating the relative uncertainties of the observed spectrum.

$$\chi^2 = \sum_i \left(\frac{F_{obs_i} - F_{syn_i}}{\sigma_{obs_i}} \right)^2 + \left(\frac{D_{\rm n}4000_{obs} - D_{\rm n}4000_{syn}}{\sigma_{D_{\rm n}4000_{obs}}} \right)^2 + \\ + \sum_i \left(\frac{Phot_{obs_i} - Phot_{syn_i}}{\ln f_x * \sigma_{Phot_{obs_i}}} \right)^2, \tag{4.2}$$

where the first term is the contribution of the comparison using the FIF approach, F_{syn_i} is the flux of the synthetic spectrum along the feature of each index, and F_{obs_i} is the flux of the observed spectrum with the error σ_{obs_i}. The second term is the contribution of the D_n4000 comparison, where $\mathrm{D_n}4000_{syn}$ is the index measurement on the synthetic template, and $\mathrm{D_n}4000_{obs}$ is the index measurement on the observed spectrum with the error $\sigma_{D_{\rm n}4000_{obs}}$. Finally, the last term is the contribution of the comparison with the photometric data, where Phot_{syn_i} is the photometric flux in the i-th band of the synthetic spectrum, and Phot_{obs_i} is the photometric flux in the i-th band of the observed galaxy with the error $\sigma_{Phot_{obs_i}}$. The photometric error is multiplied by $\ln f_x$, where x can be *uv*, *opt*, or *ir* as described above. We derived posterior probability distributions and the Bayesian evidence using the nested sampling Monte Carlo algorithm MLFriends (Buchner 2016, 2019) using the UltraNest[1] package (Buchner 2021). We assumed uniform prior for all the parameters considered, summarised in Table 4.1. Figure 4.4 shows an example of the joint and marginal probability distributions for all the fitted parameters, while Fig. 4.5 shows the best-fit applied to both the entire LEGA-C spectrum and the photometric data

[1] `https://johannesbuchner.github.io/UltraNest/`

Table 4.1: The seven free parameters fitted to our spectroscopic and photometric data, along with their associated prior distributions.

Parameter	Unit	Range	Prior
$\mathrm{Age_{model}}$	Gyr	(0, 8)	Uniform
[Z/H]	dex	(-2.23, 0.55)	Uniform
τ	Gyr	(0.1, 2)	Uniform
A_V	mag	(0, 1)	Uniform
$\ln f_{uv}$	dex	(-2, 10)	Uniform
$\ln f_{opt}$	dex	(-2, 10)	Uniform
$\ln f_{ir}$	dex	(-2, 10)	Uniform

for a representative quiescent galaxy (LEGA-C ID = 209466). It is evident that our fit provides reasonable fits for both the spectrum and the photometric data of the galaxy.

4.2.3 Hierarchical Bayesian modelling

To assess the stellar population parameters in each environment bin, we combined the obtained results for each individual galaxy using the hierarchical Bayesian modelling. In the hierarchical framework, our models consist of two levels: the first level involves the measurements of the parameters for each individual galaxy, while the second level describes how the measurements are distributed within each environment bin. Differently from the classic stacked spectra fit, this approach has several advantages as it avoids introducing correlated noise caused by smoothing the individual spectra to a common velocity dispersion and by the continuum interpolation with polynomials (see Appendix B of Beverage et al. 2023). Following the 'a posteriori' approach as in Beverage et al. (2023), as first level of the models we computed the posterior probability distribution of each physical parameter listed in Table 4.1 for each individual galaxy as detailed in Chap. 4.2.2. Then, as a second level of modelling, we fitted the posterior of each parameter with a Student-t distribution in each environment bin. The use of the Student-t distribution accounts for potential high kurtosis in the parameter distributions. This approach provides a mean value for each parameter in each environment bin, the intrinsic scatter of our sample, along with a reliable estimate of the uncertainties. We assumed the same prior stated in Table 4.1 for each parameter, then we applied a logarithmically uniform prior for the intrinsic scatter between 0.01 and 10, and a logarithmically uniform prior for the degrees of freedom of the Student-t distribution between 1 and 10, where 1 represents an heavy-tailed distribution and 10 a gaussian one. Figure 4.6 shows an example of the posterior probability distribution of the [Z/H] parameter, its scatter, and the degrees of freedom of the Student-t distribution for the X-ray groups environment bin.

4.3 Results and discussion

As described in the previous sections, we spectroscopically selected 74 massive quiescent galaxies in the COSMOS Wall volume, and we analysed their physical properties performing a joint fit of their spectra and photometric data.

We combined the results obtained on individual galaxies to characterise the galaxy properties for the entire sample and in the three different environments defined in Chap. 4.1. In the following we present the obtained results and compare them with other studies in

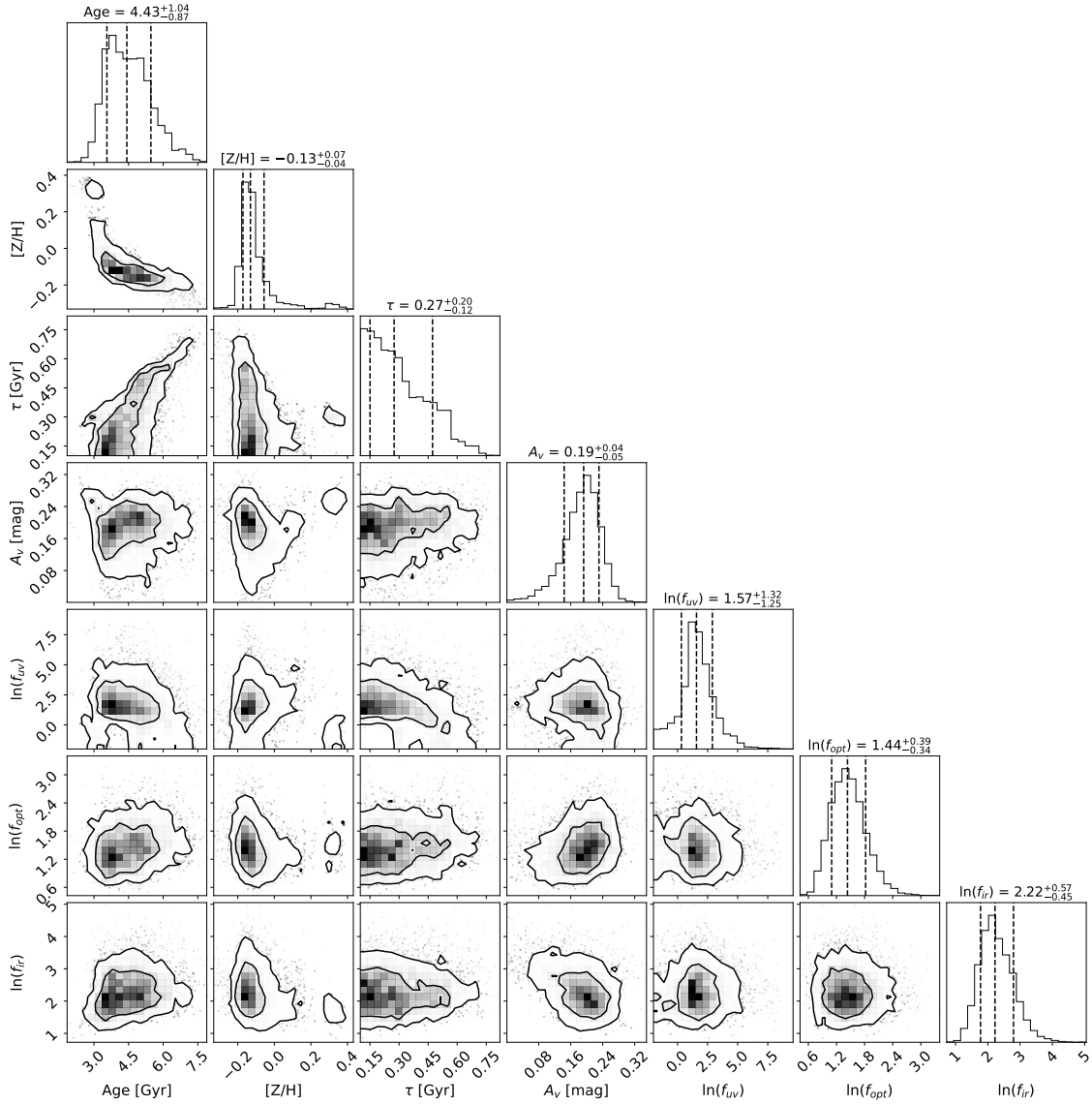

Figure 4.4: Example of the joint and marginal posterior distributions for the LEGA-C ID 209466 galaxy. Contours represent the 68% and 95% probability levels. The 16%, 50%, and 84% intervals are indicated as dashed lines.

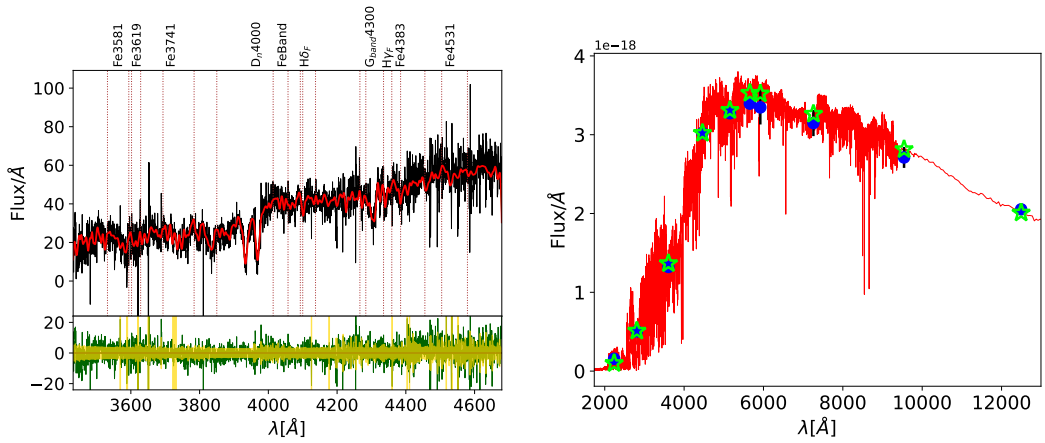

(a) (b)

Figure 4.5: Panel (a), top: Example of the best fit (in red) applied to the entire LEGA-C spectrum of the LEGA-C ID 209466 galaxy (in black). Panel (a), bottom: Difference between the observed spectrum and the best fit, shown in green, and the relative uncertainties of the observed spectrum, shown in yellow. Panel (b): Observed photometric measurements (blue points), best-fitting template (in red), and photometric measurements on the best-fitting template (lime stars). The green shaded region indicates the 68% confidence interval of our posterior.

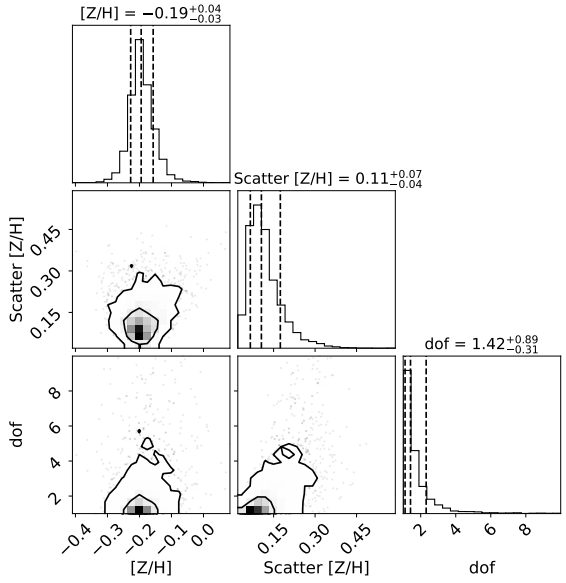

Figure 4.6: Corner plot summary of the posterior distributions of the [Z/H], its scatter, and the degrees of freedom of the Student-t distribution obtained for the galaxies in the X-ray group environment bin. Contours are at the 68% and 95% probability levels. The 16%, 50%, and 84% intervals are indicated by dashed lines.

Table 4.2: Median values of the marginalised posterior distribution of the $\mathrm{age_{model}}$, mass-weighted age, [Z/H], τ, and A_V of the second level model.

Environment bin	number of galaxies	$\mathrm{Age_{model}}$ [Gyr]	Mass-weighted age [Gyr]	[Z/H] [dex]	τ [Gyr]	A_V [mag]
X-ray groups	16	$5.83^{+0.66}_{-0.63}$	$5.52^{+0.67}_{-0.64}$	$-0.19^{+0.04}_{-0.03}$	$0.20^{+0.06}_{-0.05}$	$0.24^{+0.03}_{-0.03}$
Non-X-ray groups	22	$5.36^{+0.46}_{-0.47}$	$4.62^{+0.50}_{-0.45}$	$-0.17^{+0.06}_{-0.06}$	$0.50^{+0.07}_{-0.06}$	$0.28^{+0.04}_{-0.04}$
Field	36	$4.77^{+0.37}_{-0.36}$	$4.04^{+0.35}_{-0.37}$	$-0.02^{+0.05}_{-0.05}$	$0.50^{+0.06}_{-0.06}$	$0.30^{+0.02}_{-0.02}$
All	74	$5.18^{+0.25}_{-0.27}$	$4.46^{+0.25}_{-0.26}$	$-0.10^{+0.04}_{-0.04}$	$0.48^{+0.04}_{-0.04}$	$0.30^{+0.02}_{-0.02}$

The errors on the median values refer to the 16th and 84th percentiles.

literature (Chap. 4.3.1), and we finally discuss our results in the framework of the environmental effect on the evolution of the massive quiescent galaxies (Chap. 4.3.2).

4.3.1 Results and comparison with the literature

As described in Sect 4.1, our selected sample of massive quiescent galaxies is representative of the entire population of galaxies in the stellar mass range of $10.47 < \log M_*/\mathrm{M}_\odot < 11.4$. For each galaxy in the sample, we derived the following physical parameters: stellar mean metallicity, mean $\mathrm{Age}_{\mathrm{model}}$, star formation timescale (τ), and dust extinction (A_V). Using a Spearman rank correlation test, we found that none of these properties in each of the three environment bins are correlated with the stellar mass of the galaxies in each subsample with significance $> 2\sigma$. Therefore, the chosen small mass dynamic range and the uniformity of the mass distributions across the different environments enable the study of the environmental effects on galaxy properties. We then combined the physical properties of the individual galaxies using a hierarchical Bayesian approach to determine the parameters for the entire sample and the characterising the three environments of different galaxy densities.

Figure 4.7 shows the results obtained for $\mathrm{Age}_{\mathrm{model}}$, [Z/H] and τ as a function of the environment. The shaded grey regions represent the intrinsic scatter of the individual measured parameters in each environment bin. It is interesting to note that all the fits have shown values of $\mathrm{Age}_{model}/\tau$ higher than 3, confirming the purity and the fast star formation of the selected quiescent sample. Regarding the A_V parameter, we did not consider it as a quantity containing physical information, as it is has been derived from template fitting procedures and may partially account for potential mismatches between observations and models. At the same time, it is reassuring that we found a value of around 0.26 mag across all the environments (see Table 4.2) is consistent with results reported by other authors for massive galaxies at intermediate redshift (e.g. Citro et al. 2016).

From Table 4.2 and Fig. 4.7, a decreasing trend in the mass-weighted age of galaxies as a function of the environmental density is clearly evident. Galaxies in the X-ray groups have a typical mass-weighted mean age of 5.5 Gyr, and they become progressively younger moving towards less dense environments, with a typical age of 4 Gyr in the field, with a significance of almost 2σ. This means that galaxies in X-ray groups are about 1.5 Gyr older than those in the field, although the intrinsic scatter measured across all three environments exceeds 1.5 Gyr.

The top-right panel of Fig. 4.7 shows that galaxies in the field exhibit a stellar metallicity value that is around 0.15 dex higher than those in denser environments, with a significance greater than 2σ. Galaxies in both X-ray and non-X-ray groups display similar metallicity values, around $[\mathrm{Z/H}] = -0.18$ (i.e. 60% of the solar value).

Galaxies in X-ray groups appear quite homogeneous in their values of τ, representing the star formation timescale, and their measured τ value is significantly lower than those found in both the non-X-ray group environment and the field, even when accounting for the intrinsic scatter. It is worth noting that galaxies in non-X-ray groups and in the field present similar star formation timescales, but they differ by 0.6 Gyr in their mean mass-weighted age. The smaller intrinsic scatter observed in the stellar metallicity and τ for the sample in X-ray groups could indicate homogeneity in the physical processes that shaped these galaxies. In the next subsection we discuss possible explanations for this finding.

To check the robustness of our results, we compared them with those found by other authors in the literature. In particular, Darvish et al. (2017) proposed a different definition of the environment around the COSMOS Wall volume. In their work, they used the density

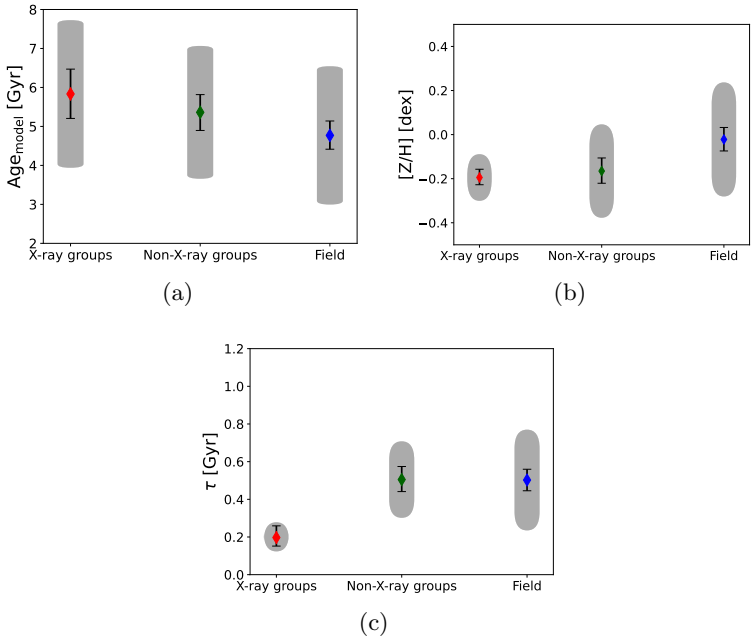

Figure 4.7: Age$_{\rm model}$, [Z/H], and τ in different environments. Upper left panel: Median values of the age$_{\rm model}$ with their relative error bars for different environments. Upper right panel: Median values of [Z/H] and their errors for different environments. Lower panel: Median values of τ and their errors for different environments. The grey shaded areas represent the intrinsic scatter of the individual posterior of the galaxies in each environment bin.

field Hessian matrix to disentangle the cosmic web into clusters, filaments and field (see Darvish et al. 2016, 2017, for full details). The main difference between the Iovino et al. (2016) and the Darvish et al. (2017) definitions of environment is that the former applied a group detection algorithm and then checked for X-ray emitting or non-X-ray emitting ones, considering all other galaxies located in the field, while the latter locates the galaxies based solely on the density of the environment, considering a global smoothing width of 0.5 Mpc, thus somewhat larger than the typical virial radius of groups. Darvish et al. (2017) performed a less detailed analysis of the galaxy stellar population properties in different environments compared to the one presented here, and found that the intrinsic colours of massive quiescent galaxies do not depend on the environment. We considered the results obtained in our analysis while classifying galaxies following Darvish et al. (2017) criteria. Our results confirm the trend that galaxies in denser environments tend to be older, have lower stellar metallicities, and shorter formation timescales compared to those in the field.

We also compared our results with those of Sobral et al. (2022). Exploring the full LEGA-C sample at $0.6 < z < 1$ and using the Darvish et al. (2017) definition of environment, they found that D$_n$4000 and Hδ indices for quiescent galaxies vary with both stellar mass and local density. In particular, at fixed stellar mass, their results suggest that quiescent galaxies residing in higher-density regions are older, meaning they formed the bulk of their stars earlier and quenched earlier. Their results are fully consistent with what we found in our analysis. Indeed, even in the narrow bin of mass and redshift we considered, we found that quiescent galaxies are older and with a shorter formation timescale in denser environment than in the field.

We compared our global results with those from other studies using LEGA-C data.

Within the same redshift and mass range, the mass-weighted age of our sample (~ 4.5 Gyr) is consistent within 0.5 Gyr with previous studies (e.g. Gallazzi et al. 2014; Chauke et al. 2018; Beverage et al. 2023; Kaushal et al. 2024), despite differences in stellar population models and analysis methodologies. It is also worth noting that the mean stellar metallicity of our sample (-0.1 dex) matches with the [Fe/H] abundance measured by Beverage et al. (2023). This further supports the robustness of our measurements, based solely on Fe indicators, suggesting that our total metallicity estimate effectively serves as a proxy for the [Fe/H] abundance.

In the local Universe, many previous studies have analysed the possible dependence of the physical properties of galaxies on the environment in which they are located. Sánchez-Blázquez et al. (2006) analysed quiescent galaxies in different environments, including Virgo and Coma clusters, finding that quiescent galaxies in lower-density environments appear younger by $1 - 2$ Gyr that those in denser environments, at given galaxy stellar mass. Their results is consistent with what we found in this work at higher redshift, suggesting an almost passive evolution from $z \sim 0.7$ to $z = 0$ for the most massive quiescent galaxies. A different conclusion is presented by Thomas et al. (2010). Using low-redshift data from the Sloan Digital Sky Survey ($0.05 \leq z \leq 0.06$), they found that the age and the stellar metallicity of the most massive quiescent galaxies do not depend on the environment and its density. Their results seem to suggest that the stellar population properties of the most massive quiescent galaxies are mainly driven by self-regulation processes related to intrinsic galaxy properties such as stellar mass. Our analysis of the properties of massive quiescent galaxies in the very narrow slice of redshift of the COSMOS Wall volume, at halfway of the Universe life, points out important differences related to the environment in which these galaxies are located. The differences we found are mainly in the mass-weighted age (i.e. galaxies in high-density environments are about 1.5 Gyr older than those in the field) and in the star formation timescale, which is roughly half in high-density environments compared to the field.

A possible explanation for the different results we found at $z \sim 0.7$ compared to those reported in Thomas et al. (2010), could be related to the small age differences we detected between X-ray groups galaxies and field ones. Indeed, precise age estimation is much more challenging in the local Universe than at higher redshift, since the typical spectral indices sensitive to the age of the stellar content lose sensitivity for old ages. Age measurement errors of about 10% in the local Universe correspond to uncertainties of approximately $1 - 2$ Gyr for ages around 10 Gyr. These uncertainties are of the same order as the age differences we estimated between galaxies in high- and low-density environments. Conversely, a limitation of our work is the relatively small sample size compared to those available at lower-z. Large surveys of quiescent galaxies at intermediate to high redshift will help reduce the statistical uncertainties affecting our work.

4.3.2 The environmental effect on stellar population parameters

The study of the age and the stellar metallicity provides valuable insights into the framework that describes the formation and the subsequent evolution of galaxies. In particular, thanks to the narrow redshift slice of the COSMOS Wall volume, the selection of a narrow stellar mass range, and detailed environment information from Iovino et al. (2016), we are able to investigate how the environment can affect the evolution of massive quiescent galaxies.

Figure 4.8 shows the cumulative mass fraction of the stellar mass as a function of the age of the Universe for galaxies in the three environments. As discussed in Chap. **??**, X-ray group galaxies are older and exhibit a shorter star formation timescale with respect

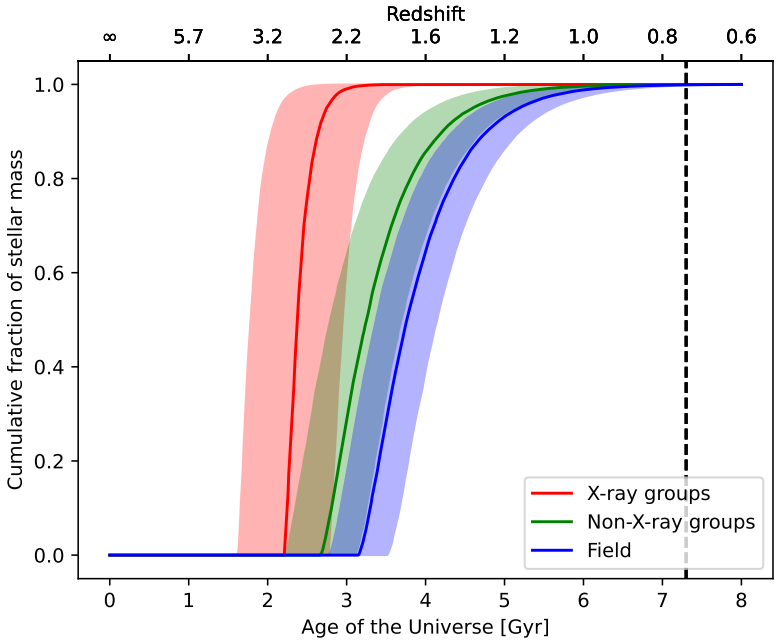

Figure 4.8: Cumulative mass fraction of the stellar mass as a function of the age of the Universe obtained for the galaxies in the three environment bins. The solid lines mark the 50% percentile of the distributions, while contours are at the 16% and 84% confidence intervals. The vertical dashed line corresponds to the redshift of the COSMOS Wall structure ($z \sim 0.73$).

to the less dense environments (see also Fig. 4.7). This suggests that they began forming their stars earlier and quenched at an earlier stage. These findings support the idea that the SFH of massive quiescent galaxies in denser environments is regulated by additional mechanisms compared to those acting in the field. Such mechanisms are responsible for the removal of the cold gas in galaxies, causing a sudden and rapid quenching of star formation in contrast to the slower quenching observed in field galaxies. The observed dependence of the quenching timescale on environmental density, combined with the uniformity in stellar mass among the studied galaxies, suggests that mechanisms such as ram-pressure stripping, active predominantly in dense environments, play a key role in explaining the observed differences between galaxies in X-ray groups and those in the field. This result is in good agreement with the SFHs derived for massive elliptical galaxies by Guglielmo et al. (2015), where the analysed galaxies show a faster decline of their SFR in clusters compared to the field. Interestingly, Zhou et al. (2025) found a similar result, analysing the star-forming galaxies in the Wall volume. Their semi-analytical approach, applied to stacked spectra of star-forming galaxies in the Wall volume, grouped by bins of mass and environment, supports the view that galaxies in dense environments start their star formation earlier than field galaxies and have systematically shorter star formation timescales.

Regarding stellar metallicity, our analysis of massive quiescent galaxies shows that cluster galaxies have lower metallicity compared to those in the field. A lower stellar metallicity in high-density environments can be due to mechanisms such as ram-pressure stripping or tidal interactions, which remove gas reservoirs, curtail star formation, and limit the enrichment of the interstellar medium. Another possibility is that, in higher-density environments, the efficient dilution of metals in the cold gas reservoirs is driven by gas inflows from the lower metallicity intergalactic medium or by galaxy-galaxy interac-

tions. In contrast, field galaxies benefit from prolonged gas availability, enabling extended star formation and chemical enrichment, which results in higher stellar metallicity. These results support the findings of Calabrò et al. (2022), who reported lower metallicities in galaxies in high-density environments compared to the field, even at higher redshifts. As mentioned above, it is important to note that, given the limited available wavelength range, we derived the total stellar metallicity in the sampled galaxies only on the basis of Fe indicators. In other words, the total metallicity we derived reflects the model assumption of the solar [Fe/Z] value. Massive quiescent galaxies, which formed very rapidly and early in the cosmic time, may be characterised by a $[Fe/Z] < [Fe/Z]_{\odot}$ due to an enhanced abundance of α elements relative to Fe. Indeed, Borghi et al. (2022) and Bevacqua et al. (2023), analysing the LEGA-C spectra of quiescent galaxies found on average $[\alpha/Fe] > [\alpha/Fe]_{\odot}$. Consequently, the trend in metallicity shown in Fig. 4.7 might reflect variations in $[\alpha/Fe]$ values across different environments, suggesting that the total metallicity could be higher than that measured. Notably, α-enhancement is expected in systems where stars formed on short timescales (Matteucci & Tornambe 1987; Thomas et al. 1999). Indeed, as reported in Table 4.2, we found that galaxies in X-ray groups are characterised by very short star formation timescales, shorter than those found in the other environments. This suggests that we may have underestimated the total metal content of galaxies in X-ray groups, which could be comparable to that of field galaxies, but with higher $\alpha-$enhancement in X-ray groups galaxies than in the field ones. Again, this result well matches what Zhou et al. (2025) found for the most massive star-forming galaxies in the Wall volume and their gas-phase metallicity.

The obtained results offer the opportunity to distinguish different evolutionary paths and quenching processes of massive quiescent galaxies. X-ray groups are characterised by hotter and denser intra-cluster medium compared to that in the non-X-ray groups (e.g. Boselli & Gavazzi 2006; Tonnesen et al. 2007). As a result, galaxies in X-ray groups are likely to be more significantly impacted by ram-pressure stripping than those located in small and less dense groups. Conversely, galaxies in less massive groups have a higher probability of merging and/or interacting with one another due their lower relative velocities. Figure 4.7 shows that galaxies in non-X-ray groups exhibit younger ages than those in denser environment and older ages than those in the field. They have a stellar metallicity similar to that found in denser environment but a star formation timescale more akin to that of field galaxies. From Fig. 4.8 we can see that these galaxies started their star formation activity at a similar epoch as those in denser clusters, but quenched later due to less efficient quenching mechanisms. While our results suggest a non-negligible role of dynamical processes affecting the gas supply available to galaxies in X-ray groups, the earlier formation time could also imply that star formation occurred in different internal physical conditions, leading to a more efficient star formation activity (and thus an earlier exhaustion of gas supply) even in absence of an active role of the environment. In this respect, however, we can leverage the sample of the non-X-ray groups, in which galaxies formed earlier than in the field but with the same timescale, possibly due to a similar rate of galaxy interactions and mergers in these two environments.

Higher S/N data covering a larger wavelength range will provide a clearer picture of the evolution of massive quiescent galaxies. Indeed, measuring the $[\alpha/Fe]$ is essential for obtaining a reliable estimation of the total stellar metallicity of quiescent galaxies, enabling a deeper insight into their complex assembly history across different environments.

4.4 Summary and conclusions

We have presented an analysis of the stellar populations of a sample of 74 massive quiescent galaxies in the COSMOS Wall to investigate the role of the environment in galaxy evolution. The COSMOS Wall is a structure at $z \sim 0.73$ that contains a large variety of environments, from rich and dense clusters down to empty field regions. The analysed sample was derived using the LEGA-C spectroscopic data; we selected galaxies with no detectable $[\mathrm{OIII}]_{\lambda 5007}$ or Hβ emission lines and at most a weak $[\mathrm{OII}]_{\lambda 3727}$ line. Additionally, we excluded post-starburst galaxies by requiring the Hδ absorption line with equivalent widths < 3 Å. From this sample, we selected galaxies in a narrow range of mass, $10.47 < \log M_*/\mathrm{M}_\odot < 11.4$, in order to have a representative, homogeneous sample in the slice of redshift of the COSMOS Wall across the different environments. We used the environment characterisation from Iovino et al. (2016), from which we found 16 galaxies in groups with X-ray detection, 22 in groups without X-ray detection, and 36 in the field.

We combined the LEGA-C survey spectroscopic data, which have high S/N and resolution suitable for studying the stellar population properties of galaxies, with the multi-wavelength photometric COSMOS2020 catalogue. We performed a joint fitting of spectra and photometric data using nested sampling techniques in order to measure the mass-weighted age, stellar metallicity, and star formation timescale of individual galaxies. After that, we assessed the stellar population parameters of each environment bin using a hierarchical Bayesian approach. Our findings can be summarised as follows:

- Quiescent galaxies in denser environments are about 1.5 Gyr older than those in the field.
- There is no significant difference in stellar metallicity between galaxies in the X-ray and non-X-ray groups, both showing values of about 60% of the solar value. Field galaxies exhibit metallicities approximately 0.15 dex higher.
- Galaxies in the X-ray groups have shorter star formation timescales. Those in the other two environment bins have similarly higher timescales despite a 1 Gyr difference in their mass-weighted ages.

Our results support the idea that the SFH of massive quiescent galaxies in denser environments is regulated by mechanisms different from those acting in the field. In particular, the presence of a hot and dense intra-cluster medium in the X-ray groups strongly suggests that ram-pressure stripping plays a key role in the quenching process. Processes like cosmological starvation could explain the physical parameters we observed in galaxies in the field, which have younger ages and longer star formation timescales compared to those in the X-ray groups. The longer star formation timescale of galaxies in non-X-ray groups indicates a more complex evolutionary history, likely driven by more frequent interactions and mergers, which is typical in less dense and smaller groups.

This study has provided a valuable step forward in understanding how environment shapes the quenching histories of massive quiescent galaxies. However, despite the precision reached in measuring their ages, metallicities, and star formation timescales, the analysis is still limited by the small number of galaxies with sufficiently high-quality spectra and by the absence of direct constraints on the α-element enhancement. As explained in Chap. 1.3 the [α/Fe] ratio is a key tracer of the duration of star formation, and its measurement is essential to fully characterise the evolutionary pathways of these systems and to properly interpret their chemical enrichment histories. Building on these

results, the next stage of this work expands the analysis to a much larger and statistically complete sample of the most massive quiescent galaxies. By exploiting recent wide-area spectroscopic surveys that provide the necessary wavelength coverage to measure [α/Fe], it becomes possible to trace, for the first time, the evolution of the most massive quiescent galaxies across a wide redshift range, bridging the gap between the intermediate-redshift Universe and the present day.

Chapter 5

The passive evolution of the most massive quiescent galaxies from $z \sim 0.8$ with BOSS and DESI

In the previous chapters, we have progressively introduced a framework to characterise the stellar population properties of galaxies, moving from controlled tests on simulations and spatially resolved analyses of individual systems to a first statistical study of quiescent galaxies in the COSMOS Wall. A final step is therefore to extend this investigation to a larger and more representative population of massive quiescent galaxies, tracing their evolution across cosmic time. In this context, we turn our attention to the luminous red galaxies (LRGs), a population of massive, passively evolving systems selected by their high luminosities and red optical colours, which reveal dominant old stellar populations (e.g. Eisenstein et al. 2001; Dawson et al. 2013; Maraston et al. 2013).

Thanks to their uniform properties and high intrinsic brightness, LRGs have long been used as both tracers of large-scale structure and benchmarks for studying the formation of the most massive galaxies in the Universe. The stellar population properties of LRGs, particularly their ages, total metallicities, and [α/Fe] abundance ratios, encode key information about their assembly histories. The [α/Fe] ratio, and specifically [Mg/Fe], provides a direct diagnostic of the duration of star formation. Enhanced [α/Fe] values point to short, intense formation episodes, whereas lower values indicate more extended star formation histories. Measuring this ratio across a broad redshift range is thus crucial to understanding when and how the most massive galaxies completed their stellar mass assembly and transitioned to quiescence.

In this work, we exploited the extensive spectroscopic datasets from the BOSS and DESI surveys to carry out a comprehensive analysis of the evolution of stellar population properties of LRGs across cosmic time. We focused in particular on the high-mass end of this population, selecting galaxies with stellar masses $11.5 < \log(M_*/\mathrm{M}_\odot) < 12.8$ to trace the most massive quiescent systems at each epoch. For the first time, we derived ages, total metallicities and in particular [Mg/Fe] abundance ratios for a large, mass-complete sample of massive LRGs that continuously spans the redshift range $0.15 < z < 0.8$. We then investigated how their stellar population properties evolve across the last ~ 7 Gyr of the cosmic history. The continuous redshift coverage of the sample represents a key advancement, enabling us to probe the evolutionary trends of massive quiescent galaxies

in a homogeneous and consistent way throughout this wide redshift range. Throughout the work, and differently from the other chapters of this thesis, we adopt a standard ΛCDM cosmology with $\Omega_M = 0.3089$, $\Omega_\Lambda = 0.6911$, and $H_0 = 67.8$ km s^{-1} Mpc^{-1} (Planck Collaboration et al. 2016).

5.1 Data and sample selection

In this section we present the LRGs samples drawn from the DESI and BOSS surveys and their most important properties, including the stellar mass completeness limits and redshift distributions.

5.1.1 DESI

We selected LRGs (Zhou et al. 2020, 2023) in the DESI Data Release 1 (DR1 DESI Collaboration et al. 2025), which covers all the data acquired during the first 13 months of the DESI main survey. The DESI DR1 includes spectra for more than 18 million unique target, covering around 9500 deg^2. According to Zhou et al. (2023), the LRGs target sample is $\geq 90\%$ complete for the most massive galaxies ($\log(M_*/\mathrm{M}_\odot) > 11.5$) within $0.4 < z < 1.0$. Although the DESI LRGs survey will be completed at the end of the full observational campaign, the DR1 offers a representative and statistically significant dataset of the final sample. We selected LRGs within two mass bins [$11.3 < \log(M_*/\mathrm{M}_\odot) < 11.5$, $11.5 < \log(M_*/\mathrm{M}_\odot) < 12.8$]. The higher–mass bin is $\sim 90\%$ complete, while the lower–mass bin reaches about 80% completeness but is still sufficient for the statistical analysis we aim to perform. We limited our selection to the redshift range $0.4 < z < 0.8$, ensuring that all spectral indices used in our analysis (see Chap. 5.2.3) are consistently available across the full sample.

5.1.2 BOSS

With the aim of extending the redshift range of our study, we complement the DESI dataset with the LRG sample from the BOSS survey (Eisenstein et al. 2011; Dawson et al. 2013), whose selection is more focussed on the redshift range $0.15 < z < 0.6$, allowing us to cover nearly 6 Gyr of cosmic history. The BOSS LRGs sample consists of two subsamples: a low-redshift sample (LOWZ), that contains galaxies up to $z \approx 0.4$, and a high-redshift sample (CMASS) for galaxies at $z > 0.4$. According to Leauthaud et al. (2016), the LOWZ selection is 80% complete for LRGs with $\log(M_*/\mathrm{M}_\odot) > 11.6$ in the redshift range $0.15 < z < 0.43$. We therefore adopt this mass and redshift cut to ensure a fair comparison with the complete DESI sample and to study the evolutionary trends down to $z = 0.15$. In addition, we include CMASS-selected LRGs up to $z < 0.6$ as a comparison sample of galaxies observed in both in DESI and BOSS surveys, in order to assess the consistency of these two datasets (App. B.1).

For the most massive quiescent galaxies, the DESI and BOSS fibres probe comparable physical regions within the galaxies, corresponding to approximately one effective radius over the redshift range considered in this work (see Favole et al. 2018). The DESI fibre has a diameter of 1.5 arcsec, while the BOSS fibre is slightly larger, with a 2 arcsec diameter. As shown in Fig. 5.1, the DESI and BOSS fibre apertures correspond to roughly one effective radius for a typical massive quiescent galaxy. However, the apparent size changes rapidly for the redshifts covered by BOSS, therefore we will take into account this difference when comparing the physical properties derived from the two surveys.

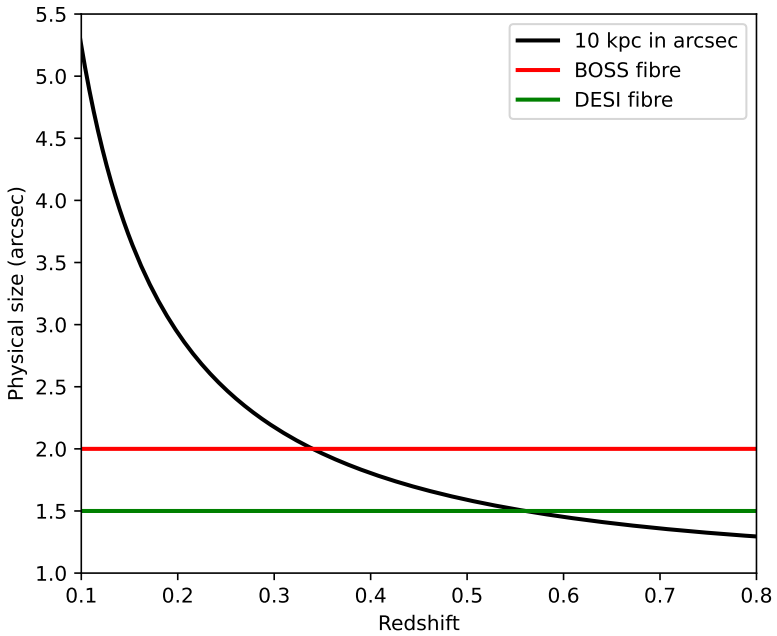

Figure 5.1: Apparent angular size (in arcsec) of a typical massive quiescent galaxy with an effective diameter of 10 kpc as a function of redshift. The horizontal red (green) line indicates the BOSS (DESI) fibre aperture.

We investigated potential differences of the stellar mass estimates between the DESI and BOSS surveys, by selecting LRGs observed in both, at $z < 0.4$, and applying the DESI mass threshold used for the sample comparison ($\log M_*/\mathrm{M}_{\odot,\mathrm{DESI}} > 11.5$). Stellar masses in the BOSS sample were derived assuming a Kroupa IMF (see Maraston et al. 2013), while DESI masses were estimated assuming a Chabrier IMF. In addition, the two surveys rely on different photometric data and SED fitting procedures. Figure 5.2 shows the stellar mass differences for the matched galaxies in DESI and BOSS. We found a median offset of ~ 0.1 dex, fully consistent with expected IMF-driven difference between Kroupa and Chabrier IMF assumptions (~ 0.05 dex, e.g. Longhetti & Saracco 2009; Bernardi et al. 2010) and different templates assumptions in the SED fitting procedures.

5.1.3 Further spectroscopic selection

Although the LRG samples are dominated by quiescent galaxies, their selection on a purely photometric basis means that a fraction of emission-line galaxies is inevitably included. To obtain a clean sample of quiescent galaxies, whose absorption lines are unaffected, or only minimally affected, by ongoing star formation or nuclear activity, we applied an additional selection criterion. We use the the following spectroscopic indicators: $[\mathrm{OII}]_{\lambda 3727}$, H$\delta$, H$\beta$, and $[\mathrm{OIII}]_{\lambda 5007}$, to define a subsample of spectroscopically confirmed quiescent galaxies satisfying these criteria:

- EW($[\mathrm{OIII}]_{\lambda 5007}$) < 1 Å;
- EW(Hβ) < 1 Å;
- EW($[\mathrm{OII}]_{\lambda 3727}$) < 5 Å;
- EW(Hδ) < 1 Å.

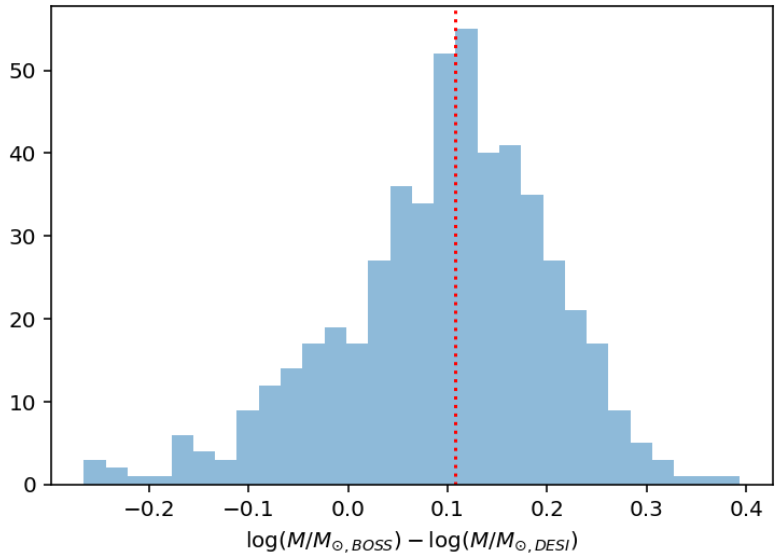

Figure 5.2: Histogram of the stellar mass differences for the matched galaxies in DESI and BOSS. The dotted red line marks the median value of the distribution.

where EW stands for Equivalent Width defined such that positive values correspond to emission. These criteria are designed to select galaxies with no detectable $[\mathrm{OIII}]_{\lambda 5007}$ and Hβ emission lines and at most a weak $[\mathrm{OII}]_{\lambda 3727}$ emission, which can occur in quiescent galaxies at these redshifts (see Maseda et al. 2021; Ditrani et al. 2025). Regarding the DESI sample, we used the emission lines measured from the DR1/Iron value-added catalogue to follow the criteria described above, while for the BOSS sample we used the emissionLinesPort table from the SDSS database. Finally, we added a last criterion, $-3 <$ EW(Hδ) < 0 Å, to exclude post-starburst galaxies from our sample, following the definition of Poggianti et al. (2009) and Werle et al. (2022). Galaxies with stronger Hδ are recently quenched galaxies, which are likely to have experienced a different evolutionary track compared to the older passive galaxies that compose our sample. We measured the EW(Hδ) in each spectrum and we selected galaxies with $-3 <$ EW(Hδ) < 0 Å, obtaining a sample of 183850 quiescent galaxies from the DESI survey, 3090 ones from the BOSS CMASS selection and 5810 from the BOSS LOWZ selection.

5.1.4 Stacked spectra

The BOSS and DESI samples provide us with a rich statistical sample of LRGs, albeit at a median SNR insufficient to robustly determine the stellar population parameters of the selected population on individual spectra. We therefore stack blocks of individual spectra to boost the SNR for our measurements in order to reach an SNR of ~ 20. In the DESI sample, at $0.4 < z < 0.8$, the median SNR of individual spectra is around 4/Å in the rest-frame range $4000 - 4200$Å. Therefore, we stacked the individual spectra in groups of 50 objects, in bins of $\Delta z = 0.01$, and within two mass bins [$11.3 < \log(M_*/\mathrm{M}_\odot) < 11.5$, $11.5 < \log(M_*/\mathrm{M}_\odot) < 12.8$], in order to stack galaxies with the most similar properties in the $z - \log(M_*/\mathrm{M}_\odot)$ plane. The chosen stacking redshift bin is wide enough to include spectra with slightly different observed wavelength ranges, allowing for optimal removal of bad pixels and sky-subtraction residuals. We perform 201 realisations using a random choice of the selected 50 spectra in each bin, in order to obtain a robust measurement of

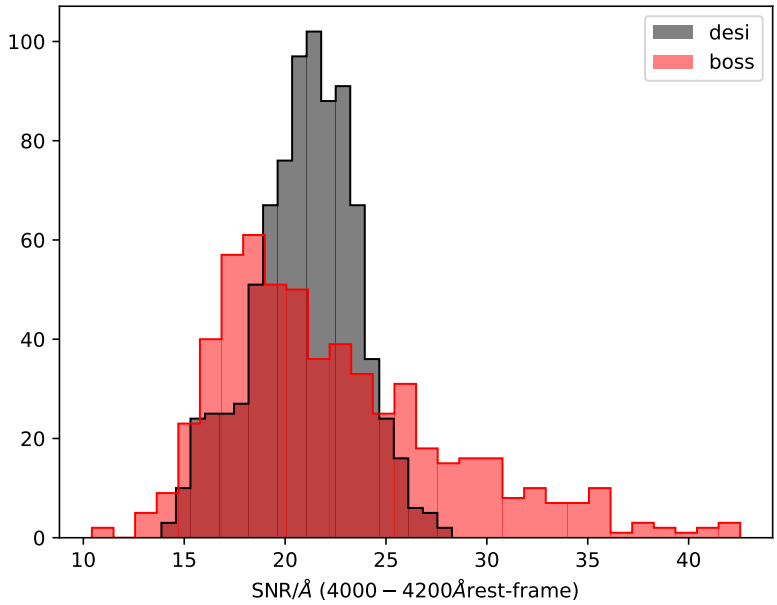

Figure 5.3: SNR distributions for the DESI stacked spectra, in black, and BOSS, in red, in the rest-frame range $4000 - 4200$Å.

the errors associated to each pixel. From this step we obtained 2835 stacked spectra in the mass bin $11.3 < \log(M_*/\mathrm{M}_\odot) < 11.5$ and 842 in the mass bin $11.5 < \log(M_*/\mathrm{M}_\odot) < 12.8$.

Regarding the BOSS LOWZ sample, the median SNR of individual spectra is around 8/Å, therefore we stacked groups of 10 spectra in order to achieve a SNR comparable to that of the DESI stacked spectra. Figure 5.3 shows the SNR distributions for the DESI and BOSS stacks in the rest-frame range $4000 - 4200$Å. The BOSS distribution, that consist of 581 stacked spectra, has a longer high tail compared to DESI, but the median values are consistent to SNR ~ 21.5/Å.

We stacked only the minimum number of spectra required to reach an SNR of ~ 20/Å. This approach preserves the possibility of estimating at least a lower limit to the intrinsic spread of stellar population properties within each bin, which would otherwise be lost if all available spectra were combined together. Moreover, pushing the SNR too high would risk exceeding the intrinsic uncertainties of the models themselves, potentially leading to misleading results.

5.2 Analysis

Our goal is to characterise the star formation and chemical enrichment history of massive LRGs through their light-weighted age, their stellar metallicity, and [Mg/Fe] abundance. In this section, we describe in detail the steps of the analysis on our sample. Specifically, in Chap. 5.2.1 we introduce the synthetic templates used to analyse the selected galaxies. In Chap. 5.2.2 we measure the stellar kinematics and extraction of the stellar spectra. In Chap. 5.2.3 we describe the performed fit of spectra using Monte Carlo techniques. Finally we present how we assess the stellar population parameters as function of redshift using the hierarchical bayesian modeling (Chap. 5.2.4).

5.2.1 Stellar population models

We exploited the semi-empirical Simple Stellar Populations (SSPs) models from Knowles et al. (2023) (sMILES) to measure the light-weighted age, stellar metallicity and Mg/Fe of our stacked spectra. These models represent the state-of-the-art in [Mg/Fe] abundance resolution, allowing for a more accurate fit of its non-linear dependence across the parameter space. The SSP models adopt the BaSTI evolutionary tracks (Pietrinferni et al. 2004, 2006) and the MILES empirical stellar library ($3540.5 < \lambda < 7350.2$ Å; Sánchez-Blázquez et al. 2006; Falcón-Barroso et al. 2011, 2.5Å FWHM resolution). We assumed a Kroupa initial mass function (IMF, Kroupa 2001). The synthetic library provides 2650 SSPs unevenly spaced in linear age and [Z/H], covering 53 ages from 0.03 Gyr to 14 Gyr, 10 metallicities from [Z/H] $= -1.79$ to [Z/H] $= 0.26$ dex, being the solar abundance $Z_\odot = 0.0198$, and five [Mg/Fe] abundances from -0.2 to 0.6 dex.

5.2.2 Kinematics and residual emission subtraction

For each stacked spectrum in the sample, we determined the kinematic parameters (i.e., recession velocity and velocity dispersion) using the latest version of the pPXF code[1](Cappellari & Emsellem 2004; Cappellari 2022), adopting the template set from the MILES stellar spectral library, considering the rest-frame wavelength range between 3800 Å and 5500 Å. Synthetic templates were then shifted to match the recession velocity of each galaxy and convolved with the estimated stellar velocity dispersion. Even if we applied the spectroscopic criteria in Chap. 5.1, the individual spectra have a low SNR, and they might be affected by low levels of nebular emission in the core of absorption features. We address this issue with the stacked spectra, their high SNR make them suitable to fit them with emission line templates at the Balmer lines. This is particularly important at $H\beta$, where the emission line, if present, should be stronger, thus affecting the estimated age. We performed an additional two-step pPXF spectral fitting to extract the nebular emission component from each stacked spectrum, this time fixing the kinematics measured in the previous stage. We first performed a fit using pPXF in the $4000\text{Å} < \lambda < 5500\text{Å}$ range considering only the $H\beta$ emission line (the strongest Balmer line in the observed range), to obtain a reliable estimate of the kinematics of the nebular emissions. After this step, using the same wavelength range, we fitted $H\delta$, $H\gamma$ and $H\beta$ emission lines fixing the nebular kinematics obtained in the previous fit. We retained only fits in which $H\delta < H\gamma < H\beta$, in order to exclude fits that fail to properly reproduce the Balmer line flux sequence. In cases where the condition was not satisfied, we fixed the emission line ratios to the case B recombination (Osterbrock 1989). Finally, we subtracted the best-fit nebular components from the total spectra, deriving clean stellar spectra. We performed 1000 realisations of the nebular best-fit by perturbing the emission line fluxes according to their associated flux uncertainties, in order to estimate the pixel-wise errors in the $H\delta$, $H\gamma$, and $H\beta$ regions of the nebular component. These estimated uncertainties were then added in quadrature to those of the observed spectrum.

5.2.3 Full-index fitting

We then adopted the full-index fitting approach (FIF, Martín-Navarro et al. 2014; Ditrani et al. 2025) to compare the observed spectra with the synthetic spectral templates. Unlike the more classic index fitting approach, FIF compares the flux within a specific absorption feature (with respect to its continuum value) pixel by pixel rather than averaging it. This

[1]https://pypi.org/project/ppxf/

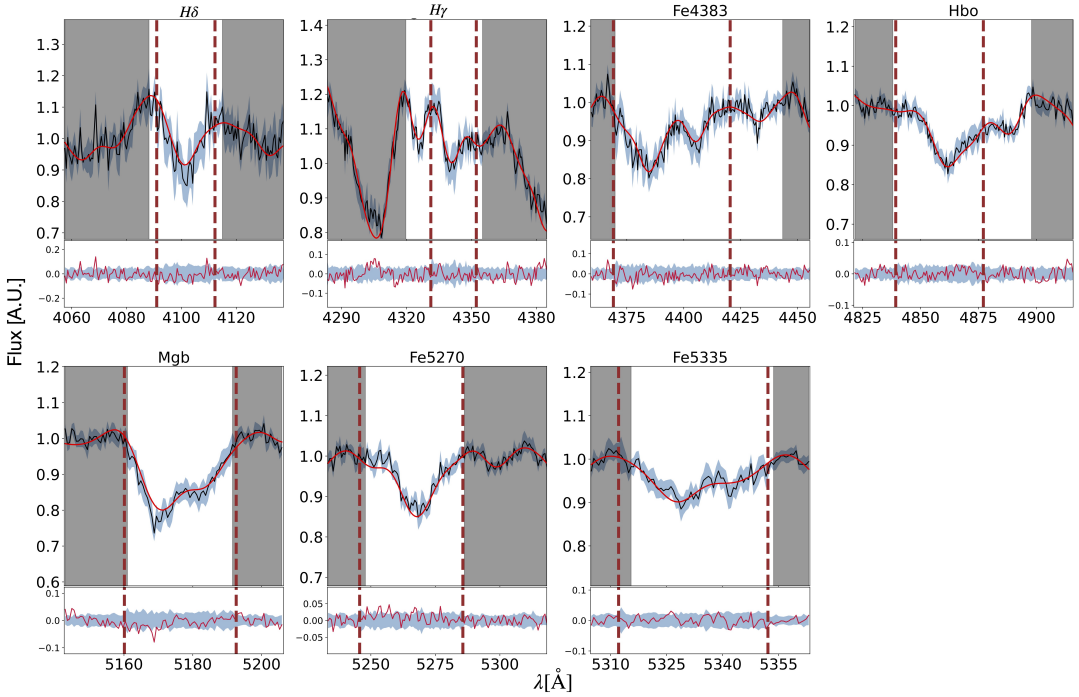

Figure 5.4: FIF application on the selected indices for a stacked spectrum in the DESI sample. The vertical dashed brown lines indicate the feature boundaries for each index while the grey shaded regions represent the pseudo-continua used for normalization. In the upper subplots, the black lines and blue shaded regions correspond to the observed spectrum and its associated uncertainty, respectively. The solid red line represents the best-fit derived from the posterior distribution. The red lines in the lower subplots show the residuals between the observed spectrum and the best fit, with the blue shaded region indicating the relative uncertainties of the observed spectrum.

pixel-level comparison within the index window is more effective in breaking the degeneracy between age and metallicity compared to the classical index analysis, as it accounts not only for the strength of the absorption feature but also for its detailed shape, which provides additional information about the stellar population parameters. (Martín-Navarro et al. 2019; Ditrani et al. 2024). We applied the FIF method to a comprehensive set of spectral indices sensitive to the age, stellar metallicity and [Mg/Fe], listed in Table **??**. Figure 4.3 shows the results of an example of the FIF approach applied to one of the selected galaxies. The best-fit template closely matches each spectral feature, capturing detailed information from both their depth and shape.

The modelling of the Balmer lines with [Mg/Fe] $\neq 0$ (see Vazdekis et al. 2015; Knowles et al. 2023) is known to be problematic, as it relies on stellar models computed under the assumption of local thermodynamic equilibrium (LTE), which may underestimate Balmer line depths in Mg-enhanced or hot stellar populations, where non-LTE effects are known to be non-negligible. To mitigate this issue, we fitted the set of indices [Hδ_F, Hγ_F, $H\beta_o$] adopting SSP templates corresponding to [Mg/Fe] $= 0$, while we fitted the remaining indices using SSPs with variable [Mg/Fe] abundance ratio. We computed the total posterior probability distribution using the likelihood given by $\mathcal{L} = e^{-\chi^2/2}$, with

$$\chi^2 = \sum_i \left(\frac{F_{obs_i} - F_{syn_i}}{\sigma_{obs_i}} \right)^2 \tag{5.1}$$

Table 5.1: Spectral indices used for our analysis ((1)Worthey et al. (1994); (2) Cervantes & Vazdekis (2009)).

Index	Blue pseudocontinuum	Central feature	Red pseudocontinuum	Fit	Ref.
Hδ_F	4057.25-4088.50	4091.00-4112.25	4114.75-4137.25	[Mg/Fe] = 0	1
Hγ_F	4283.50-4319.75	4331.25-4352.25	4354.75-4384.75	[Mg/Fe] = 0	1
Fe4383	4359.125-4370.375	4369.125-4420.375	4442.875-4455.375	variable [Mg/Fe]	1
$H\beta_o$	4821.175-4838.404	4839.275-4877.097	4897.445-4915.845	[Mg/Fe] = 0	2
Mgb	5142.625-5161.375	5160.125-5192.625	5191.375-5206.375	variable [Mg/Fe]	1
Fe5270	5233.150-5248.150	5245.650-5285.650	5285.650-5318.150	variable [Mg/Fe]	1
Fe5335	5304.625-5315.875	5312.125-5352.125	5353.375-5363.375	variable [Mg/Fe]	1

Table 5.2: The 3 free parameters fitted to our spectroscopic data, along with their associated prior distributions.

Parameter	Unit	Range	Prior
$\mathrm{Age_{model}}$	Gyr	(0, $\mathrm{Age_{Universe}}$)	Uniform
[Z/H]	dex	(-1.79, 0.26)	Uniform
[α/Fe]	dex	(-0.2, 0.6)	Uniform

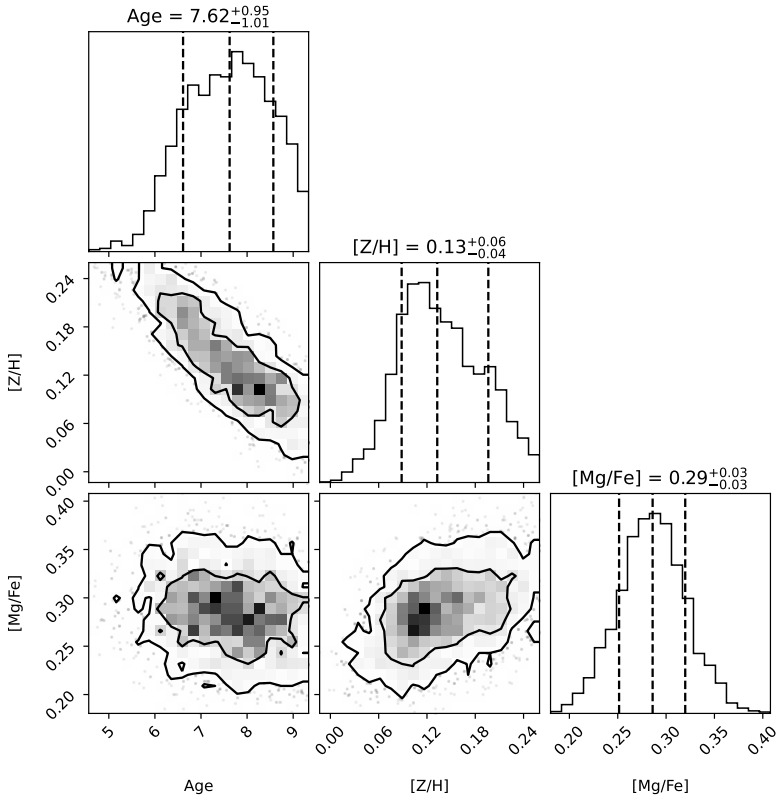

Figure 5.5: Example of the joint and marginal posterior distributions for a DESI stacked spectrum. Contours represent the 68% and 95% probability level. The 16%, 50% and 84% intervals are indicated as dashed lines.

where F_{syn_i} is the flux of the synthetic spectrum along the feature of each index, and F_{obs_i} is the flux of the observed spectrum with the error σ_{obs_i}. We derived posterior probability distributions and the Bayesian evidence using the nested sampling Monte Carlo algorithm MLFriends (Buchner 2016, 2019) using the UltraNest[2] package (Buchner 2021). We assumed uniform prior for all the parameters considered, summarised in Table 4.1. Figure 4.4 shows an example of the joint and marginal probability distributions for all the fitted parameters.

5.2.4 Hierarchical Bayesian Modeling

To assess the stellar population parameters in each redshift bin, we combined the obtained results for each individual stack using the hierarchical bayesian modeling. In the hierarchical framework, our models consist of two levels: the first level involves the mea-

[2] `https://johannesbuchner.github.io/UltraNest/`

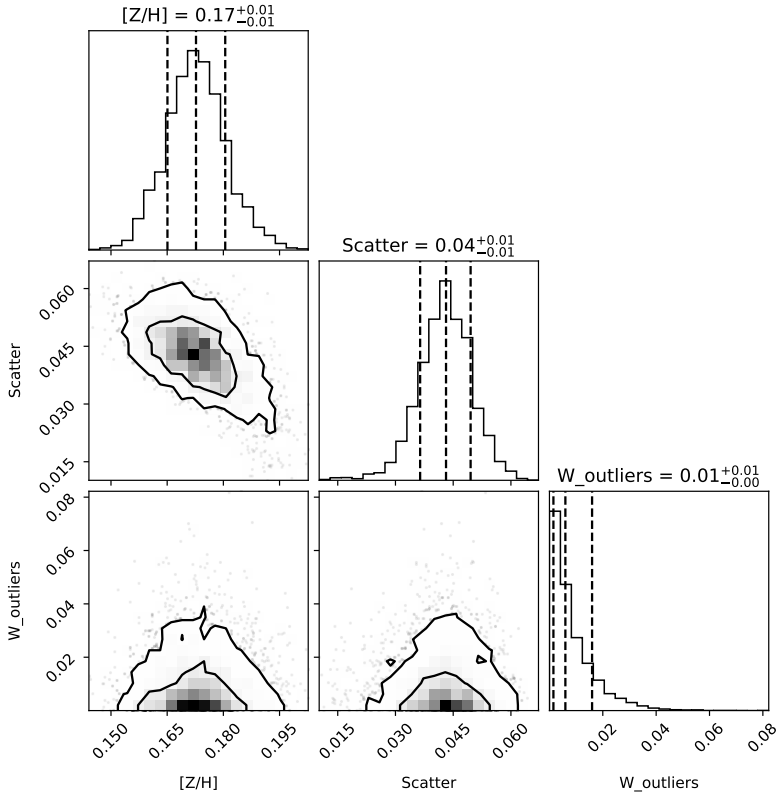

Figure 5.6: Corner plot summary of the posterior distributions of the [Z/H], its scatter, and the fraction of outliers obtained for the stacked spectra in the $0.45 < z < 0.5$ bin. Contours are at the 68% and 95% probability. The 16%, 50% and 84% intervals are indicated by dashed lines.

surements of the parameters for each individual stacked spectrum, while the second level describes how the measurements are distributed within each redshift bin. Differently from the classic stacked spectra fit, this approach has several advantages as it avoids introducing correlated noise caused by smoothing the individual spectra to a common velocity dispersion and by the continuum interpolation with polynomials (see Appendix B in Beverage et al. 2023). Following the 'a posteriori' approach (e.g. Beverage et al. 2023; Ditrani et al. 2025), as first level of the models we computed the posterior probability distribution of each physical parameter listed in Table 4.1 for each individual stacked spectrum as detailed in Chap. 5.2.3. Then, as a second level of modelling, we fitted the distribution of the posteriors of each parameter with a Gaussian function plus an outlier model in each redshift bin. This approach provides a mean value for each parameter in each selected redshift bin, the intrinsic scatter of our sample, along with a reliable estimate of the uncertainties. We assumed the same prior listed in Table 4.1 for each parameter, then we applied a logarithmically uniform prior for the intrinsic scatter between 0.01 and 10 dex, and a uniform prior for the fraction of outliers within $0 - 20\%$. We performed the measurements in redshift bins of width $\Delta z = 0.05$ to ensure to have a statistically significant sample in each bin. Figure 5.6 shows an example of the posterior probability distribution of the [Z/H] parameter, its scatter, and the fraction of outliers for the DESI spectra in the redshift bin $0.45 < z < 0.5$.

5.3 Results

As detailed in the previous sections, we analysed stacked spectra of galaxies from the BOSS and DESI surveys to characterise the stellar populations of these systems. For each stacked spectrum, we derived the light-weighted age, stellar metallicity and [Mg/Fe], and we obtained the mean parameters at different redshift bins through the hierarchical bayesian modeling. In the following we present the results obtained. Specifically, we discuss the stellar population parameters of the DESI stacked spectra in two distinct mass bins, the redshift evolution for the parameters of the most massive galaxies across the full BOSS and DESI redshift range, and the comparison with massive passive galaxies from the TNG simulations.

5.3.1 Observational results

Figure 5.7 shows the evolution of the light-weighted age, [Z/H] and [Mg/Fe] in the redshift range $0.4 < z < 0.8$ for the DESI sample in the two mass bins [$11.3 < \log(M_*/\mathrm{M}_\odot) < 11.5$, $11.5 < \log(M_*/\mathrm{M}_\odot) > 12.8$]. The distributions of the stellar population parameters follow consistent trends across the redshift range, suggesting similar star formation histories in the two mass bins. Overall, galaxies in the higher mass bin exhibit systematically older ages, higher stellar metallicity and higher [Mg/Fe] across the entire redshift range covered by DESI, although these differences remain within the 1σ uncertainties.

Figure 5.8 shows the evolution of the light-weighted age, [Z/H] and [Mg/Fe] in the redshift range $0.15 < z < 0.8$ for stacked spectra of galaxies in the BOSS and DESI samples. As described in Chap. 5.2.4, we estimated the mean and intrinsic scatter of each parameters in redshift bins of width $\Delta z = 0.05$. Overall, the two surveys show consistent evolutionary trends and all parameters exhibit clear correlations with redshift. Despite being independent datasets, the BOSS and DESI results agree well where they overlap, supporting a consistent selection of the LRGs in both surveys and the mass comparison described in App. B.1. Within each redshift bin, we found no evidence for significant intrinsic scatter beyond the observational errors of the individual stacked spectra, suggesting that the galaxy population is homogeneous within our resolution limits. In both samples, galaxies exhibit an evolution of the light-weighted age consistent with pure passive evolution, with a nearly constant offset between the age of the Universe and the measured stellar ages. We found that this age offset decreases from approximately 3.5 Gyr to 3 Gyr towards lower redshift, in agreement with passive evolution. The galaxies stellar metallicity shows a mild increase and an overall flat trend in the [Mg/Fe] ratio towards lower redshift, supporting the picture of a passive evolution of the most massive passive galaxies.

5.3.2 Test with TMJ

We verified whether the obtained results depend on the assumed model templates and their selected parameters. For this test, we fitted the DESI and BOSS stacked spectra using the models from Thomas et al. (2011) (hereafter TMJ). These models are based on the Cassisi evolutionary tracks (Cassisi et al. 1997) and the MILES empirical stellar library. The models assume a Kroupa initial mass function. The synthetic library provides predictions of 25 indices for each SSP. The SSPs are unevenly spaced in linear age and [Z/H], covering 20 ages from 0.1 Gyr to 15 Gyr, 6 metallicities from [Z/H] $= -2.25$ to [Z/H] $= 0.67$ dex, and five [α/Fe] abundance ratio from -0.3 to 0.5 dex. To perform the analysis, Figure 5.9 shows the results obtained using the TMJ models for the light-weighted age, [Z/H] and [Mg/Fe] in the redshift range $0.15 < z < 0.8$. As for the analysis based on the sMILES

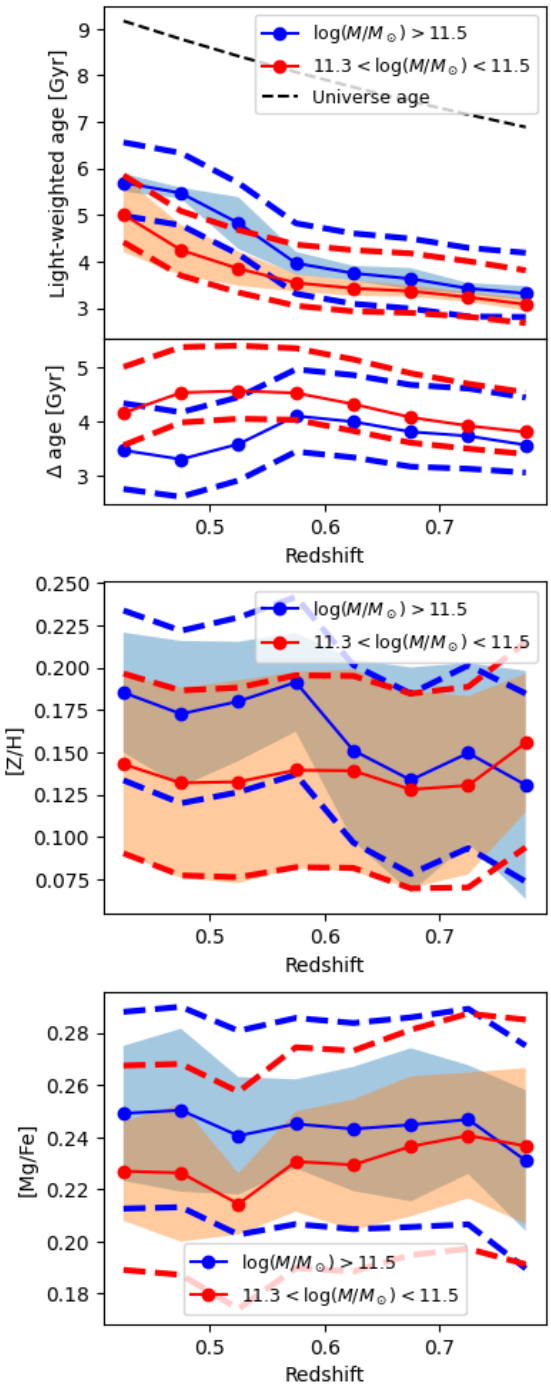

Figure 5.7: Evolution of the light-weighted age, [Z/H] and [Mg/Fe] in the redshift range $0.4 < z < 0.8$ in the mass bins $[11.3 < \log(M_*/\mathrm{M}_\odot) < 11.5,\ 11.5 < \log(M_*/\mathrm{M}_\odot) < 12.8]$. The data points represent the median value in each redshift bin, the dashed lines cover the typical uncertainties of the stacked spectra, and the shaded regions correspond to the intrinsic scatter within each bin. The dashed black line in the top panel represents the age of the Universe at each redshift.

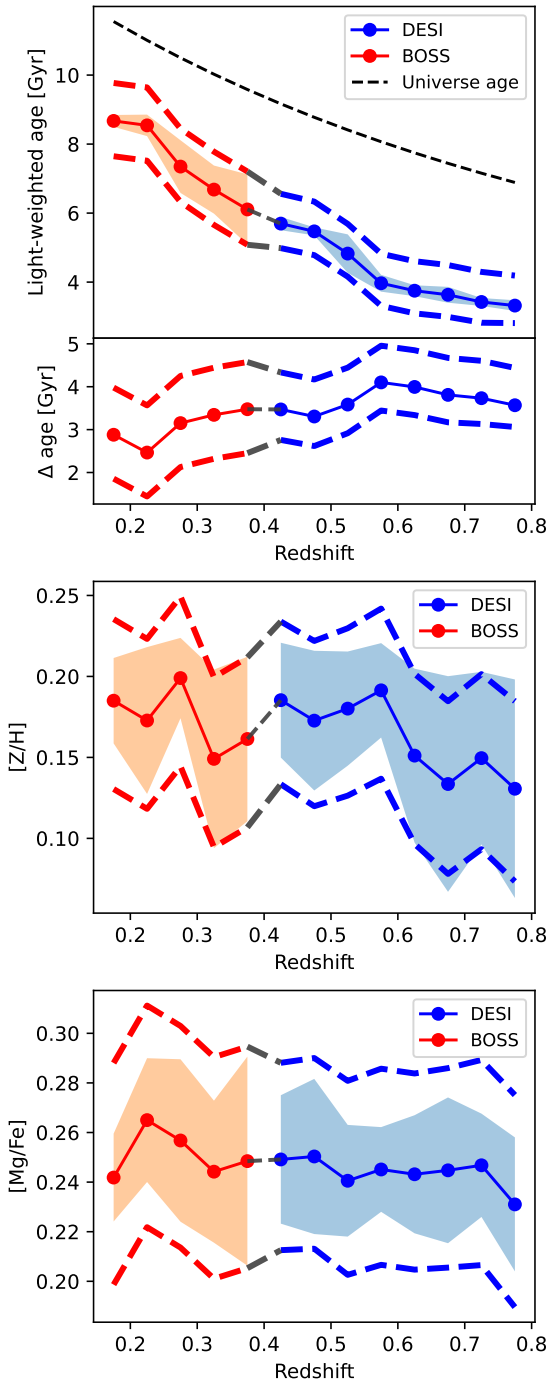

Figure 5.8: Evolution of the light-weighted age, [Z/H] and [Mg/Fe] in the redshift range $0.15 < z < 0.8$. The data points represent the median value in each redshift bin, the dashed lines cover the typical uncertainties of the stacked spectra, and the shaded regions correspond to the intrinsic scatter within each bin. The dashed black line in the top panel represents the age of the Universe at each redshift.

models, the light-weighted ages and [Mg/Fe] derived using the TMJ models are consistent with pure passive evolution. Moreover, the [Z/H] measurements remain approximately constant with redshift but exhibit a systematic offset between the two surveys. This offset may arise from differences in spectral resolution, since the TMJ models adopt a fixed resolution, while the BOSS instrumental resolution varies with wavelength. At the redshift range of the BOSS galaxies the spectral resolution is, on average, lower than that of the models, particularly in the red spectral region where the metallicity-sensitive indices are located. In the analysis with the TMJ models, the observed spectra are degraded to match the model resolution. However, in cases where the instrumental resolution is poorer than that of the models, this correction cannot be applied. As a consequence, the comparison with higher-resolution model templates may lead to a slight underestimation of the metallicity, as the broadened absorption features in the observed spectra appear weaker than in the models. Nevertheless, this systematic difference does not affect the relative trends discussed above. This consistency across different model assumptions strengthens the robustness of our analysis and confirms that the inferred evolutionary trends are not driven by the choice of stellar population models.

5.3.3 Comparison with IllustrisTNG simulations

The IllustrisTNG simulations (Springel et al. 2018; Pillepich et al. 2018; Nelson et al. 2019, TNG hereafter) are a series of cosmological magnetohydrodynamical simulations that model a range of physical processes for the formation of galaxies. Each TNG simulation includes a comprehensive model of galaxy formation and evolution from $z = 127$ to $z = 0$, generating several snapshots across the cosmic time. The initial conditions of the TNG snapshots have been initialised at $z = 127$ assuming a matter density $\Omega_m = \Omega_{dm} + \Omega_b = 0.3089$, baryonic density $\Omega_b = 0.0486$, cosmological constant $\Omega_\Lambda = 0.6911$, Hubble constant $H_0 = 100h$ km s^{-1} Mpc^{-1} with $h = 0.6774$ (Planck Collaboration et al. 2016). In this work, we considered the TNG300-1, that provides a simulation box with a large comoving side length of 300 Mpc. For our analysis, we considered snapshots within the redshift range $0.15 < z < 0.8$, in order to compare the stellar population parameters of simulated galaxies with those obtained from the spectral analysis of our sample. Specifically, we used the full snapshots $59, 67, 72, 78$, and 84, corresponding to $z = [0.7, 0.5, 0.4, 0.3, 0.2]$, as the [Mg/Fe] information is only available in the full snapshots. For each snapshot, we selected galaxies with $\log(M_*/\mathrm{M}_\odot) > 11.5$ and $\log(sSFR) < -11$, following selection criteria consistent with those adopted for the BOSS and DESI samples. Moreover, we derived light-weighted age, [Z/H] and [Mg/Fe] within one effective radius of each galaxy, to ensure consistency between simulated and observed values.

Figure 5.10 shows the the evolution of the light-weighted age, [Z/H] and [Mg/Fe] as a function of redshift for stacks of galaxies in the BOSS and DESI samples, alongside the parameters of the selected galaxies across the five TNG snapshots. The light-weighted age of TNG galaxies closely track the observed trends in the BOSS and DESI stacks, with ages increasing from 4 Gyr to 9 Gyr toward lower redshifts, with an almost constant difference between the age of the Universe and the measured light-weighted age. This agreement lends support to the adopted selection of massive and passive galaxies in the TNG snapshots for the comparison.

Regarding the total metallicity, observed galaxies show a mild increase in [Z/H] towards lower redshift. The TNG galaxies exhibit similar mild trend, though with a slight decrease at lower redshift. However, the observed uncertainties and the scatter in the simulations are fully consistent with each other, suggesting an almost flat trend for both cases.

Regardless of the absolute offset, the redshift evolution of [Mg/Fe] in TNG galaxies

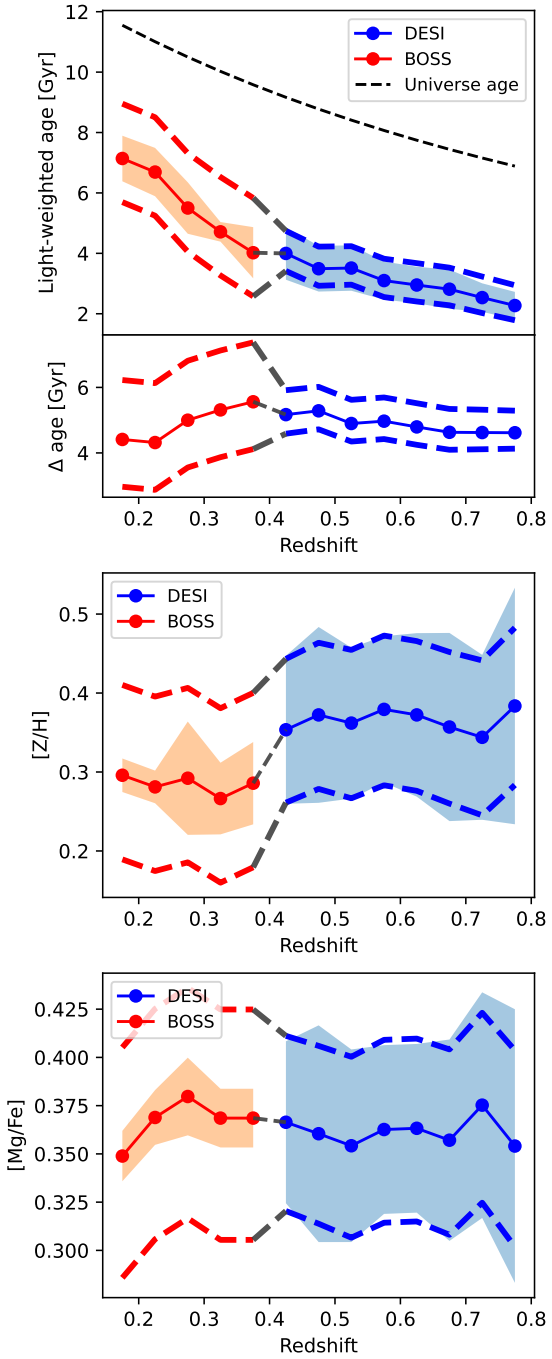

Figure 5.9: Results obtained using the TMJ models for the light-weighted age, [Z/H] and [Mg/Fe] in the redshift range $0.15 < z < 0.8$. The data points represent the median value in each redshift bin, the dashed lines cover the typical uncertainties of the stacks, and the shaded regions correspond to the intrinsic scatter within each bin. The dashed black line in the top panel represents the age of the Universe at each redshift.

closely follows the observed trend obtained from the observations, both showing a constant trend across the entire redshift range. However, the [Mg/Fe] values predicted by TNG simulations for massive quiescent galaxies are systematically higher by up to ~ 0.2 dex than those derived from observations (Naiman et al. 2018). This discrepancy likely originates from differences in nucleosynthetic yields and stellar population modeling. Indeed, according to Naiman et al. (2018), the offset may point to an overproduction of Mg relative to Fe from core-collapse supernovae or a too low rate of Type Ia supernovae in the simulation assumptions.

5.4 The evolution of LRGs within $0.15 < z < 0.8$

The study of the age, the stellar metallicity and the [Mg/Fe] abundance ratio of massive LRGs across the cosmic time provides valuable insights into the framework of galaxy formation and evolution. Thanks to the extensive spectroscopic datasets from the BOSS and DESI surveys, we are able to investigate how the most massive and passive galaxy population evolve in the redshift range $0.15 < z < 0.8$, and, for the DESI sample, to explore the effect of stellar mass by comparing adjacent mass bins.

The DESI results reveal consistent evolutionary trends for galaxies in the two mass bins, with the more massive systems showing slightly older ages, higher stellar metallicities, and enhanced [Mg/Fe] ratios across the redshift range $0.4 < z < 0.8$. Although these systematic differences are within the 1σ uncertainties, they are suggestive of a mild downsizing effect, in which the more massive galaxies formed their stars earlier and over shorter timescales than their lower-mass counterparts. The measured intrinsic scatter is comparable with the uncertainties across both mass and redshift bins for all parameters, suggesting a homogeneous stellar population within the DESI stacked spectra.

Given the wide redshift range covered by our analysis, we can compare our results with previous studies of massive passive galaxies at different epochs. As shown in Figure 5.8, the most massive passive galaxies exhibit a passive evolution of the light-weighted age, with an almost constant offset from the Universe age. The slight age offset from 3.5 Gyr to 3 Gyr toward lower redshift can be explained by aperture effects. Because of the fixed angular size of the BOSS slit, the spectra at lower redshift sample more central regions of the galaxies (typically within $< 1R_{\rm e}$, see Fig 5.1), where stellar populations are older. This naturally results in a slightly higher inferred age compared to higher-redshift observations, where a larger fraction of the galaxy light is included. Numerous studies, based on different data and methodologies, consistently support this picture indicating that the high-mass end of quiescent galaxies evolves passively over the last 8 Gyr. Indeed, Gallazzi et al. (2014) found a strong agreement between quiescent galaxies at $z \sim 0.7$ and local passive systems for $\log(M_*/\mathrm{M}_\odot) > 11.5$. Other works based on LEGA-C data (Beverage et al. 2023; Bevacqua et al. 2024), although limited to smaller samples, similarly found that the formation epochs of the most massive galaxies at LEGA-C redshifts are consistent with those inferred for local galaxies. Stacking analyses at different redshifts further confirm the passive evolution of high–mass quiescent galaxies (Choi et al. 2014).

Our measurements also reveal no significant evolution in the global stellar metallicity of the most massive quiescent galaxies from $z \sim 0.8$ to $z \sim 0.15$. This is consistent with Gallazzi et al. (2014), who found comparable metallicities for quiescent galaxies at $z \sim 0.7$ and in the local Universe. While the total stellar metallicity traces the overall metal content accumulated during star formation, the [Mg/Fe] abundance ratio provides the complementary information on the timescales of that enrichment. A key emerging result from both our results and simulations is that [Mg/Fe] shows little or no evolution across

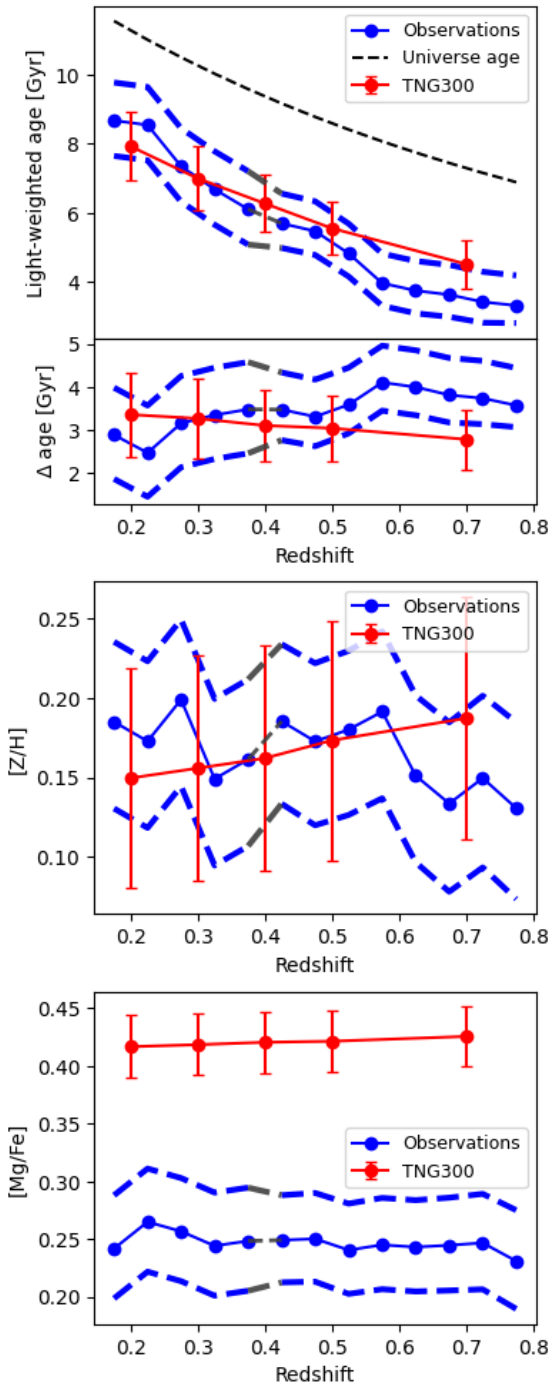

Figure 5.10: Evolution of the light-weighted age, [Z/H] and [Mg/Fe] in the redshift range $0.15 < z < 0.8$. The blue (orange) data points represent the median value in each redshift bin, the error bars represent the typical uncertainties of the DESI (BOSS) stacks, and the shaded regions correspond to the intrinsic scatter within each bin. The green data points and error bars are the median values and the dispersion of the stellar population parameters of the selected galaxies in five TNG300 snapshots. The dashed black line in the top panel represents the age of the Universe at each redshift.

cosmic time for massive quiescent galaxies. Choi et al. (2014) and Leethochawalit et al. (2019), analysing composite spectra of LRGs up to $z \sim 0.5$, find very weak or no evolution in [Mg/Fe] compared to the local Universe. Similarly, LEGA-C massive quiescent galaxies at $z \sim 0.7$ show [Mg/Fe] ratios comparable to those of local massive early-type systems (Beverage et al. 2021; Bevacqua et al. 2023). These results indicate that the most massive quiescent galaxies observed at $0.15 < z < 0.8$ had already completed their star formation by $z \gtrsim 1.5$–2. Their uniformly high [Mg/Fe] ratios across this redshift range suggest that both the galaxies observed at $z \sim 0.8$ and those at $z \sim 0.15$ formed and quenched their stars at similar early epochs, implying rapid formation timescales followed by passive evolution.

At higher redshift ($z \sim 1 - 1.3$), Carnall et al. (2019, 2022) reported slightly lower metallicities for galaxies with $\log(M_*/\mathrm{M}_\odot) > 11$, with an offset of $\sim 0.2 - 0.3$ dex below the local values. Their studies also found [Mg/Fe] ratios in massive quiescent galaxies comparable to those of local early-type systems, suggesting that the α-enhancement, and thus the short formation timescales, were already established by $z \sim 1$. However, their stellar metallicities are consistent with an earlier evolutionary stage of the passive population. Between $z \sim 1.3$ and $z \sim 0.8$, that correspond to around 2 Gyr of cosmic time, the number density of quiescent galaxies with $\log(M_*/\mathrm{M}_\odot) > 11.5$ increases by a factor of $\sim 4-5$ (Muzzin et al. 2013a). This implies that a large number of newly quenched systems joined the existing massive passive population during this period. These additions were likely slightly more metal-rich but shared similarly high [Mg/Fe] ratios, producing a mild apparent evolution in metallicity while maintaining a roughly constant α enhancement. This behaviour is indicative of a classical progenitor bias, where the growth of the quiescent population at lower redshift reflects the addition of recently quenched galaxies rather than the intrinsic evolution of the original passive systems. In contrast, from $z \sim 0.8$ to $z \sim 0.15$, despite 5 additional Gyr of elapsed time and an additional increase in number density by a factor of $3 - 4$ (e.g., Muzzin et al. 2013a; Donnari et al. 2021), the stellar population properties remain remarkably constant. This demonstrates that below $z \sim 0.8$ the progenitor bias is no longer significant, and the evolution of the massive quiescent population is genuinely passive. The galaxies added at later times were already largely quenched, having formed most of their stars at earlier epochs similarly to those already in place at $z \sim 0.8$. Their subsequent evolution likely involved dry mergers, which increased their stellar mass and size without significantly affecting the light-weighted age, global metallicity or [Mg/Fe] distribution. Consequently, while the build-up of the passive population between $z \sim 1.3$ and $z \sim 0.8$ is shaped by progenitor bias, at later times the most massive quiescent galaxies evolve truly passively, with structural growth dominating over further chemical or star-formation evolution.

5.5 Summary and conclusions

The analysis presented here provides the first homogeneous and continuous mapping of the stellar population properties of the most massive quiescent galaxies ($\log M_*/\mathrm{M}_\odot > 11.5$) across the last ~ 7 Gyr of cosmic time ($0.8 > z > 0.15$). This work has been made possible by the combination of the BOSS and DESI surveys, whose unprecedented spectral coverage and large sample size provide the foundation for our analysis. By applying a homogeneous selection across the two datasets we are able to trace the evolution of the most massive passive systems across a wide redshift range. Using an innovative full–index fitting technique, and consistently fitting the same set of spectral indices at all redshifts, we robustly measure physically meaningful trends of [Z/H], [Mg/Fe], and light–weighted age of the

most massive quiescent galaxies as continuous functions of redshift. This methodological homogeneity overcomes a common limitation in evolutionary studies, where results from different analyses, often based on distinct spectral indicators, are combined, introducing inconsistencies even when the underlying samples are comparable.

The resulting trends show no significant evolution in [Mg/Fe] and stellar metallicity, and an age increase fully consistent with passive stellar evolution. These results are robust against the choice of stellar population models and analysis assumptions, and they are in excellent agreement with the predictions from IllustrisTNG, which similarly predict negligible evolution in the chemical properties of the most massive quiescent galaxies at $z \leq 0.8$. Together, these findings demonstrate the remarkable chemical stability and constancy of the star-formation timescales of the high–mass quiescent population. Specifically, the observed variations in the redshift range $0.15 < z < 0.8$ (< 0.05 dex in [Z/H], < 0.02 dex in [Mg/Fe]) indicate that no more than about $10 - 15\%$ of the population can consist of newly quenched systems with distinct chemical histories. This implies that, below $z \sim 0.8$, the growth of the most massive quiescent galaxies is dominated by passive mass assembly through dry mergers rather than by the addition of freshly quenched stars.

Beyond confirming the qualitative expectations from previous snapshots and cosmological simulations, this work provides, for the first time, a quantitative characterisation of the passive–evolution regime in a way that was previously unattainable. Indeed, it provides a quantitative benchmark for the passive evolution of the most massive galaxies, offering a solid empirical basis for future comparisons with hydrodynamical simulations and chemical–enrichment models.

Chapter 6

Conclusions

In this thesis we have investigated the formation and evolution of galaxies as traced by their stellar populations, combining methodological innovation with a multi-scale observational approach. We developed and validated tools designed to extract physical information from spectroscopic data of varying quality and applied them to diverse galaxy samples, ranging from individual systems caught in the act of transformation to large surveys that trace population trends across cosmic time. The unifying theme throughout the thesis is the search for a consistent and physically meaningful description of how stellar populations encode the complex interplay between internal and environmental processes that regulate galaxy evolution.

In Chapter 2, we established a first, necessary, methodological step of the work by developing and validating a strategy to measure stellar population parameters from realistic survey-quality spectra. The chapter focused on testing the ability to recover ages and metallicities by combining optical and ultraviolet absorption-line indices, anticipating the data quality of forthcoming intermediate-redshift surveys such as WEAVE-StePS.

Through a comprehensive suite of simulated spectra, it demonstrated that a carefully chosen combination of blue and optical indices can successfully constrain stellar ages and metallicities, even at moderate S/N ratios typical of large spectroscopic programmes. This result is particularly relevant in the context of next-generation surveys, where observational efficiency and data uniformity are crucial. The work showed that leveraging the information carried by bluer spectral regions enables an accuracy comparable to that of traditional optical analyses, while also avoiding wavelength ranges heavily affected by atmospheric features. This provides an effective and practical recipe for extracting stellar population parameters from large galaxy samples at intermediate redshift, ensuring that surveys like WEAVE-StePS will be able to deliver robust measurements of stellar metallicity and age across thousands of galaxies.

Beyond its immediate application, this study laid the conceptual and technical foundation for the methodological development presented in the subsequent chapters of the thesis. Building on the groundwork described in Chapter 2, in Chapter 3 we introduced a more advanced and comprehensive analysis method, the Full-Index Fitting. This approach is specifically designed to exploit the full diagnostic potential of the absorption-line indices. Unlike classical index-based analyses, the FIF approach incorporates both the strength and the shape of absorption features within a unified Bayesian modeling, allowing a more complete and self-consistent extraction of stellar population parameters. We applied this

method to the Cartwheel galaxy, the archetypal collisional ring system that provides an exceptional case study for linking stellar population properties to the dynamical effects of an interaction. Using MUSE integral-field spectroscopy in combination with multi-wavelength photometry extending from GALEX to JWST, the analysis reconstructed the spatially resolved distribution of stellar ages and metallicities across the system. The results revealed a dominant intermediate-to-old stellar component in most of the disc, with a younger population confined to the outer ring, where recent star formation has been triggered by the outward-propagating collision wave.

This reconstruction offered a coherent picture of the recent evolution of the Cartwheel galaxy. The collision appears to have primarily affected the external regions, sweeping gas outwards and compressing it into the ring while leaving the inner disc largely undisturbed. The absence of young stellar populations in the inner ring and nucleus contrasts with some theoretical predictions of fallback-driven star formation, suggesting that the post-collision evolution of the Cartwheel is more stable and extended in time than previously thought.

From a broader perspective, in this Chapter we demonstrated how the FIF approach, combined with hierarchical Bayesian modelling, can link the fossil record of stellar populations to the dynamical histories in complex systems. It established the method's capability to recover spatially resolved stellar properties in a accurate and strongly reliable way and to connect them directly to physical processes.

In Chapter 4, we further develop our analysis method combining the FIF technique with photometric information. This joint spectro-photometric approach allowed the simultaneous use of the detailed information encoded in the absorption features and the broader constraints provided by galaxy spectral energy distributions. The method produced a more complete and physically robust view of stellar populations, capturing both the fine structure of spectra and the overall energy balance of galaxies. The study targeted the massive quiescent galaxies in the COSMOS Wall at $z \sim 0.73$, a well-characterised large-scale structure that includes a broad range of environments, from dense X-ray groups to the field. This setting provided an ideal context to explore how external conditions influence the quenching of massive galaxies during a key phase of cosmic evolution, when the global star-formation rate was rapidly declining. By combining LEGA-C spectroscopy with COSMOS2020 photometry, and analysing the data through nested sampling and hierarchical modelling, we derived consistent estimates of stellar ages, metallicities, and formation timescales, while quantifying intrinsic variations across different environments.

The results revealed a clear environmental hierarchy in the properties of massive quiescent galaxies. Densest, X-ray-detected groups host galaxies with the oldest stellar populations and the shortest star-formation timescales. Their stars formed rapidly and early, consistent with accelerated quenching driven by the hot intracluster medium, which likely removed or heated the remaining gas and suppressed further accretion and star formation. Galaxies in non–X-ray-detected groups showed intermediate characteristics, with older populations than those in the field but broader and more extended star-formation histories. This suggests that environmental mechanisms act more gradually in these systems, through repeated tidal interactions, mergers, or slow gas depletion. Field galaxies displayed the youngest stellar populations and the longest formation timescales, indicating quenching mainly regulated by internal processes such as gas exhaustion, feedback, or declining accretion. Altogether, these trends demonstrate that environment leaves a measurable imprint on the evolutionary paths of galaxies, even for massive galaxies. The COSMOS Wall analysis thus delivered one of the most detailed empirical characterisations of environmental quenching at intermediate redshift, demonstrating that the combination of internal processes and external environment governs the pace and efficiency of galaxy

evolution. Beyond the specific findings, we highlighted the power of the integrated spectro-photometric approach.

Building on the previous chapters, we extended in Chapter 5 our framework—tested on simulations, individual systems, and the COSMOS Wall sample, to a larger, more representative population of massive quiescent galaxies to trace their evolution across the last ~ 7 Gyr of cosmic history. Using the extensive spectroscopic datasets of the BOSS and DESI surveys, we focused on the most massive luminous red galaxies ($\log(M_*/\mathrm{M}_\odot) > 11.5$), which represent the most massive and passively evolving systems in the Universe. The uniform selection of the sample across the whole redshift range and the wide wavelength range covered by the galaxy spectra assure the ideal framework within which investigating how the stellar populations of the most massive quiescent galaxies have evolved since $z \sim 0.8$. The analysis adopted a homogeneous procedure across all the redshift bins, based on the FIF approach applied to the same set of spectral indices. This ensured methodological consistency and removed the inter-survey calibration offsets that have often limited previous evolutionary studies. By measuring stellar ages, metallicities, and [Mg/Fe] abundance ratios in a self-consistent way, we produced the first continuous and statistically robust mapping of the stellar population properties of high-mass end of quiescent galaxies across this broad redshift range.

The results revealed a strikingly uniform population. Both metallicity and [Mg/Fe] show no significant evolution with redshift, while stellar ages increase as expected from passive evolution. This implies that the chemical enrichment and star-formation histories of these galaxies were essentially completed by $z \sim 0.8$, and that their subsequent growth has been dominated by dry mergers—mass assembly without renewed star formation. The minimal variation in chemical properties places tight constraints on the fraction of newly quenched systems, confirming that late additions to the high-mass quiescent population chemically similar to the existing members. These results demonstrate that the most massive galaxies evolve almost exclusively through passive stellar ageing and minor structural growth, in excellent agreement with cosmological simulations such as IllustrisTNG. Beyond confirming theoretical expectations, the study quantifies the stability of this population with unprecedented precision, establishing a reference empirical benchmark for future comparisons with hydrodynamical and chemical-enrichment models. More broadly, in this Chapter we complete both our methodological development and the physical analysis of stellar populations at the core of this thesis. It demonstrates that the combination of consistent spectral analysis across surveys with a large, mass-complete galaxy sample can uncover genuine evolutionary trends with well-controlled and quantified systematics. The outcome is a coherent and data-driven picture of the most massive galaxies, demonstrating that their key stellar population properties have remained remarkably uniform over most of the recent cosmic history.

6.1 Future prospects

The path outlined by this thesis can certainly be further pursued, by applying the methods developed here and building upon the results achieved. Two complementary future directions could be:

- refining studies of integrated galaxy spectra over a broad wavelength range, both for individual systems and across a wider span of redshifts;
- extending the analysis to spatially resolved spectroscopy of galaxies over different epochs, to investigate the gradients in their stellar population properties.

These two directions share the same goal of connecting the physical mechanisms that shape galaxies across different scales, environments, and cosmic epochs.

The upcoming wide-field spectroscopic surveys will likely drive progress along the first of these research directions. Projects such as WEAVE-StePS, 4MOST-StePS, 4MOST-WAVES, and MOONRISE will deliver high-quality spectra for thousands of galaxies covering a wide range of stellar masses, morphologies, and environments. The already developed Bayesian tools for spectro-photometric analysis, when applied to these forthcoming datasets, which combine wide wavelength coverage, depth, and homogeneity across a large redshift range, will enable detailed measurements of stellar ages, metallicities, and abundance ratios for individual galaxies. This will enable a step forward beyond population averages and the investigation of the intrinsic diversity of stellar populations as a function of galaxy mass, structure, and environment. This will allow us to study how star-formation timescales and chemical enrichment depend on these parameters, and how they evolve with cosmic time. In particular, MOONRISE will extend these measurements to $z \geq 1$, directly probing galaxies when approach the quenching phase. This will provide a bridge between the massive passive galaxies studied in this thesis and their younger counterparts at earlier epochs. By combining the statistical power of large surveys with the methodological consistency developed here, a coherent picture of how galaxies assembled and stopped forming stars during the last ~ 10 Gyr can be constructed.

In parallel, future works can focus on spatially resolved analyses of galaxies from intermediate to high redshift. A possible step in this direction is to exploit the already available JWST spectroscopic data of high-redshift galaxies, as well as ESO archive and large programmes using the KMOS instrument at VLT (e.g. EMPOWER), to open a new window on galaxy quenching and structural interaction during the crucial stages of cosmic star formation. In particular, EMPOWER will provide deep integral-field spectroscopy of galaxies at $0.7 < z < 2.3$, covering a wide range of environments from the field to massive clusters. JWST adds the unique capability to resolve the stellar populations of quiescent galaxies at $z \geq 1.5$ with unprecedented spatial detail and sensitivity. By combining these datasets, it will be possible to trace how galaxies quench as a function of time, mass, and environment, following the transition from star-forming to passive systems across the full quenching sequence.

The innovative and advanced techniques developed during my PhD can be employed to measure spatial gradients of age, metallicity, and abundance ratios in these galaxies. These gradients provide a direct signature of the physical mechanisms at work. Comparison between observed trends and predictions from hydrodynamical simulations, such as IllustrisTNG and SIMBA, will help to identify which processes dominate at different epochs and in different environments, from AGN feedback and gas compaction to environmental stripping and strangulation. These analyses will connect the internal structure of high-redshift galaxies with the integrated properties of their descendants at lower redshift. Combining the statistical strength of large surveys with the physical detail of spatially resolved observations will allow to reconstruct the full evolutionary path of massive galaxies, linking the processes that govern their formation, chemical enrichment, and quenching.

Ultimately, these two complementary approaches leverage both integrated analyses from next-generation surveys and spatially resolved studies with JWST and EMPOWER, offering the opportunity to move toward a unified picture of galaxy evolution. Taken together, these approaches can enable a detailed reconstruction of how galaxies assembled their stars and transformed their structures across cosmic time, linking the fossil record of stellar populations to the dynamical and environmental mechanisms that shaped them.

Bibliography

Alberts, S., Williams, C. C., Helton, J. M., et al. 2024, ApJ, 975, 85

Amram, P., Mendes de Oliveira, C., Boulesteix, J., & Balkowski, C. 1998, A&A, 330, 881

Antwi-Danso, J., Papovich, C., Leja, J., et al. 2023, ApJ, 943, 166

Aringer, B., Girardi, L., Nowotny, W., Marigo, P., & Lederer, M. T. 2009, A&A, 503, 913

Athanassoula, E. & Bosma, A. 1985, ARA&A, 23, 147

Bacon, R., Accardo, M., Adjali, L., et al. 2010, in Ground-based and Airborne Instrumentation for Astronomy III, Vol. 7735, SPIE, 131–139

Baldry, I. K., Balogh, M. L., Bower, R. G., et al. 2006, MNRAS, 373, 469

Baldry, I. K., Glazebrook, K., Brinkmann, J., et al. 2004, ApJ, 600, 681

Baldwin, J. A., Phillips, M. M., & Terlevich, R. 1981, PASP, 93, 5

Balogh, M. L., Morris, S. L., Yee, H., Carlberg, R., & Ellingson, E. 1999, The Astrophysical Journal, 527, 54

Balogh, M. L., Navarro, J. F., & Morris, S. L. 2000, ApJ, 540, 113

Bamford, S. P., Nichol, R. C., Baldry, I. K., et al. 2009, MNRAS, 393, 1324

Bastian, N., Covey, K. R., & Meyer, M. R. 2010, ARA&A, 48, 339

Belfiore, F., Maiolino, R., Maraston, C., et al. 2016, MNRAS, 461, 3111

Bell, E. F., Wolf, C., Meisenheimer, K., et al. 2004, ApJ, 608, 752

Bennett, C., Larson, D., Weiland, J., & Hinshaw, G. 2014, The Astrophysical Journal, 794, 135

Bernardi, M., Shankar, F., Hyde, J. B., et al. 2010, MNRAS, 404, 2087

Bevacqua, D., Saracco, P., Boecker, A., et al. 2024, A&A, 690, A150

Bevacqua, D., Saracco, P., La Barbera, F., et al. 2023, MNRAS, 525, 4219

Bevacqua, D., Saracco, P., La Barbera, F., et al. 2025, A&A, 699, A203

Beverage, A. G., Kriek, M., Conroy, C., et al. 2021, ApJ, 917, L1

Beverage, A. G., Kriek, M., Conroy, C., et al. 2023, ApJ, 948, 140

Blanton, M. R. & Moustakas, J. 2009, ARA&A, 47, 159

Boardman, N. F., Weijmans, A.-M., van den Bosch, R., et al. 2017, Monthly Notices of the Royal Astronomical Society, 471, 4005

Borghi, N., Moresco, M., Cimatti, A., et al. 2022, ApJ, 927, 164

Boselli, A. & Gavazzi, G. 2006, PASP, 118, 517

Bower, G. C., Goss, W. M., Falcke, H., Backer, D. C., & Lithwick, Y. 2006, ApJ, 648, L127

Brammer, G. B., Whitaker, K. E., van Dokkum, P. G., et al. 2009, ApJ, 706, L173

Bruzual, G. & Charlot, S. 2003, Monthly Notices of the Royal Astronomical Society, 344, 1000

Buchner, J. 2016, Statistics and Computing, 26, 383

Buchner, J. 2019, PASP, 131, 108005

Buchner, J. 2021, The Journal of Open Source Software, 6, 3001

Burstein, D., Faber, S. M., Gaskell, C. M., & Krumm, N. 1984, ApJ, 287, 586

Byler, N., Dalcanton, J. J., Conroy, C., & Johnson, B. D. 2017, The Astrophysical Journal, 840, 44

Calabrò, A., Guaita, L., Pentericci, L., et al. 2022, A&A, 664, A75

Calzetti, D. 2001, PASP, 113, 1449

Cappellari, M. 2017, Monthly Notices of the Royal Astronomical Society, 466, 798

Cappellari, M. 2022, arXiv preprint arXiv:2208.14974

Cappellari, M. 2023, MNRAS, 526, 3273

Cappellari, M. & Emsellem, E. 2004, Publications of the Astronomical Society of the Pacific, 116, 138

Carnall, A. C., Cullen, F., McLure, R. J., et al. 2024, MNRAS, 534, 325

Carnall, A. C., McLure, R. J., Dunlop, J. S., et al. 2019, MNRAS, 490, 417

Carnall, A. C., McLure, R. J., Dunlop, J. S., & Davé, R. 2018, MNRAS, 480, 4379

Carnall, A. C., McLure, R. J., Dunlop, J. S., et al. 2022, ApJ, 929, 131

Cassarà, L. P., Piovan, L., Weiss, A., Salaris, M., & Chiosi, C. 2013, Monthly Notices of the Royal Astronomical Society, 436, 2824

Cassisi, S., Castellani, M., & Castellani, V. 1997, A&A, 317, 108

Cenarro, A. J., Cardiel, N., Gorgas, J., et al. 2001, MNRAS, 326, 959

Cervantes, J. & Vazdekis, A. 2009, Monthly Notices of the Royal Astronomical Society, 392, 691

Chabrier, G. 2003, Publications of the Astronomical Society of the Pacific, 115, 763

Charlot, S. & Fall, S. M. 2000, The Astrophysical Journal, 539, 718

Charlot, S. & Longhetti, M. 2001, Monthly Notices of the Royal Astronomical Society, 323, 887

Chauke, P., van der Wel, A., Pacifici, C., et al. 2018, The Astrophysical Journal, 861, 13

Chavez, M., Bertone, E., Buzzoni, A., et al. 2007, The Astrophysical Journal, 657, 1046

Chen, Y., Bressan, A., Girardi, L., et al. 2015, Monthly Notices of the Royal Astronomical Society, 452, 1068

Choi, J., Conroy, C., Moustakas, J., et al. 2014, The Astrophysical Journal, 792, 95

Citro, A., Pozzetti, L., Moresco, M., & Cimatti, A. 2016, A&A, 592, A19

Coil, A. L., Blanton, M. R., Burles, S. M., et al. 2011, ApJ, 741, 8

Comparat, J., Richard, J., Kneib, J.-P., et al. 2015, A&A, 575, A40

Conroy, C. 2013, arXiv preprint arXiv:1301.7095

Cooper, M. C., Newman, J. A., Croton, D. J., et al. 2006, MNRAS, 370, 198

Corcho-Caballero, P., Ascasibar, Y., & Scannapieco, C. 2021, Monthly Notices of the Royal Astronomical Society, 506, 5108

Costantin, L., Gillman, S., Boogaard, L. A., et al. 2025, A&A, 699, A360

Costantin, L., Iovino, A., Zibetti, S., et al. 2019, Astronomy & Astrophysics, 632, A9

Croton, D. J., Springel, V., White, S. D. M., et al. 2006, MNRAS, 365, 11

Cucciati, O., Iovino, A., Marinoni, C., et al. 2006, A&A, 458, 39

Curti, M., Cresci, G., Mannucci, F., et al. 2017, Monthly Notices of the Royal Astronomical Society, 465, 1384–1400

Daddi, E., Renzini, A., Pirzkal, N., et al. 2005, The Astrophysical Journal, 626, 680

Dalton, G., Trager, S. C., Abrams, D. C., et al. 2012, in Ground-based and Airborne Instrumentation for Astronomy IV, Vol. 8446, SPIE, 220–231

Darvish, B., Mobasher, B., Martin, D. C., et al. 2017, ApJ, 837, 16

Darvish, B., Mobasher, B., Sobral, D., et al. 2016, ApJ, 825, 113

Davis, M. & Geller, M. J. 1976, ApJ, 208, 13

Dawson, K. S., Schlegel, D. J., Ahn, C. P., et al. 2013, AJ, 145, 10

de Jong, R. S., Agertz, O., Berbel, A. A., et al. 2019, The Messenger, 175, 3

de Vaucouleurs, G. 1959, Handbuch der Physik, 53, 275

Dekel, A. & Birnboim, Y. 2004, AIP Conference Proceedings, 743, 162

Dekel, A., Birnboim, Y., Engel, G., et al. 2009, Nature, 457, 451

DESI Collaboration, Abdul-Karim, M., Adame, A. G., et al. 2025, arXiv e-prints, arXiv:2503.14745

Dicke, R. H., Peebles, P. J. E., Roll, P. G., & Wilkinson, D. T. 1965, ApJ, 142, 414

Ditrani, F. R., Longhetti, M., Fossati, M., & Wolter, A. 2024, A&A, 688, A89

Ditrani, F. R., Longhetti, M., Iovino, A., et al. 2025, A&A, 696, A116

Donnari, M., Pillepich, A., Nelson, D., et al. 2021, MNRAS, 506, 4760

Donnari, M., Pillepich, A., Nelson, D., et al. 2019, MNRAS, 485, 4817

Dressler, A. 1980, ApJ, 236, 351

Dressler, A., Oemler, Jr., A., Couch, W. J., et al. 1997, ApJ, 490, 577

Driver, S. P., Robotham, A. S. G., Bland-Hawthorn, J., et al. 2013, MNRAS, 430, 2622

Eftekhari, E., La Barbera, F., Vazdekis, A., Allende Prieto, C., & Knowles, A. T. 2022, Monthly Notices of the Royal Astronomical Society, 512, 378

Eisenstein, D. J., Annis, J., Gunn, J. E., et al. 2001, AJ, 122, 2267

Eisenstein, D. J., Weinberg, D. H., Agol, E., et al. 2011, AJ, 142, 72

Erfanianfar, G., Popesso, P., Finoguenov, A., et al. 2016, MNRAS, 455, 2839

Falcón-Barroso, J., Sánchez-Blázquez, P., Vazdekis, A., et al. 2011, Astronomy & Astrophysics, 532, A95

Fanelli, M. N., O'Connell, R. W., Burstein, D., & Wu, C.-C. 1992, The Astrophysical Journal Supplement Series, 82, 197

Favole, G., Montero-Dorta, A. D., Prada, F., Rodríguez-Torres, S. A., & Schlegel, D. J. 2018, MNRAS, 480, 1415

Feroz, F., Hobson, M., & Bridges, M. 2009, Monthly Notices of the Royal Astronomical Society, 398, 1601

Feroz, F. & Hobson, M. P. 2008, Monthly Notices of the Royal Astronomical Society, 384, 449

Feroz, F., Hobson, M. P., Cameron, E., & Pettitt, A. N. 2019, The Open Journal of Astrophysics, 2, 10

Ferreras, I., Hopkins, A. M., Gunawardhana, M. L. P., et al. 2017, MNRAS, 468, 607

Ferreras, I., Pasquali, A., Malhotra, S., et al. 2009, The Astrophysical Journal, 706, 158

Ferré-Mateu, A., Sanchez-Blazquez, P., Vazdekis, A., & De la Rosa, I. G. 2014, The Astrophysical Journal, 797, 136

Forrest, B., Marsan, Z. C., Annunziatella, M., et al. 2020, ApJ, 903, 47

Fossati, M., Fumagalli, M., Boselli, A., et al. 2016, Monthly Notices of the Royal Astronomical Society, 455, 2028

Fossati, M., Fumagalli, M., Gavazzi, G., et al. 2019, MNRAS, 484, 2212

Fossati, M., Mendel, J., Boselli, A., et al. 2018, Astronomy & Astrophysics, 614, A57

Fossati, M., Wilman, D. J., Mendel, J. T., et al. 2017, ApJ, 835, 153

Gallazzi, A., Bell, E. F., Zibetti, S., Brinchmann, J., & Kelson, D. D. 2014, ApJ, 788, 72

Gallazzi, A., Bell, E. F., Zibetti, S., Brinchmann, J., & Kelson, D. D. 2014, The Astrophysical Journal, 788, 72

Gallazzi, A., Charlot, S., Brinchmann, J., White, S. D., & Tremonti, C. A. 2005, Monthly Notices of the Royal Astronomical Society, 362, 41

Gallazzi, A. R., Pasquali, A., Zibetti, S., & Barbera, F. L. 2021, Monthly Notices of the Royal Astronomical Society, 502, 4457

Gavazzi, G., Consolandi, G., Dotti, M., et al. 2015, A&A, 580, A116

Genzel, R., Tacconi, L. J., Lutz, D., et al. 2015, ApJ, 800, 20

George, M. R., Leauthaud, A., Bundy, K., et al. 2011, ApJ, 742, 125

Gilks, W. R. 2005, Encyclopedia of biostatistics, 4

Giocoli, C., Tormen, G., Sheth, R. K., & van den Bosch, F. C. 2010, MNRAS, 404, 502

Giovanelli, R. & Haynes, M. P. 1985, ApJ, 292, 404

González-Lópezlira, R. A., Bruzual-A., G., Charlot, S., Ballesteros-Paredes, J., & Loinard, L. 2010, MNRAS, 403, 1213

Gozaliasl, G., Finoguenov, A., Tanaka, M., et al. 2019, MNRAS, 483, 3545

Graves, G. J., Faber, S. M., & Schiavon, R. P. 2009, ApJ, 693, 486

Gregg, M. D. 1994, The Astronomical Journal, 108, 2164

Guglielmo, V., Poggianti, B. M., Moretti, A., et al. 2015, MNRAS, 450, 2749

Gunn, J. E. & Gott, J. Richard, I. 1972, ApJ, 176, 1

Haynes, M. P. & Giovanelli, R. 1984, AJ, 89, 758

Hernquist, L. & Weil, M. L. 1993, MNRAS, 261, 804

Higdon, J. L. 1996, ApJ, 467, 241

Hopkins, P. F., Cox, T. J., Hernquist, L., et al. 2013, MNRAS, 430, 1901

Hopkins, P. F., Hernquist, L., Cox, T. J., et al. 2006, ApJS, 163, 1

Horellou, C. & Combes, F. 2001, Ap&SS, 276, 1141

Hubble, E. P. 1936, Realm of the Nebulae

Iovino, A. 2002, AJ, 124, 2471

Iovino, A., Cucciati, O., Scodeggio, M., et al. 2010, A&A, 509, A40

Iovino, A., Mercurio, A., Gallazzi, A. R., et al. 2023a, The Messenger, 190, 22

Iovino, A., Petropoulou, V., Scodeggio, M., et al. 2016, A&A, 592, A78

Iovino, A., Poggianti, B. M., Mercurio, A., et al. 2023b, A&A, 672, A87

Jin, S., Trager, S. C., Dalton, G. B., et al. 2023, Monthly Notices of the Royal Astronomical Society, stad557

Johnson, B. D., Leja, J., Conroy, C., & Speagle, J. S. 2021, ApJS, 254, 22

Jørgensen, I., Bergmann, M., Davies, R., et al. 2005, The Astronomical Journal, 129, 1249

Jørgensen, I. & Chiboucas, K. 2013, The Astronomical Journal, 145, 77

Kannappan, S. J. 2004, ApJ, 611, L89

Kauffmann, G., Heckman, T. M., Tremonti, C., et al. 2003, MNRAS, 346, 1055

Kaushal, Y., Nersesian, A., Bezanson, R., et al. 2024, ApJ, 961, 118

Kennicutt, Robert C., J. 1998, ARA&A, 36, 189

Kewley, L. J., Dopita, M. A., Sutherland, R. S., Heisler, C. A., & Trevena, J. 2001, ApJ, 556, 121

Kewley, L. J., Groves, B., Kauffmann, G., & Heckman, T. 2006, MNRAS, 372, 961

Kimmig, L. C., Remus, R.-S., Seidel, B., et al. 2025, ApJ, 979, 15

Knowles, A. T., Sansom, A. E., Vazdekis, A., & Allende Prieto, C. 2023, MNRAS, 523, 3450

Kroupa, P. 2001, MNRAS, 322, 231

Kroupa, P. & Jerabkova, T. 2019, Nature Astronomy, 3, 482

Kroupa, P., Weidner, C., Pflamm-Altenburg, J., et al. 2013, in Planets, Stars and Stellar Systems. Volume 5: Galactic Structure and Stellar Populations, ed. T. D. Oswalt & G. Gilmore, Vol. 5, 115

Kuijken, K. et al. 2011, The Messenger, 146

La Barbera, F., Ferreras, I., Vazdekis, A., et al. 2013, Monthly Notices of the Royal Astronomical Society, 433, 3017

La Barbera, F., Vazdekis, A., Ferreras, I., et al. 2017, Monthly Notices of the Royal Astronomical Society, 464, 3597

Labbé, I., Huang, J., Franx, M., et al. 2005, ApJ, 624, L81

Lanz, T. & Hubeny, I. 2003a, ApJS, 146, 417

Lanz, T. & Hubeny, I. 2003b, ApJS, 147, 225

Lanz, T. & Hubeny, I. 2007, ApJS, 169, 83

Larson, R. B., Tinsley, B. M., & Caldwell, C. N. 1980, ApJ, 237, 692

Le Cras, C., Maraston, C., Thomas, D., & York, D. G. 2016, Monthly Notices of the Royal Astronomical Society, 461, 766

Leauthaud, A., Bundy, K., Saito, S., et al. 2016, MNRAS, 457, 4021

Leethochawalit, N., Kirby, E. N., Ellis, R. S., Moran, S. M., & Treu, T. 2019, ApJ, 885, 100

Lilly, S. J., Carollo, C. M., Pipino, A., Renzini, A., & Peng, Y. 2013, ApJ, 772, 119

Lilly, S. J., Le Fèvre, O., Renzini, A., et al. 2007, ApJ Supplement Series, 172, 70

Longhetti, M., Bressan, A., Chiosi, C., & Rampazzo, R. 2000, Astronomy and Astrophysics, 353, 917

Longhetti, M. & Saracco, P. 2009, MNRAS, 394, 774

Lonoce, I., Maraston, C., Thomas, D., et al. 2020, Monthly Notices of the Royal Astronomical Society, 492, 326

López Fernández, R., Cid Fernandes, R., González Delgado, R. M., et al. 2016, Monthly Notices of the Royal Astronomical Society, 458, 184

Lynds, R. & Toomre, A. 1976, ApJ, 209, 382

Madau, P. & Dickinson, M. 2014, ARA&A, 52, 415

Madau, P., Ferguson, H. C., Dickinson, M. E., et al. 1996, MNRAS, 283, 1388

Mannucci, F., Cresci, G., Maiolino, R., Marconi, A., & Gnerucci, A. 2010, MNRAS, 408, 2115

Mapelli, M., Moore, B., Giordano, L., et al. 2008a, MNRAS, 383, 230

Mapelli, M., Moore, B., Ripamonti, E., et al. 2008b, MNRAS, 383, 1223

Maraston, C., Colmenárez, L. N., Bender, R., & Thomas, D. 2009, Astronomy & Astrophysics, 493, 425

Maraston, C., Daddi, E., Renzini, A., et al. 2006, The Astrophysical Journal, 652, 85

Maraston, C., Pforr, J., Henriques, B. M., et al. 2013, MNRAS, 435, 2764

Marigo, P., Bressan, A., Nanni, A., Girardi, L., & Pumo, M. L. 2013, Monthly Notices of the Royal Astronomical Society, 434, 488

Martin, D. C., Fanson, J., Schiminovich, D., et al. 2005, The Astrophysical Journal, 619, L1

Martín-Navarro, I., Lyubenova, M., van de Ven, G., et al. 2019, Astronomy & Astrophysics, 626, A124

Martín-Navarro, I., Pérez-González, P. G., Trujillo, I., et al. 2014, The Astrophysical Journal Letters, 798, L4

Martín-Navarro, I., Pinna, F., Coccato, L., et al. 2021, A&A, 654, A59

Martín-Navarro, I., Spiniello, C., Tortora, C., et al. 2023, MNRAS, 521, 1408

Martins, L. P., Delgado, R. M. G., Leitherer, C., Cervino, M., & Hauschildt, P. 2005, Monthly Notices of the Royal Astronomical Society, 358, 49

Maseda, M. V., van der Wel, A., Franx, M., et al. 2021, ApJ, 923, 18

Matteucci, F. & Tornambe, A. 1987, A&A, 185, 51

Mayya, Y. D., Barway, S., Gómez-González, V. M. A., & Zaragoza-Cardiel, J. 2024, MNRAS, 527, 2816

Mayya, Y. D., Plat, A., Gómez-González, V. M. A., et al. 2023, MNRAS, 519, 5492

Merritt, D. 1984, ApJ, 276, 26

Mihos, J. C. & Hernquist, L. 1994, ApJ, 437, 611

Moore, B., Lake, G., & Katz, N. 1998, ApJ, 495, 139

Muzzin, A., Marchesini, D., Stefanon, M., et al. 2013a, ApJ, 777, 18

Muzzin, A., Marchesini, D., Stefanon, M., et al. 2013b, ApJS, 206, 8

Naiman, J. P., Pillepich, A., Springel, V., et al. 2018, MNRAS, 477, 1206

Nelson, D., Springel, V., Pillepich, A., et al. 2019, Computational Astrophysics and Cosmology, 6, 2

Nenkova, M., Ivezić, Ž., & Elitzur, M. 2000, in Astronomical Society of the Pacific Conference Series, Vol. 196, Thermal Emission Spectroscopy and Analysis of Dust, Disks, and Regoliths, ed. M. L. Sitko, A. L. Sprague, & D. K. Lynch, 77–82

Oemler, Augustus, J. 1974, ApJ, 194, 1

Oke, J. B. 1974, The Astrophysical Journal Supplement Series, 27, 21

Osterbrock, D. E. 1989, Astrophysics of gaseous nebulae and active galactic nuclei

Pandey, B. & Sarkar, S. 2017, MNRAS, 467, L6

Parikh, T., Thomas, D., Maraston, C., et al. 2021, MNRAS, 502, 5508

Peebles, P. J. E. 1974, ApJ, 189, L51

Peebles, P. J. E. 1980, The large-scale structure of the universe

Peebles, P. J. E. & Dicke, R. H. 1968, ApJ, 154, 891

Peebles, P. J. E. & Yu, J. T. 1970, ApJ, 162, 815

Peng, Y.-j., Lilly, S. J., Kovač, K., et al. 2010, ApJ, 721, 193

Penzias, A. A. & Wilson, R. W. 1965, ApJ, 142, 419

Pietrinferni, A., Cassisi, S., Salaris, M., & Castelli, F. 2004, The Astrophysical Journal, 612, 168

Pietrinferni, A., Cassisi, S., Salaris, M., & Castelli, F. 2006, The Astrophysical Journal, 642, 797

Pillepich, A., Springel, V., Nelson, D., et al. 2018, MNRAS, 473, 4077

Pilyugin, L. S. & Grebel, E. K. 2016, MNRAS, 457, 3678

Planck Collaboration, Ade, P. A. R., Aghanim, N., et al. 2016, A&A, 594, A13

Plat, A., Charlot, S., Bruzual, G., et al. 2019, Monthly Notices of the Royal Astronomical Society, 490, 978

Poggianti, B. M., Aragón-Salamanca, A., Zaritsky, D., et al. 2009, ApJ, 693, 112

Poggianti, B. M., Calvi, R., Bindoni, D., et al. 2013, ApJ, 762, 77

Poggianti, B. M., von der Linden, A., De Lucia, G., et al. 2006, ApJ, 642, 188

Postman, M. & Geller, M. J. 1984, ApJ, 281, 95

Renaud, F., Athanassoula, E., Amram, P., et al. 2018, MNRAS, 473, 585

Renzini, A. 2006, ARA&A, 44, 141

Rodighiero, G., Daddi, E., Baronchelli, I., et al. 2011, ApJ, 739, L40

Salpeter, E. E. 1955, ApJ, 121, 161

Salvador-Rusiñol, N., Beasley, M. A., Vazdekis, A., & Barbera, F. L. 2021, Monthly Notices of the Royal Astronomical Society, 500, 3368

Salvador-Rusiñol, N., Ferré-Mateu, A., Vazdekis, A., & Beasley, M. A. 2022, Monthly Notices of the Royal Astronomical Society, 515, 4514

Salvador-Rusiñol, N., Vazdekis, A., La Barbera, F., et al. 2020, Nature Astronomy, 4, 252

Salvaggio, C., Wolter, A., Belfiore, A., & Colpi, M. 2023, MNRAS, 522, 1377

Sánchez, S., Barrera-Ballesteros, J., Lacerda, E., et al. 2022, The Astrophysical Journal Supplement Series, 262, 36

Sánchez, S., Kennicutt, R., De Paz, A. G., et al. 2012, Astronomy & Astrophysics, 538, A8

Sánchez-Blázquez, P., Jablonka, P., Noll, S., et al. 2009, Astronomy & Astrophysics, 499, 47

Sánchez-Blázquez, P., Peletier, R., Jiménez-Vicente, J., et al. 2006, Monthly Notices of the Royal Astronomical Society, 371, 703

Sandage, A. 1986, Astronomy and Astrophysics, 161, 89

Santucci, G., Brough, S., Scott, N., et al. 2020, ApJ, 896, 75

Sargent, M. T., Béthermin, M., Daddi, E., & Elbaz, D. 2012, ApJ, 747, L31

Sarzi, M., Iodice, E., Coccato, L., et al. 2018, Astronomy & Astrophysics, 616, A121

Schawinski, K., Urry, C. M., Simmons, B. D., et al. 2014, MNRAS, 440, 889

Schmidt, M. 1959, ApJ, 129, 243

Scoville, N., Aussel, H., Benson, A., et al. 2007, ApJS, 172, 150

Shapley, A. E., Steidel, C. C., Erb, D. K., et al. 2005, ApJ, 626, 698

Skibba, R. A., Bamford, S. P., Nichol, R. C., et al. 2009, MNRAS, 399, 966

Smith, R. J. 2020, ARA&A, 58, 577

Smith, R. J., Lucey, J. R., & Hudson, M. J. 2009, MNRAS, 400, 1690

Smoot, G. F., Bennett, C. L., Kogut, A., et al. 1992, ApJ, 396, L1

Sobral, D., van der Wel, A., Bezanson, R., et al. 2022, ApJ, 926, 117

Spiniello, C., Trager, S., Koopmans, L. V., & Conroy, C. 2014, Monthly Notices of the Royal Astronomical Society, 438, 1483

Spitzer, Lyman, J. & Baade, W. 1951, ApJ, 113, 413

Springel, V., Pakmor, R., Pillepich, A., et al. 2018, MNRAS, 475, 676

Storey, P. J. & Zeippen, C. J. 2000, MNRAS, 312, 813

Straatman, C. M., van der Wel, A., Bezanson, R., et al. 2018, The Astrophysical Journal Supplement Series, 239, 27

Strateva, I., Ivezić, Ž., Knapp, G. R., et al. 2001, AJ, 122, 1861

Struck, C., Appleton, P. N., Borne, K. D., & Lucas, R. A. 1996, AJ, 112, 1868

Tacconi, L. J., Neri, R., Genzel, R., et al. 2013, ApJ, 768, 74

Theys, J. C. & Spiegel, E. A. 1977, ApJ, 212, 616

Thomas, D., Greggio, L., & Bender, R. 1999, MNRAS, 302, 537

Thomas, D., Maraston, C., Bender, R., & De Oliveira, C. M. 2005, The Astrophysical Journal, 621, 673

Thomas, D., Maraston, C., & Johansson, J. 2011, MNRAS, 412, 2183

Thomas, D., Maraston, C., Schawinski, K., Sarzi, M., & Silk, J. 2010, MNRAS, 404, 1775

Thomas, D., Maraston, C., Schawinski, K., Sarzi, M., & Silk, J. 2010, Monthly Notices of the Royal Astronomical Society, 404, 1775

Tonnesen, S., Bryan, G. L., & van Gorkom, J. H. 2007, ApJ, 671, 1434

Toomre, A. 1977, in Evolution of Galaxies and Stellar Populations, ed. B. M. Tinsley & R. B. G. Larson, D. Campbell, 401

Trager, S., Faber, S., Worthey, G., & González, J. J. 2000, The Astronomical Journal, 120, 165

Valdes, F., Gupta, R., Rose, J. A., Singh, H. P., & Bell, D. J. 2004, ApJS, 152, 251

van der Wel, A. 2008, ApJ, 675, L13

van der Wel, A., Bezanson, R., D'Eugenio, F., et al. 2021, The Astrophysical Journal Supplement Series, 256, 44

van der Wel, A., Noeske, K., Bezanson, R., et al. 2016, The Astrophysical Journal Supplement Series, 223, 29

Vazdekis, A., Coelho, P., Cassisi, S., et al. 2015, Monthly Notices of the Royal Astronomical Society, 449, 1177

Vazdekis, A., Koleva, M., Ricciardelli, E., Röck, B., & Falcón-Barroso, J. 2016, Monthly Notices of the Royal Astronomical Society, 463, 3409

Villaume, A., Conroy, C., Johnson, B., et al. 2017, ApJS, 230, 23

Weaver, J. R., Kauffmann, O. B., Ilbert, O., et al. 2022, ApJS, 258, 11

Weiner, B. J., Phillips, A. C., Faber, S. M., et al. 2005, ApJ, 620, 595

Werle, A., Poggianti, B., Moretti, A., et al. 2022, ApJ, 930, 43

Westera, P., Lejeune, T., Buser, R., Cuisinier, F., & Bruzual, G. 2002, A&A, 381, 524

Whitaker, K. E., Franx, M., Leja, J., et al. 2014, ApJ, 795, 104

Whitaker, K. E., van Dokkum, P. G., Brammer, G., & Franx, M. 2012, ApJ, 754, L29

Whitaker, K. E., van Dokkum, P. G., Brammer, G., et al. 2013, ApJ, 770, L39

White, S. D. M. & Rees, M. J. 1978, MNRAS, 183, 341

Wilkinson, D. M., Maraston, C., Goddard, D., Thomas, D., & Parikh, T. 2017, MNRAS, 472, 4297

Williams, R. J., Quadri, R. F., Franx, M., van Dokkum, P., & Labbé, I. 2009, ApJ, 691, 1879

Wilman, D. J., Fontanot, F., De Lucia, G., Erwin, P., & Monaco, P. 2013, MNRAS, 433, 2986

Worthey, G. 1994, ApJS, 95, 107

Worthey, G., Faber, S., Gonzalez, J. J., & Burstein, D. 1994, The Astrophysical Journal Supplement Series, 94, 687

Worthey, G. & Ottaviani, D. 1997, The Astrophysical Journal Supplement Series, 111, 377

Wright, E. L. 2006, Publications of the Astronomical Society of the Pacific, 118, 1711

Wuyts, S., Labbé, I., Franx, M., et al. 2007, ApJ, 655, 51

York, D. G., Adelman, J., Anderson Jr, J. E., et al. 2000, The Astronomical Journal, 120, 1579

Zaragoza-Cardiel, J., Gómez-González, V. M. A., Mayya, D., & Ramos-Larios, G. 2022, Monthly Notices of the Royal Astronomical Society, 514, 1689

Zhou, R., Dey, B., Newman, J. A., et al. 2023, AJ, 165, 58

Zhou, R., Newman, J. A., Dawson, K. S., et al. 2020, Research Notes of the American Astronomical Society, 4, 181

Zhou, S., Iovino, A., Longhetti, M., et al. 2025, A&A, submitted

Zibetti, S., Gallazzi, A. R., Ascasibar, Y., et al. 2017, Monthly Notices of the Royal Astronomical Society, 468, 1902

Zibetti, S., Gallazzi, A. R., Hirschmann, M., et al. 2020, MNRAS, 491, 3562

Chapter A

Appendix to Chapter 2

A.1 α-enhancement

Our analysis relies on stellar population models constructed with stars having the same abundance pattern as in the solar neighbourhood. Since massive galaxies are over-abundant in several elements (e.g. [α/Fe]), we estimate the possible impact of [α/Fe] on metallicity estimates by adding the [α/Fe] information on the simulated spectra, while the comparison library remains unaltered. We consider the most extreme case of [α/Fe]=0.4, which is typical of the most massive galaxies in the nearby Universe. We added the [α/Fe] information in a differential way, by measuring the indices used in this work on [α/Fe] = 0.4 and [α/Fe] = 0 templates and then we subtract the values of the [α/Fe] = 0 indices to the ones at [α/Fe] = 0.4, in order to obtain the differential offset caused by the α/Fe. The differential offset is added on the indices values of the WEAVE-StePS-like simulations. For the UV part (below 3500Å) we used the E-MILES preliminary models (see Eftekhari et al. 2022) calculated with Teramo isochrones, age values between 4 and 10 Gyr, metallicity values between -0.35 dex and 0.26 dex, with [α/Fe] = 0 and [α/Fe] = 0.4, respectively. For the optical part (above 3500Å) we used the α-enhanced E-MILES models from Vazdekis et al. (2015). For ages below 4 Gyr and metallicity below -0.35 dex we consider the differential offset obtained at 4 Gyr and at -0.35 dex, as no α-enhanced models have been computed in the UV spectral range.

Figure A.1 shows the difference between the estimated metallicity and the true ones, as a function of the true values of r-band light-weighted age, at $z = 0.30$, considering α-enhanced simulations. There is a systematic underestimation up to -0.3 dex at $S/N_{I,\mathrm{obs}} = 10$, while the errors decrease as the $S/N_{I,\mathrm{obs}}$ increases. The underestimation is large because our metallicity indices mostly consist of Fe indicators, which decrease as α/Fe increases. While Figure A.1 shows the importance of taking the effect of abundance ratios into account, in practice, the effect of chemical abundances might be not so severe, as the overabundance of different elements (e.g. [C/Fe]) tend to cancel out the effect of [α/Fe] (see La Barbera et al. 2017).

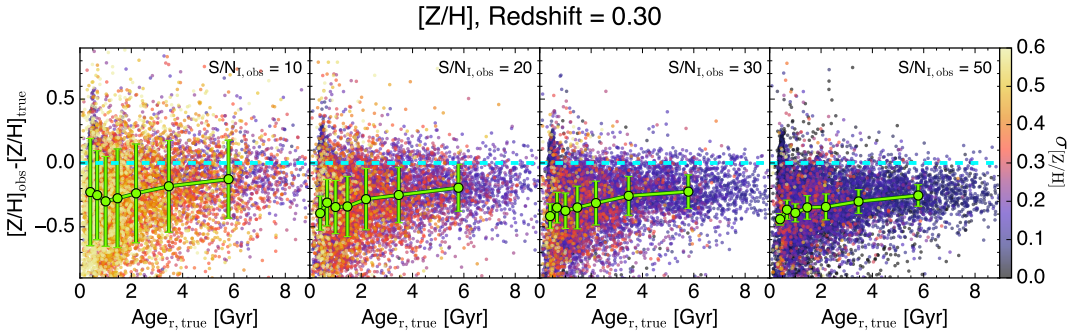

Figure A.1: Difference between the observed and true metallicity, as a function of true r-band light-weighted age values at $z = 0.30$, considering α-enhanced simulations. Each dot is colour-coded according to $\sigma_{[\mathrm{Z/H}]}$ obtained from the posterior. The green error bars are the median and the 68% confidence interval of [Z/H] differences in bins of $\mathrm{Age}_{r,\mathrm{true}}$, with each bin having the same number of data points. The cyan dashed line represents the 0 value of the y-axis.

Chapter B

Appendix to Chapter 5

B.1 Consistency between BOSS and DESI

We selected LRGs observed in both the BOSS and DESI survey within the redshift range $0.35 < z < 0.6$, in order to test the consistency between DESI and BOSS spectra. We stacked the individual spectra in groups of 30 galaxies, using those matched between the BOSS and DESI datasets and we performed the same analysis described in Chap. 5.2. Figure B.1 shows the results obtained in the measure of light-weighted age, [Z/H], and [Mg/Fe] for stacks of the matched galaxies in DESI and BOSS. The results for age and [Mg/Fe] are within 1σ across the redshift range where BOSS and DESI overlap. However, there is a systematic offset between the [Z/H] measured from the DESI and BOSS spectra of about 0.05 dex. The systematic offset in stellar metallicity that we found can be explained by the different fibre apertures used by the two instruments. BOSS fibres have a diameter of 2 arcsec, while DESI fibres are 1.5 arcsec, implying that BOSS spectra sample a larger fraction of each galaxy. Because massive passive galaxies are known to exhibit negative metallicity gradients, typically with $\Delta[Z/H]/\Delta \log R \sim -0.2$ to -0.4 (e.g. Santucci et al. 2020; Zibetti et al. 2020; Parikh et al. 2021), a larger aperture effectively includes a greater contribution from the outer, more metal-poor regions of the galaxies. Assuming a representative gradient of -0.3 dex/dex and the relative aperture sizes of DESI and BOSS (1.5 arcsec and 2 arcsec, corresponding to a difference of $\Delta \log\left(\frac{R_{BOSS}}{R_{DESI}}\right) \sim 0.12$), the expected metallicity difference is $\Delta[Z/H] \sim -0.04$ dex. This value is fully consistent with the observed offset (~ 0.05 dex) between the two datasets. This support the interpretation that aperture effects, coupled with intrinsic metallicity gradients, are responsible for the discrepancy.

B.2 TNG300-TNG100 comparison

We investigated potential differences of the stellar population parameters of massive quiescent galaxies ($\log(M_*/\mathrm{M}_\odot) > 11.5$ and $\log(\mathrm{sSFR}) < -11$) within TNG300 and TNG100 in the 5 snapshots described in Chap. 5.3.3. Figure B.2 shows the light-weighted age, stellar metallicity and [Mg/Fe] in the redshift bins $z = [0.2, 0.3, 0.4, 0.5, 0.7]$ for TNG300 and TNG100. We found that galaxies in TNG300 have slightly older ages compared to the ones in TNG100, with offset of around 0.5 Gyr, and well within the dispersion at each

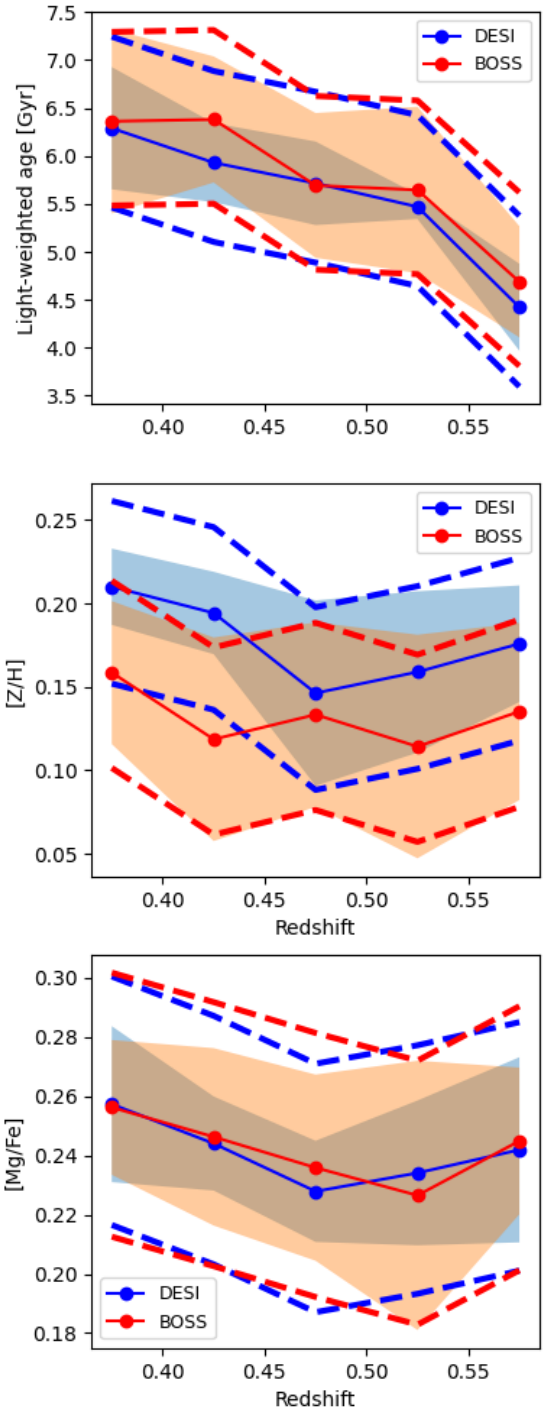

Figure B.1: Light-weighted age, [Z/H] and [Mg/Fe] in the redshift range $0.35 < z < 0.6$ for the matched DESI and BOSS stacked spectra. The data points represent the median value in each redshift bin, the dashed lines cover the typical uncertainties of the stacked spectra, and the shaded regions correspond to the intrinsic scatter within each bin.

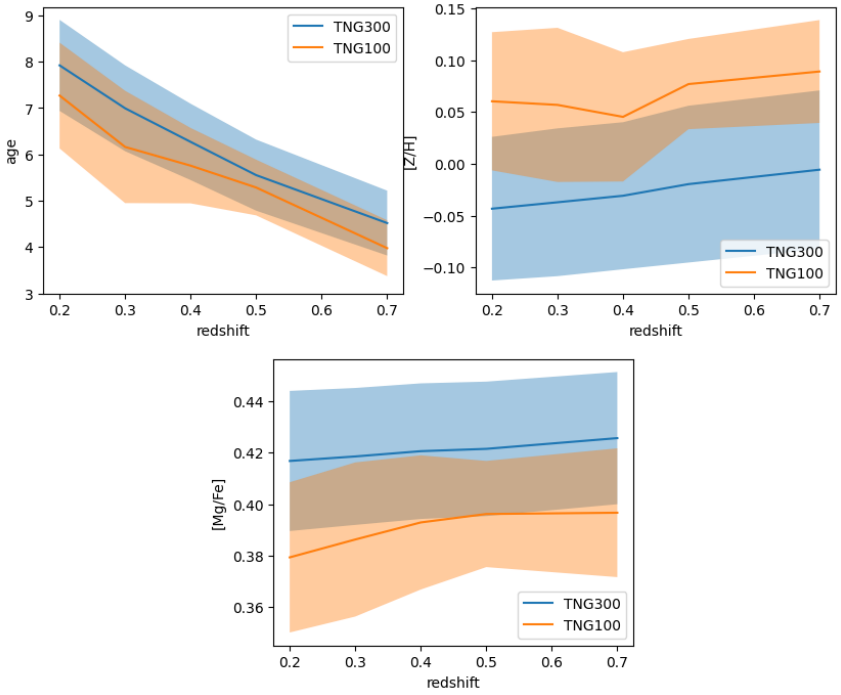

Figure B.2: Evolution of the light-weighted age, [Z/H] and [Mg/Fe] across the five redshift bins for galaxies in TNG300 (blue) and TNG100 (orange). The shaded regions represent the dispersion of each parameter within each redshift bin.

redshift. This is consistent with the reported effects of resolution on quenching timescales. Indeed, galaxies in TNG300 quench slightly earlier than the ones in TNG100, and can explain the slightly older ages (e.g. Donnari et al. 2019; Nelson et al. 2019; Donnari et al. 2021). For the stellar metallicity, we estimated slightly lower values ($\approx 0.05 - 0.1$ dex) in galaxies from TNG300 in respect to the ones from TNG100.

Finally, we found that [Mg/Fe] are marginally higher ($\approx 0.02 - 0.04$ dex) in galaxies from TNG300 than the ones from TNG100.

Despite these small differences, the trends and scatter of the stellar population parameters are consistent between the two simulation.